Cavity-Enhanced Raman Gas Spectrometry of Biogenic Gases

Kumulative Dissertation

zur Erlangung des akademischen Grades doctor rerum naturalium

(Dr. rer. nat.)

seit 1558

vorgelegt dem Rat der Chemisch-Geowissenschaftlichen Fakultät

der Friedrich-Schiller-Universität Jena

von Dipl.-Chem. Robert Keiner

geboren am 28.05.1986 in Suhl

Gutachter:

1. Prof. Dr. Jürgen Popp

2. Prof. Dr. Kirsten Küsel

Tag der öffentlichen Verteidigung: 6. Mai 2015

Table of Contents

1 Summary

1.1 Motivation

There is a variety of biological processes with gas involvement, such as photosynthesis and respiration (O_2/CO_2), denitrification (N_2), and methanogenesis (CH_4). Dedicated gas sensors for every single gas do exist. However, there is no sensor which is equally applicable for all gases, although it is sometimes necessary to quantify a blend of gases in order to solve a certain scientific problem. A gas sensor based on Raman spectroscopy should be able to measure all molecular gases simultaneously, because it is based on the characteristic inherent molecular vibrations of a gas. A major drawback of Raman spectroscopy is the low efficiency of the Raman process. This could be compensated with the high exciting laser power of an optical cavity arrangement. A Raman gas device which is based on cavity-enhanced Raman gas spectrometry should have many advantages over common gas sensors and should be applicable for a variety of scientific questions.

The present work describes the modification of such a device in hard- and software to fit the demands like versatility and sensitivity of various biogeochemical gas measurements. Three selected applications with increasing degree of complexity are presented. The objective is to show that Raman gas spectrometry can be a superior novel tool in biophotonics with its advantages arising mostly from the new sensing mechanism compared to the present solutions.

1.2 Current State of Research

Mobile, on-site and cost-efficient multi-gas sensors with low power consumption are important for life sciences and environmental research. Applications include e.g. isotope quantification[1,2], biogas analysis[3,4], breath gas analysis[5] and environmental monitoring[6-9]. Relevant gases include N_2, O_2, CO_2, CH_4 and N_2O[10]. Generally, the simultaneous quantitative detection of multiple gases is desired.

In the context of environmental gas sensing gaseous nitrogen compounds such as N_2 and N_2O play an essential role in the intensive agriculture as the end product of denitrification[11-14]. Especially dinitrogen gas is not easily sensed by optical means except by Raman spectroscopy[15], however it can be sensed by exploiting its ionization potential[16]. Raman gas spectrometry is one of the rare methods that are able to detect and quantify all diatomic gases, especially homoatomics like nitrogen and oxygen. Oxygen plays an important role in aerobic bioprocesses and photosynthesis. Common oxygen sensors include paramagnetic sensors, electrochemical sensors like the Nernst-cell, semi-conductive oxygen sensors, and photoluminescence sensors[17]. Carbon dioxide is the main product of combusting processes like respiration. For carbon dioxide detection galvanic as well as optical near infrared (NIR) absorption sensors are commonly used. Stable isotopes like $^{13}CO_2$ are often used for isotope labeling, because of their availability, price and innocuousness. Isotopes like $^{12/13}CO_2$ and $^{14/15}N_2$ are hard to distinguish, due to their very similar chemical properties. They are conventionally quantified by means of complex laboratory-based isotope ratio mass spectrometry (IRMS)[18]. A laser spectroscopic technique for CO_2 quantification with remarkable development throughout the past years is cavity ring-down spectroscopy (CRDS)[19]. This technique enables the portable highly sensitive quantification of many single gases like CH_4, N_2O, CO_2 and H_2O. New broadband methods promise the simultaneous measurement more than one gas in a single cavity[20]. However, one major drawback of these broadband methods is the limited availability of NIR-broadband sources and the lower reflectivity of broadband mirrors.

Solutions for single gas analysis are available, but most applications require the simultaneous analysis of several gases at once. The small number of detectable environmental gases, which is often criticized in reviews[5,21], is due to the lack of capable devices, available for that

purpose. To increase this number, several electrochemical sensors are combined in a portable multi-gas measurement device. The device gets more complex by this combination of multiple sensors, because the requirements and characteristics of every single sensor have to be taken into account. The parallel use of several unspecific sensors mimes the human or animal nose and is therefore called electronic nose[22,23] or optical nose respectively[24,25]. These approaches achieve higher specificity but also combine disadvantages like aging, drift and saturation[23].

Multi-gas sensors are able to detect a whole range of gases with a single method. Examples are mass spectrometry (MS), ion-mobility spectrometry (IMS) and mid- (MIR) or near-infrared (NIR) absorption spectrometry. The gases are spectrally separated, which allows distinct identification and quantification. However, all common methods show essential disadvantages. Mass spectrometry is limited in portability, because of the necessary turbo pumps for high vacuum. This is circumvented in ion mobility spectrometry where ambient air serves as a drift gas. These devices are especially suited for simultaneous detection of small ionizable industrial gases or chemical warfare agents[26]. Another method for multi-gas detection is infrared spectroscopy. The mid-infrared spectral range offers sensitive detection, because it exploits vibration transitions of molecules with high absorption cross-sections. However the optics needed for these wavelengths are expensive and often sensitive to water. Common SiO_2-based optics are sufficient for the near-infrared range, where overtones of the fundamental vibrational modes are located.

Raman gas analysis is a spectroscopic method which enables detection and quantification of all gases mentioned above including nitrogen. Also unknown gases can be detected and hints about their structure are obtained. However, the effect of inelastic light scattering is inherently very weak[27] and the molecule density of gases is low. This makes the detection of low gas concentrations via Raman spectroscopy very challenging. Possibilities to improve the detection limits include enhanced excitation and collection efficiency of the scattered light. The excitation efficiency is increased approx. 50 times with the help of multi reflection cells and spherical mirrors[28,29]. Detection limits in the hundred ppm range were obtained with these methods[30]. High-finesse power build-up cavities can increase the field of a laser diode

up to three orders of magnitude[31,32]. This could improve the detection limit by one more order of magnitude leading to detection limits in the ten ppm range.

With only few exceptions such as monoatomic gases like the noble gases, all gases can be measured simultaneously with Raman gas spectrometry. The inelastic scattering process is inherently fast compared to other methods and linear in the complete dynamic range. The whole system as well as the costs should be miniaturizable since the substantial progress in semiconductor optoelectronics, namely charge coupled devices (CCD) and laser diodes (LD). This makes the method universally applicable for a variety of applications like investigation of respirational processes (O_2/CO_2), photosynthesis (CO_2/O_2), methanogenesis (CH_4) and denitrification (N_2O, N_2). Therefore the method is superior to a complex and cost-intensive combination of most diverse techniques which would be necessary to cover the quantitative detection of all relevant biogenic gases.

1.3 Theory and Setup

The ability to detect all gases is fundamental for Raman gas spectrometry. This chapter briefly describes the necessary theory as well as the setup for Raman gas spectroscopy.

1.3.1 Quantitative Raman Gas Spectroscopy

Raman scattering is utilized for molecular spectroscopy and to some extent complementary to infrared absorption spectroscopy. Raman scattering reveals information about the structure and properties of molecules via vibrational transitions. The majority of the Raman scattered light is shifted to longer wavelengths (Stokes scattering)[33]. Raman scattering leads to a very weak signal and to an insufficient signal-to-noise ratio for certain applications aiming for high sensitivity compared to other spectroscopic techniques like absorption spectroscopy. Several parameters can improve the sensitivity and therefore the limit of detection. These are expressed by the simplified equation[34,35]:

$$I_R(\tilde{\nu}_R, \tilde{\nu}_0) = \eta \, I_0 \, N \, \left(\frac{d\sigma(\tilde{\nu}_R, \tilde{\nu}_0)}{d\Omega}\right) \Omega \, L. \tag{1}$$

In this equation, I_0 represents the intensity of exciting field, I_R the intensity of the Raman scattered light, N is the molecule density of the measured gas (parts per cm^{-3}). The factor η represents the detection efficiency of the experimental setup and takes intensity losses related to signal collection geometry, the optical components (mirrors, grating efficiencies), and quantum efficiency of the detector into account. Ω contributes to the solid angle of the signal collection optics and the effective scattering length is the probe volume length L. $(d\sigma)/(d\Omega)$, the absolute differential Raman scattering cross-section (in cm^2 sr^{-1}) is herein given by following equation,

$$\left(\frac{d\sigma}{d\Omega}\right) = \frac{(2\pi)^4}{45} \frac{(\tilde{\nu}_0 - \tilde{\nu}_R)^4}{1 - \exp(-\frac{hc\tilde{\nu}_R}{kT})} \frac{h}{8\pi^2 c\tilde{\nu}_R} \frac{1}{(4\pi\varepsilon_0)^2} g(45a^2 + 7\gamma^2), \tag{2}$$

where $\tilde{\nu}_0$ is the excitation wavenumber, $\tilde{\nu}_R$ the wavenumber of the Raman signal, g is the degeneracy of the Raman mode, a^2 and γ^2 are the isotropic and anisotropic part of the polarizability tensor (C^2 V^{-2} m^4)[36]. From the above equation (1), we can observe a linear relationship between the intensity of the Raman scattered light and the laser intensity, as well as the particle density of the gas. The particle density is related to the pressure by the ideal gas law and is thus linear with pressure. According to equation (1), there are multiple

options to improve the performance of a Raman gas sensor, as for instance: increased gas pressure, collection angle, reduced exciting wavelength, reduced gas temperature and increased exciting laser power I_0.

1.3.2 Cavity-enhanced Raman Spectroscopy

The setup that was used for the measurements was a Raman gas monitor prototype built within a cooperation of Philips Medizin Systeme Boeblingen GmbH and Carl Zeiss Jena GmbH. It is based on a power build-up cavity that increases the exciting laser power by several orders of magnitude. The optical cavity as well as further setup constituents for biogenic gas analysis are discussed in this chapter.

Miniaturization plays a major role in mobile and portable gas analysis based on Raman spectroscopy. This has been considered using miniaturized parts, for example light source and detector. Figure 1 shows the principle setup and Figure 2 some example Raman spectra.

The laser cavity consists of an external 650 nm laser diode with anti-reflection coating at the front facet. The emitted light of the laser diode is focused into the center of the cavity. The cavity is pumped through the input coupler mirror and the beam is reflected back from the high reflective end mirror. Both of these mirrors have extremely low scattering losses and form a stable confocal resonator. A cavity of this geometry and with these reflectivity values acts as a power build-up cavity (PBC) supporting a Gaussian beam inside the cavity. The laser diode feeds about 50 mW of power into the cavity and acts as the gain medium. Due to the very low losses inside the cavity the power there builds up by a factor of several thousand to more than 100 W. Figure 1 illustrates the optical pathway.
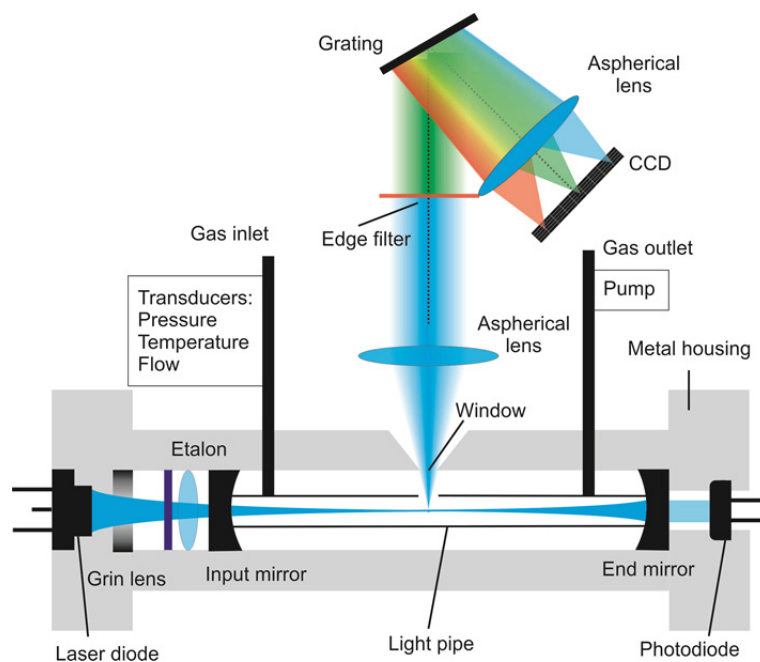
Figure 1: Schematic diagram of the optical pathway. Blue: resonator mode in the power build-up cavity. Green lines indicate inelastically scattered light.

The spectrograph in the system has a very compact design. The radiation scattered from the laser beam is collimated by an aspherical lens and falls onto a planar diffraction grating. The diffracted spectrally separated radiation is imaged by an aspherical camera lens onto a linear CCD array of 512 elements. The wavelength range covered by this spectrograph allows to record the Stokes-shifted Raman scattered light of the gas molecules interacting with the laser beam. Behind the collimator lens a long-pass Rayleigh filter is mounted in the parallel beam in order to filter Rayleigh-scattered light from the signal impinging onto the CCD array. With this device it is possible to acquire spectra within a measurement time of 33 ms. The gas sample is pumped through the cavity. Changes of gas composition over time can be monitored with high temporal precision. The thermal measurement of the gas flow is facilitated and this is used to ensure and adjust a continuous gas flow. Dust particles are filtered out before entering the laser cavity by sterile filters. The gas sample is continuously monitored for temperature, pressure and flow. The number density of each gas component in the volume interacting with the laser beam is a measure of its relative abundance in the sample. Quantification of the partial pressures of the gas species in the sample is accomplished via calibration of the system with pure samples of each gas of interest. Some prominent gas spectra are plotted in Figure 2.
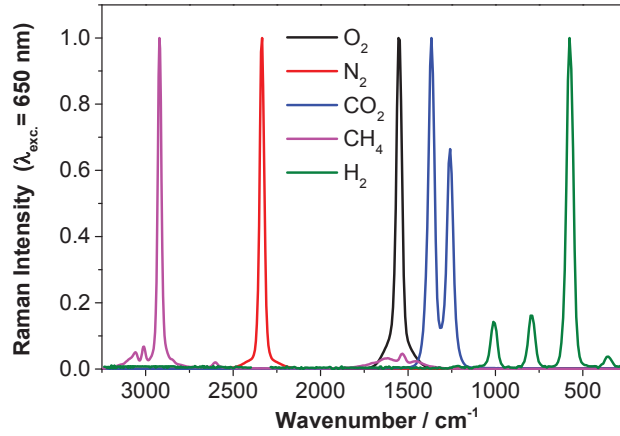
Figure 2: Raman spectra of some prominent gases. The spectral intensity is normalized to one for better visibility.

Linearity and Scaling

All signal influences that are not related to the gas concentration have to be compensated to establish Raman gas spectrometry as method for quantitative analysis. First of all, the Raman spectrum is intra-cavity power dependent. This was investigated in a diode current tuning while acquiring Raman spectra in Figure 3a. It was found that the Raman intensity scales linear with the laser diode current (Figure 3b).

a

b
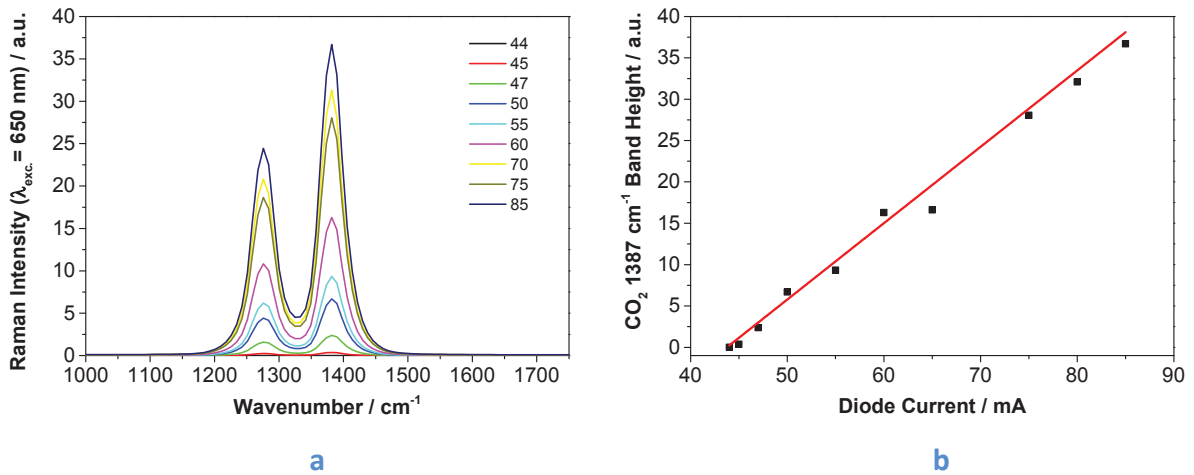
Figure 3: Spectra of 23% vol. CO_2 in Argon versus the gain medium current (unit: mA). The spectral intensity scales with the current. Band height analysis of the spectra of the 1387 cm^{-1} band. No deviations other than statistical uncertainty from linearity are visible.

High light intensities could lead to nonlinear effects. However, no deviations from intensity were observed. Reasons are the low matter density of gases and, with respect to nonlinear effects, the low intra-cavity power.

Dynamic Range and Limit of Detection

Stability and reproducibility of the spectral intensity was the first requirement for quantitative measurements. The second is the linearity of the Raman signal with the analyte concentration. It is crucial if a simple and fast calibration is desired A linear fit through the origin and one point proved to be sufficient, because of the excellent linearity over the whole dynamic range (Figure 4a) on the one hand and stable spectral background leading to an unbiased signal after background correction on the other hand.
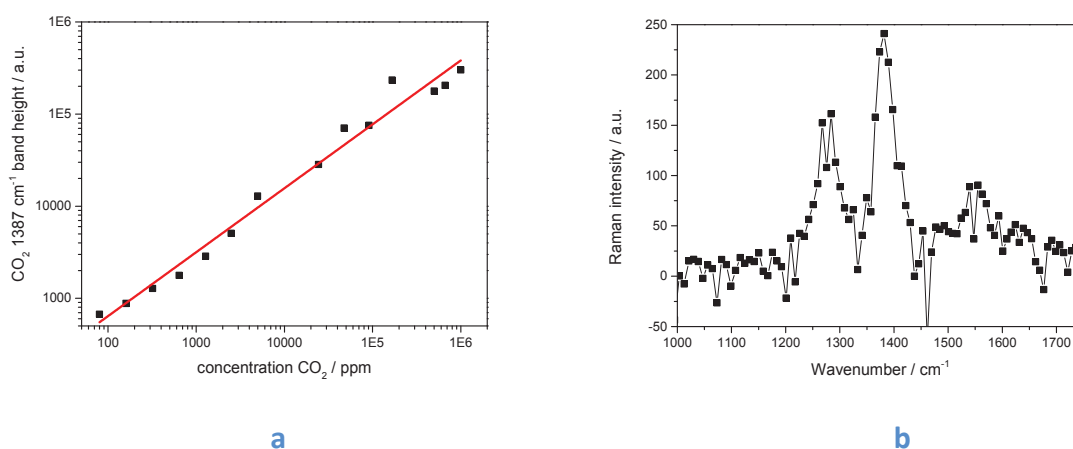

| a | b |

Figure 4: a) Analysis of the dynamic range. The band height increases linearly with the concentration in a range of four orders of magnitude.
b) Spectrum of 80 ppm CO_2 in Ar. The peak height at 1387 cm^{-1} is 241, the standard deviation of the noise in the range of 1000…1200 cm^{-1} was determined to be 16. The LOD is supposed to be three times the standard deviation of the baseline noise, equaling 48 ppm if only the peak height of the highest peak is evaluated. The LOD reduces/improves further, if more CCD pixels are taken into account.

The measurable concentration range spans over almost six orders of magnitude, ranging from 100 % vol. down to ca. 50 ppm. No saturation occurs within this very large range compared to other gas sensors. Linearity governs the whole range which is a very strong and rare advantage of this method.

The limit of detection (LOD) for CO_2 can be estimated by analyzing the low concentration spectrum in Figure 3b. Generally, LOD is considered as a peak height equaling three times the baseline noise ($\sigma = 3$). This yields an LOD of 48 ppm for CO_2. The exact LOD depends on the actual differential Raman cross-section of each gas species. A brief overview of Raman cross-sections of prominent gases normalized to the one of N_2 is found in Table 1. Reported ratios[27] were adjusted to 650 nm using an assumed frequency dependence of v_R^4. The

absolute differential Raman cross section for the vibrational line (Q-branch) in nitrogen was adjusted from the same reference and resulted in $8.81*10^{-32}$ cm²sr^{-1}mol^{-1}.

Table 1: Important biogenic gases, their transition wavenumbers and the differential cross sections with respect to the one of N$_2$ for an excitation wavelength of 650 nm.

Gas	frequency / cm^{-1}	ratio
N_2	2331	1.0
O_2	1556	1.4
$CO_2\ (v_1)$	1388	1.5
$CO_2\ (2v_2)$	1286	1.0
$N_2O\ (v_1)$	1285	2.4
$N_2O\ (v_3)$	2224	0.5
$CH_4\ (v_1)$	2914	5.7
$C_6H_6\ (v_1)$	3062	6.6
$C_6H_6\ (v_2)$	992	10.1

Data processing and result validation was done with a software which also allows working with different setups for parallel monitoring of two or more samples. One concentration has to be measured for calibration. Gases are therefore measured either as pure gases or as known mixtures with an inert gas. The reproducibility of the calibration process was determined by measuring the calibrated gas again. The relative standard deviation of this procedure was below 0.3 %. The concentrations were obtained using a classical least-square fit of the calibrated pure gas spectra and the measured spectrum, this is called soft modeling[37]. Therefore an over determined linear equation system is solved:

$$\begin{bmatrix} I_{g_11} & \cdots & I_{g_m1} \\ \vdots & \ddots & \vdots \\ I_{g_1n} & \cdots & I_{g_mn} \end{bmatrix} * \begin{bmatrix} c_1 \\ \vdots \\ c_m \end{bmatrix} = \begin{bmatrix} I_{a1} \\ \vdots \\ I_{an} \end{bmatrix}$$

Equation 1: Least-square fit of pure gas spectra and unknown spectrum.

with calibration gas g, analysis gas a, Intensity I, CCD pixel n, and number of gases m. The validation of the calibration procedure in this thesis is carried out with a total of three points: the pure gas, a zero measurement and a certified test gas mixture. The standard

deviation of successive measurements of pure nitrogen was 0.2 %. The zero measurement depends strongly on the baseline stability, which deviated by 50 ppm for nitrogen gas. The results of the test gas analysis are shown in Table 2.

Table 2: Comparison and deviation from certified test gas (Linde AG, D-06237 Leuna) prepared in compliance with DIN EN ISO 6141. The absolute deviations were below 0.16%.

gas	test gas %	Raman %	deviation %
N_2	1.12	0.96	0.16
O_2	0.92	1.05	0.13
CO_2	1.02	1.05	0.03
N_2O	0.99	1.09	0.10
CH_4	1.08	1.08	0.00

There were only small absolute deviations below 0.16 % from of the concentrations obtained by Raman gas spectrometry and these obtained with several certified gas chromatographic measurements. This quantifies the absolute accuracy of the cavity-enhanced Raman gas spectrometry setup.

1.4 Closed-Chamber Experiments

The evolution of gas atmospheres and fluxes are often more relevant than just concentrations. One option to measure fluxes is to establish a closed system and to record gas concentrations over time. The fluxes are obtainable even for very low gas concentrations below the detection limit because of this enrichment process.
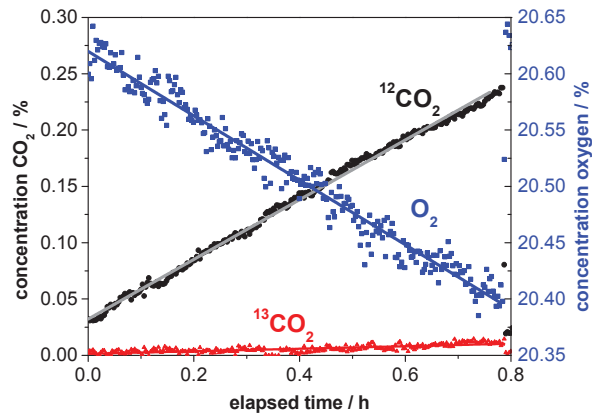

Figure 5: Example closed chamber measurement taken from a leaf dark respiration measurement of ^{13}C-labeled beech mesocosms. Linear concentration courses of O_2, $^{12}CO_2$, and $^{13}CO_2$ are shown. The flux is determined via linear fitting.

Enriching can be a very powerful tool to determine small changes, but it is limited to the sample-dependent range of linearity. This range turned out to be very big for the dark respiration of leaves (Figure 5). The slopes of the linear fits with the respective errors are O_2: -2860±31 ppm/h, $^{12}CO_2$: 2650±10 ppm/h, $^{13}CO_2$: 112±7 ppm/h. Even the $^{13}CO_2$ flux rate can be obtained via long closed chamber enrichment, although its concentration is 20 times lower in comparison to $^{12}CO_2$. The uncertainty for oxygen is three times higher than that for CO_2, because uncertainty scales with the peak height and small oxygen changes in the range of 30 ppm are detected on an underground signal of 205000 ppm (blue curve in Figure 5). The underground signal for carbon dioxide is considerably smaller in comparison.

Closed chamber experiments are often performed to obtain soil gas exchange rates. However, they suffer from an underestimation of the soil gas rates[38,39], because of diffusion limits of the gases into the porous soil. This was investigated by other researchers and a non-steady state diffusion model was established[38]. In the present work, an exponential fit of the type $f(t) = a * e^{bt} + c$ is used to determine the slope at time t = 0, which was assumed to be the best representative of the actual soil gas flux.
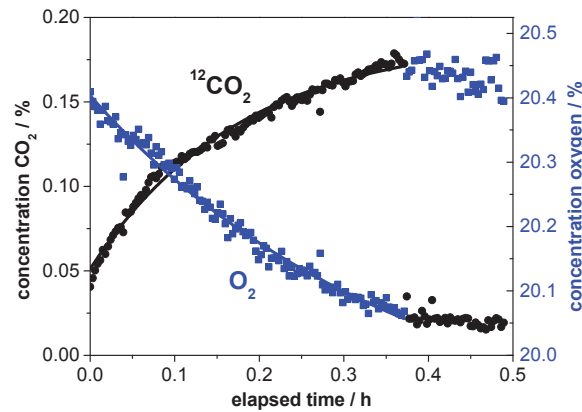

Figure 6: Example soil respiration graph of a sandy-loamy soil. The observed experimental oxygen and carbon dioxide courses (squares and spheres) and their exponential fits (solid lines) are shown. Ambient air is the starting atmosphere and is again measured as reference in the end.

The first derivative of this function is $f'(xt) = a * b * e^{bt}$, the slope at t = 0 represents the gas rate and is equal to $f'(0) = a * b$. This data processing was automated in a LabVIEW program to enable fast and reproducible processing of many datasets. The rates for oxygen and carbon dioxide in Figure 6 are: O_2: -1.48 %/h and CO_2: 0.77 %/h.

Volume and leak test

The gas rates are obtained in volumetric units and need to be related to the sample and have to be corrected by the total experimental gas volume. This volume is determined by an overpressure test, which serves simultaneously as a leak test. A defined amount of gas volume is injected into the closed system for this purpose and the pressure leap is determined via the built-in pressure sensor.
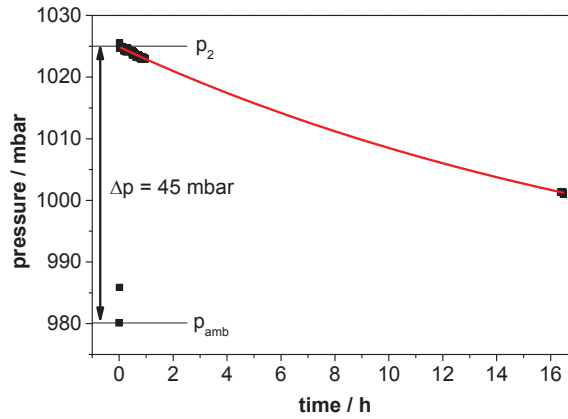
Figure 7: Example graph for the pressure test (black dots) with pressure leap and decay for the determination of the total volume and leak testing including an exponential decay fit (red curve)

In Figure 7, a glass syringe was used to inject a defined volume of 50 mL gas into the experimental setup. This led to an end pressure of 1015 mbar and to an overpressure of 45 mbar, respectively. The total gas volume V_{tot} of the setup is derived from the isothermal ideal gas equation:

$$p * V = \text{const}$$
$$p_1 * V_1 = p_2 * V_2$$

with the ambient state (ambient pressure p_{amb} and volume of the syringe V_{Sy}) at the left side:

$$p_{amb}(V_{Sy} + V_{tot}) = p_2 V_{tot}$$

$$V_{tot} = \frac{p_{amb} V_{Sy}}{p_2 - p_{amb}}$$

A total volume of 1097±61 mL is obtained for three measurements for the example in Figure 7, which is consistent for a setup that consisted of an 1 L glass serum bottle, spectrometer and tubing.

Leakproofness can be assured with the same test. An exponential decay function

$$f(t) = ae^{bt} + c$$

is fitted to analyze the decay rate of the overpressure which serves as a measure for the leakproofness. The parameter c, the asymptote for the decay function, equals the ambient

14

pressure; the parameter a is the overpressure at t = 0. The resulting decay rate b is conveniently converted into the half-life time of overpressure:

$$t_{1/2} = -\frac{ln2}{b}$$

The resulting half-life time for the above example in Figure 7 is 15.3 h. This test can be considered a worst-case scenario for a pressure gradient between the system and the atmosphere. This gradient is in common experiments not larger than the weather-dependent atmospheric pressure variations which are in the range of 980…1000 mbar at the local altitude[40]. This test was automated and delivers the total volume and the half-life time within some minutes depending on the desired tightness and the accuracy of the pressure sensor, which is currently limited by its resolution of 0.3 mbar. These values are crucial for closed chamber experiments.

1.5 Selected Applications

1.5.1 Bacterial Respiration

The brief opening of the Herrenberg cave provided a unique opportunity to investigate bacteria that lived in the absence of light for thousands of years [RK1, RK5]. A bilateral collaboration combined the expertise of Raman spectroscopy and microbiology, such that the biogenic mineral samples of different sites in the Herrenberg cave were supportively investigated by near-infrared Raman macrospectroscopy and confocal Raman microspectroscopy [RK5] on the one hand and extracted cave bacteria were cultivated and investigated in terms of respiration and mineral formation [RK1] on the other hand.

The extracted cave bacteria (*Arthrobacter sulfonivorans)* were cultivated in a liquid growth medium which was optimized to best represent the cave environment. The respiration in the headspace above this medium was monitored with cavity-enhanced Raman gas analysis. Oxygen and carbon dioxide concentrations over time were obtained. The concentrations were differentiated with respect to time yielding the according respiration velocities. Two maxima were detected for the pleomorphic (two-stage) lifecycle of A. *sulfonivorans*, whereas a single-stage lifecycle bacterium (*Pseudomonas fluorescens*) yielded only one maximum (see Fig. 2 in [RK1]).

The bacteria precipitated calcium carbonate which was investigated with Raman macro and microspectroscopy. Near-infrared (1064 nm) Raman macrospectroscopy was applied for fluorescence-free spectra acquisition of the averaged sample composition. The carbonate valence vibration in the Raman spectra around 1086 cm^{-1} indicated that a high amount of calcium carbonate precipitates as the thermodynamically instable mineral vaterite first. The stable form calcite was exclusively detected in later samples in contrast. This shows that calcium carbonate crystallizes first as vaterite which transforms to the stable calcite later.

Single carbonate crystals could be targeted with 532 nm Raman microspectroscopy. The microscopic results indicated that the bacteria serve as nuclei for the crystallization of biogenic vaterite. Epitaxial growth of further calcium carbonate happens preferably in form of calcite. This was exemplarily shown with a chemical Raman image showing a vaterite crystal which is surrounded by epitaxial calcite.

In summary, Raman spectrometry sterile monitored the gaseous headspace for oxygen and carbon dioxide changes on the one hand and determined the solid microcrystal composition on the other hand. The Raman gas spectrometry revealed differences in the life cycle of the pleomorphic bacteria versus one-stage lifecycle bacteria. Raman macro and micro-spectroscopy discovered the mechanism of vaterite and calcite precipitation. This gave valuable hints on the functioning of biomineralization inside cave wall biofilms and may explain the crystal size in the micrometer range and the macroscopic shape of karstic cave walls. No other technique owns this analyte versatility.

1.5.2 $^{13}CO_2$ Labeling of Plants

The counter-ecosystem function to bacterial and plant respiration is the photosynthesis of green plants. This is exploited in ecophysiological studies as introduction pathway for the labeling with stable mass isotope ^{13}C [RK2] by photosynthetic assimilation of $^{13}CO_2$. This procedure has many advantages for the investigation of the flow of resources: The stable mass isotope is the perfect inert label, because it is not radioactive, not decomposable and has no significant influence on the subject's metabolism.

Unfortunately, stable mass isotopes are hard to distinguish from their abundant isotope, which makes it difficult to sense them in any other way than mass-resolved. The common analytic method is mass spectrometry, mostly coupled to gas chromatographic separation (GC-MS). With some modifications, it is also possible to sense the O_2/N_2 ratio as the other important gas related to photosynthesis. However, this coupled technique is bulky, slow, consumptive, expensive, and a complex calibration of the non-linear mass spectrometer response with special test gases is necessary. These disadvantages may be overcome by Raman gas spectrometry with fast spectral separation of all gases. The mass isotopes in particular are spectrally shifted, because the molecular vibration frequency is altered by altered reduced mass of the molecule. The Raman spectrum of CO_2 is marked by a Fermi diad, due to the coupling of deformation overtone and valence vibration (see Fig. 1B in [RK2]). The mass change of carbon induces a change in the intensity distribution of the diad as well as an altered spectral position. This allows the quantitative spectral separation in the Raman spectrum of the chemically almost identical isotopes within labeling experiments.

The $^{13}CO_2$ labeling was performed in a sealed chamber which was integrated into a gas cycle with the Raman gas cavity. Saplings of *Populus trichocarpa* were placed inside the chamber and $^{13}CO_2$ was released. The concentrations of nitrogen, oxygen, $^{12}CO_2$ and $^{13}CO_2$ were recorded via Raman gas monitoring (see Fig. 1 in [RK2]). The important peak values of $^{13}CO_2$ around 380 ppm were resolved and it could be assured that they do not exceed a CO_2 concentration limit of 400 ppm. The second dose was administered as the Raman-$^{13}CO_2$-concentration fell below 100 ppm.

Two separate labeling runs were performed in total (see Fig. 3 in RK[2]). The second run yielded an overall oxygen production of 0.38 mol/d, and 63 % of the $^{13}CO_2$ were consumed in

t_e = 17.2 min. A lower overall oxygen production of 0.35 mol/d and a slower $^{13}CO_2$ uptake of t_e = 23.5 min were measured for the first run in comparison. This is explained by the lower mean light intensity (photosynthetic active radiation, PAR) and the lower total leaf area inside the chamber for the first run. The $^{13}CO_2$ uptake was stated based on the exponential decay time. This time was obtained by exponential fitting of the decay curves. That worked exceptionally well, because of the high time resolution of the optical measurement leading to highly resolved decays and good quality fits.

The labeled plants were further investigated by leaf dark respiration measurements with only little changes to the setup. A dark container of one liter size was used to enclose a defined leaf area. The oxygen and carbon dioxide concentration courses were measured and respiration rates were calculated based on the leaf area that is covered by gas-exchanging stomata. The mean CO_2 and O_2 rates were $1.8 \, \mu mol \, m^{-2} \, h^{-1}$ for immature leaves and $0.7 \, \mu mol \, m^{-2} \, h^{-1}$ for mature leaves, what is in good agreement with values reported in literature. Furthermore, Raman gas spectrometry provides an opportunity to calculate the respiratory quotient (RQ) due to the additional quantification of oxygen fluxes. The respiratory quotient is defined as the amount of released carbon dioxide divided by the amount of consumed oxygen. It can characterize the type of combusted substrate. In the dark, leaves combust starch and other carbohydrates that they generated by photosynthesis during daylight. Carbohydrates produce an RQ of one, what was approved by in-situ Raman gas measurements. Determinations of RQ own a huge potential for further ecophysiological studies that are running to date.

In summary the short communication [RK2] briefly proves, that Raman gas spectrometry is a valuable tool for ecophsiological studies including the comprehensive monitoring of labeling experiments, dual respiration rate determination, and RQ determination.

1.5.3 Monitoring of a Complex Ecosystem

Photosynthesis and leaf dark respiration were separately investigated in this third chapter. In the third publication, [RK3], a complex ecosystem consisting of both peat soil and sphagnum moss as green plant, was monitored. It is demonstrated, that a proper multi-gas analysis can lead to valuable multivariate ecosystem data.

Monitoring of peatland areas is important, because they store in an area of only 3 % of the global land surface approximately one-third of the world's soil carbon. Peat bogs act as carbon sink, because they fix carbon dioxide in a growing organic peat layer. The peat has to be covered by water, since this carbon fixation is an anoxic process. The global warming and agricultural land-use lead to drained and desiccated peat layers, which then change their ecosystem function from carbon sink to strong CO_2 source due to the aeration and therewith oxidation of the organic matter. This CO_2 emission risk and the high methane production of peat bogs constitute how important the gas-related specification considering soil respiration, photosynthesis, and methanogenesis of peat areas is. The on-site characterization should be done via portable gas sensors, which are able to quantify the occurring biogenic gas mixtures (N_2, O_2, CO_2, CH_4). Raman gas analysis is supposed to be able to supplement the existing non-dispersive infrared techniques for CO_2 and CH_4.

To prove this hypothesis, a peat bog column experiment was performed. A sample of the peat bog including the sphagnum was carefully cored and transferred into a transparent acrylic cylinder. The column was incubated at room temperature under varying light conditions. A gas cycle between the Raman cavity and the headspace of the column was established. The gas phase monitoring lasted for four hours and N_2, O_2, CO_2 and CH_4 were monitored.

The interdependence of oxygen and carbon dioxide was of particular interest (Fig. 2 in [RK3]). The intense light at the beginning of the experiment promoted photosynthesis and decreased CO_2 concentration to the plant-specific CO_2 compensation point of 170 ppm. The maximum slopes around 3.3 $\mu mol\, m^{-2}\, h^{-1}$ represent the maximum photosynthesis rate of the sphagnum as a C3 shade pant. The amount of soil respiration (0.2 $\mu mol\, m^{-2}\, h^{-1}$) was indirectly quantifiable during the period of steady CO_2 concentration by the slope of the oxygen concentration, because soil-CO_2 is immediately transformed into O_2 by

photosynthesis. Leaf dark respiration was quantified in the last period during the total absence of light. The sum respiration (3.2 µmol m^{-2} h^{-1}) equals soil and leaf respiration and leaf respiration (3.0 µmol m^{-2} h^{-1}) by subtracting the already known soil respiration.

Besides the interesting results due to simultaneous oxygen and carbon dioxide quantification, diffusion-induced difficulties of standalone CO_2 quantifications were encountered (for details see [RK3]) and an enrichment of methane in the headspace was quantified and normalized to the emitting soil area (0.11 µmol m^{-2} h^{-1}) and could therefore serve as a parameter in climate models.

In summary, Raman gas spectrometry was proven to be a versatile and superior toolkit for the investigation of the dynamics of greenhouse gas fluxes and for the elucidation of complex biogeochemical processes.

1.5.4 Fiber-enhanced Raman multi-gas spectrometry

The amplification of the optical field has happened inside an optical cavity up to this point of the thesis. Now this method shall be compared with an alternative approach for sensitive Raman multi-gas spectrometry: the enhancement of the Raman signal inside a hollow core photonic bandgap fiber. The two methods are both based on Raman gas spectrometry, however signal amplification is accomplished in different ways.

Hollow optical fibers feature the following advantages for Raman gas sensing: guiding of the analyte, minimal sample volumes, guiding of exciting laser light, almost complete spatial overlap of light and analyte, and guiding of the inelastically scattered light in the framework of the numerical aperture. That suggests the "enrichment" of Raman light and therefore scaling sensitivity with increased fiber lengths.

A setup was built on an optical table to prove the applicability of Fiber enhanced Raman gas sensing to environmental gas analysis and breath-gas analysis. The optical part of this setup (see Figure 1 in [RK5]) consisted of a 2.8 W 532 nm Nd:YAG laser, telescope, dichroic beam splitter, microscope objective and a liquid nitrogen cooled spectrometer. This focused the laser light into the hollow core of a photonic bandgap fiber. The backscattered Raman light was collected via the same microscope objective, passed a pinhole and an edge-filter and was finally focused into a spectrometer. The gas part of the setup consisted of a sophisticated adapter (see Figure 2 in [RK5]) featuring four ports: two ports are connected to gas, what allows gas filling of the fiber and flushing of the system. One central port holds the fiber in place with outstanding spatial stability in the sub micrometer range. The fourth port has a sealed optical window and allows the exciting laser light to be focused into the fiber core and allows the Raman scattered light to be collected by the microscope objective. The gas was filled into the fiber core by a syringe pump supporting pressures up to ten bar.

The whole setup was intended to push todays detection limits of fiber enhanced Raman gas spectrometry and was not optimized for size. The whole setup is therefore much bulkier and immobile compared to the cavity-enhanced miniaturized mobile setup.

As a result, linear scaling of the Raman gas signal with laser power and partial pressure was observed (Figure 3 in [RK5]), equally to the cavity-based approach (see Figures 4 and 5 in this thesis). To prove the simultaneous multi-gas detection capabilities, a certified test gas

mixture consisting of five gases was measured. Each gas had a concentration of 1 %. The gases in the resulting spectrum in Figure 4 in [RK5] were spectrally well separated due to the higher spectral resolution. This doesn't theoretically improve the limit of detection, because the peak area is unaffected by its broadness. However, unideal influences like drifting baseline and not normally distributed baseline noise leads to higher signal-to-noise ratios for high-resolved systems. The sub inverse centimeter resolution of the FERS setup allowed the observation of the natural $^{14}N^{15}N$ and $^{13}CO_2$ isotopes in human breath. These are promising results, considering that especially the nitrogen isotope breath gas analysis is not extensively explored yet.

The "analytical power" of the two methods can be compared by normalizing the obtained LODs to laser power, pressure and measurement time.

Table 3: Comparison of CERS and FERS with respect to the obtainable LOD. The LOD was normalized to time, laser power and pressure to improve comparability.

	CERS	FERS	
laser power I	50	2000	mW
pressure p	1	20	bar
measurement time t	100	1000	ms
LOD	48	4	ppm
$LOD * I * p * \sqrt{t}$	1	160	ppm*W*bar*$\sqrt{s}$

The analytical efficiency of CERS is over one hundred times higher than that of FERS. It achieves lower LODs, which is mainly due to the low exciting laser power and the massive optical field enhancement in the cavity. Generally spoken, the finesse of optical cavities outruns the losses of optical fibers to date. However, the miniaturized cavity approach in this thesis is limited to the low laser power and to low pressures what renders the fiber method more sensitive in most common measurements.

1.5.5 Calcite Biomineralization by Bacterial Isolates

This publication [RK5] by the Limnology department of the Institute of Ecology in Jena is the predecessor of [RK1]. It evolved in a bilateral cooperation with the objective to investigate the bacterial cultures and biomineral precipitation. The recent opening of the pristine carstic Herrenberg cave allowed discovering an unperturbed habitat containing bacteria that lived in the absence of light for about twenty million years. The cave walls are covered by a microbiological active biofilm which rules the biomineralization process and substantially determines the actual shape of the cave.

Solid cave samples of different cave locations from stalactites, cave wall, ceiling and floor were taken and investigated by Fourier-Transform (FT)-Raman spectroscopy and FT-infrared (IR) spectroscopy for their mineral composition. 1064 nm FT-Raman was used, because it allows the fluorescence-free imaging of complex samples. As a result of IR-spectroscopy, the samples were separated into two groups: sediments and stalactite samples. The sediment samples consisted of a varying mixture of muscovite, quartz, and another component which may be dolomite, calcite or aragonite, what is hard to distinguish with IR-spectroscopy. The deformation vibration in FT-Raman spectroscopy finally determined the last component to be calcite. Only carbonate bands at 1450 cm^{-1} and 870 cm^{-1} were found in the IR spectra of stalactite samples. Again, these carbonates were identified to be calcite (bands at 1085 cm^{-1} and 713 cm^{-1}) by FT-Raman spectroscopy. FT-Raman imaging of a polished stalactite surface yielded a homogeneous undisturbed calcite distribution.

This cooperation was extended and one of nine isolated bacterial species (*Arthobacter sulfonivorans*) was investigated in more detail in terms of gas exchange and biomineralization in [RK1].

1.6 Conclusion and Outlook

The application of an innovative design of a miniaturized and extremely robust gas sensor based on cavity enhanced Raman spectrometry is introduced. The versatility of the new sensor allows online, simultaneous identification and quantification of various biogenic gases and volatiles in a wide range of concentrations and without cross-sensitivity. The different experiments in which this instrument has been applied demonstrate its stability for a range of important environmental research questions. In particular, the ability to simultaneously measure O_2 and N_2 besides other gases like CO_2 and the ability of real-time, in-situ measurements using isotope labels with a comparable inexpensive sensor is unique. The application of stable isotope tracers, such as used in the examples with ^{13}C, provides a powerful tool for understanding metabolic pathways, using low flow rates and small sample volumes in closed systems. All this is possible because Raman spectra are based on the characteristic inherent molecular vibrations of the measured gases such that the measurement does not influence or disturb the experimental site by the consumption of gases, labels or transducers. Fast analysis of gas exchange processes is possible, since time consuming sampling and sample preparation steps are not necessary. Also long-term gas observations can be performed due to stable linear calibration with no saturation and aging effects. It was shown that Raman gas spectrometry provides versatility, while at the same time portability is maintained by miniaturized instrument components and low power consumption. The comparably simple calibration and the straightforward handling allow focusing on the actual experiment rather than on the gas quantification. The experiments demonstrated that Raman spectrometry enables the simultaneous investigation of various gases produced and/or consumed by plants and microbes in controlled laboratory studies and in complex ecosystems. Miniaturization and low power consumption constitute a high potential for on-field measurement campaigns. This method is urgently needed and will contribute in the future to the elucidation of complex and strongly interdependent environmental processes.

1.7 Literature

1.   Dawson, T. E., Mambelli, S., Plamboeck, A. H. *et al.*, Stable Isotopes in Plant Ecology. *Annual Review of Ecology and Systematics* **33**, 507-559 (2002).
2.   Yakir, D. & Sternberg, L. d. S. L., The use of stable isotopes to study ecosystem gas exchange. *Oecologia* **123**, 297-311 (2000).
3.   Cuéllar, A. D. & Webber, M. E., Cow power: the energy and emissions benefits of converting manure to biogas. *Environmental Research Letters* **3**, 034002 (2008).
4.   Nordberg, A., Hansson, M., Sundh, I. *et al.*, Monitoring of a biogas process using electronic gas sensors and near-infrared spectroscopy (NIR). *Water Sci. Technol.* **41**, 1-8 (2000).
5.   Ohira, S. & Toda, K., Micro gas analyzers for environmental and medical applications. *Anal Chim Acta* **619**, 143-156 (2008).
6.   Seiyama, T., Nakahara, T. & Takeuchi, T., *Overview of Gas Sensors for Environmental Use*. (Elsevier, 1994).
7.   Yamazoe, N. & Miura, N., Environmental gas sensing. *Sensors and Actuators B: Chemical* **20**, 95-102 (1994).
8.   Davidson, E. A. & Janssens, I. A., Temperature sensitivity of soil carbon decomposition and feedbacks to climate change. *Nature* **440**, 165-173 (2006).
9.   Luo, Y., Wan, S., Hui, D. *et al.*, Acclimatization of soil respiration to warming in a tall grass prairie. *Nature* **413**, 622-625 (2001).
10.   Conrad, R., Soil microorganisms as controllers of atmospheric trace gases (H2, CO, CH4, OCS, N2O, and NO). *Microbiological reviews* **60**, 609-640 (1996).
11.   Rudaz, A. O., Wälti, E., Kyburz, G. *et al.*, Temporal variation in N2O and N2 fluxes from a permanent pasture in Switzerland in relation to management, soil water content and soil temperature. *Agriculture, Ecosystems & Environment* **73**, 83-91 (1999).
12.   Knowles, R., Denitrification. *Microbiology and Molecular Biology Reviews* **46**, 43-70 (1982).
13.   Smirnov, P. M., Kidin, V. V. & Pedishyus, R. K., Loss of nitrogen by denitrification. *Biology bulletin of the Academy of Sciences of the USSR* **6**, 450-459 (1979).
14.   Koerselman, W., The vegetation N: P ratio: a new tool to detect the nature of nutrient limitation. *Journal of Applied Ecology* **33**, 1441-1450 (1996).
15.   Wolfbeis, O. S., Fiber-optic chemical sensors and biosensors. *Analytical chemistry* **80**, 4269-4283 (2008).
16.   Modi, A., Koratkar, N., Lass, E. *et al.*, Miniaturized gas ionization sensors using carbon nanotubes. *Nature* **424**, 171-174 (2003).
17.   Suresh, S., Srivastava, V. & Mishra, I., Techniques for oxygen transfer measurement in bioreactors: a review. *Journal of Chemical Technology & Biotechnology* **84**, 1091-1103 (2009).
18.   Patterson, B. W., Zhang, X. J., Chen, Y. *et al.*, Measurement of very low stable isotope enrichments by gas chromatography/mass spectrometry: application to measurement of muscle protein synthesis. *Metabolism: clinical and experimental* **46**, 943-948 (1997).
19.   Berden, G., Peeters, R. & Meijer, G., Cavity ring-down spectroscopy: Experimental schemes and applications. *International Reviews in Physical Chemistry* **19**, 565-607 (2000).

20.	Thorpe, M. J., Moll, K. D., Jones, R. J. *et al.*, Broadband cavity ringdown spectroscopy for sensitive and rapid molecular detection. *Science (New York, N.Y.)* **311**, 1595-1599 (2006).

21.	Kanan, S. M., El-Kadri, O. M., Abu-Yousef, I. a. *et al.*, Semiconducting Metal Oxide Based Sensors for Selective Gas Pollutant Detection. *Sensors* **9**, 8158-8196 (2009).

22.	Gardner, J. W. & Bartlett, P. N., A brief history of electronic noses. *Sensors and Actuators B: Chemical* **18**, 210-211 (1994).

23.	Röck, F., Barsan, N. & Weimar, U., Electronic nose: current status and future trends. *Chemical reviews* **108**, 705-725 (2008).

24.	Dickinson, T. a., White, J., Kauer, J. S. *et al.*, *a chemical-detecting system based on a cross-reactive optical sensor array* (1996), Vol. 382, pp. 697-700.

25.	Rakow, N. a. & Suslick, K. S., A colorimetric sensor array for odour visualization. *Nature* **406**, 710-713 (2000).

26.	Kanu, A. B., Dwivedi, P., Tam, M. *et al.*, Ion mobility-mass spectrometry. *Journal of mass spectrometry : JMS* **43**, 1-22 (2008).

27.	Fenner, W. R., Hyatt, H. a., Kellam, J. M. *et al.*, Raman cross section of some simple gases. *Journal of the Optical Society of America* **63**, 73-73 (1973).

28.	Claps, R., Sabbaghzadeh, J. & Fink, M., Raman Spectroscopy with a Single-Frequency , High-Power , Broad-Area Laser Diode. *Applied Spectroscopy* **53**, 491-496 (1999).

29.	Schiel, D. & Richter, W., Use of Raman spectrometry in gas analysis. *Fresenius' Zeitschrift für Analytische Chemie* **327**, 335-337 (1987).

30.	Li, X., Xia, Y., Zhan, L. *et al.*, Near-confocal cavity-enhanced Raman spectroscopy for multitrace-gas detection. *Optics letters* **33**, 2143-2145 (2008).

31.	King, D. a. & Pittaro, R. J., Simple diode pumping of a power-buildup cavity. *Optics letters* **23**, 774-776 (1998).

32.	Ohara, S., Yamaguchi, S., Endo, M. *et al.*, Performance Characteristics of Power Build-up Cavity for Raman Spectroscopic Measurement. *Optical review* **10**, 342-345 (2003).

33.	Lewis, I. R. & Edwards, H. G. M., *Handbook of Raman Spectroscopy: From the Research Laboratory to the Process Line*. (Marcel Dekker, 2001).

34.	Larkin, P., *Infrared and Raman Spectroscopy: Principles and Spectral Interpretation*, 1st edition ed. (Elsevier, 2011).

35.	Demtröder, W., *Laser Spectroscopy: Vol. 2: Experimental Techniques*, 4th edition ed. (Springer Berlin Heidelber, 2008).

36.	Long, D. A., *The Raman Effect: A Unified Treatment of the Theory of Raman Scattering by Molecules*. (John Wiley & Sons, 2002).

37.	Alsmeyer, F., Koss, H. J. & Marquardt, W., Indirect spectral hard modeling for the analysis of reactive and interacting mixtures. *Appl Spectrosc* **58**, 975-985 (2004).

38.	Livingston, G. P., Hutchinson, G. L. & Spartalian, K., Trace Gas Emission in Chambers. *Soil Science Society of America Journal* **70**, 1459 (2006).

39.	Hutchinson, G. L. & Livingston, G. P., Vents and seals in non-steady-state chambers used for measuring gas exchange between soil and the atmosphere. *European Journal of Soil Science* **52**, 675-682 (2001).

40.	Control, D. o. M. a., *Climatological Station*, edited by University of Applied Sciences Jena (Jena, 2012).

2 Zusammenfassung

Die Cavity-verstärkte Raman-Spektrometrie ist eine neue Technik mit vielen Vorteilen gegenüber den etablierten Gasmesstechniken. Die sensitive Gasdetektion durch Raman-Spektroskopie ist eine besondere Herausforderung, da Gase im Vergleich zur kondensierten Phase eine besonders niedrige Moleküldichte aufweisen und zusätzlich nur wenige Photonen inelastisch, im Sinne des Raman-Effekts, gestreut werden. Die Verstärkung der Lichtintensität durch eine optische Cavity macht die Raman-Spektroskopie für die anwendungsorientierte Quantifizierung von Gasen nutzbar, indem der niedrige Streuquerschnitt durch eine um drei bis vier Größenordnungen höhere Lichtintensität kompensiert wird. Durch diesen Aufwand werden die Vorteile der Raman-Spektroskopie für die Gasanalytik zugänglich. Zu den Vorteilen gehört die Universalität, das heißt die Fähigkeit nahezu alle Gase simultan zu quantifizieren. Diese resultiert aus der speziellen Auswahlregel der Raman-Streuung, dass sich die Polarisierbarkeit der Moleküle während der Schwingung ändern muss. Diese wird von allen mehratomigen Gasmolekülen erfüllt. Keine andere Technik ist in der Lage diese Fülle von Gasen abzudecken. Insbesondere die homoatomaren Gase sind mit herkömmlichen Techniken schwierig zu quantifizieren und es werden Speziallösungen notwendig, welche sich dann meist auf ein einzelnes Gas beschränken. Zu den interessanten zweiatomigen Gasen gehören Stickstoff, Sauerstoff und Wasserstoff und deren Isotope. Diese und andere Gase können mit einer hohen Messgeschwindigkeit online bis zu 30 Hz erfasst werden, was durch die schnelle optische Technik und schnelle Elektronik realisiert wird. Dies spielt vor allem bei schnellen Änderungen der Gaskonzentrationen eine Rolle. Die Gaskonzentrationen skalieren linear mit analytischen Kenngrößen wie der Bandenhöhe beziehungsweise der Bandenfläche, was am Beispiel Kohlendioxid gezeigt wurde. Für die Bestimmung der Gaskonzentrationen wurde ein least-square Fit des gesamten Spektrums durchgeführt, was zusätzlich zum verbesserten Signal-Rausch-Verhältnis die ohnehin sehr gute Spezifität weiter steigert indem zusätzlich schwache aber sehr spezifische Banden zur automatisierten Auswertung hinzugezogen werden. Diese extreme Spezifität wird durch die sehr gute Unterscheidbarkeit der chemisch fast identischen Isotope deutlich. Auch das Isotopensignal skaliert linear mit der Konzentration. Die Linearität ermöglicht eine einfache, schnelle und günstige Einpunktkalibration mit Reingasen und mit hinreichender Genauigkeit für die meisten Anwendungen, wie im

weiteren Verlauf der Arbeit gezeigt wird. Die hohe Linearität ist der Raman-Streuung inhärent und umfasst den gesamten dynamischen Bereich. Der dynamische Bereich reicht von reinen Gasen bis zu einer Konzentration von etwa 50 ppm (gasabhängig) und umfasst damit fast sieben Größenordungen, was den meisten anderen Gasmesstechniken weit überlegen ist. Die Methode wurde durch drei Punkte validiert: Blindwert, Reingas und mittels eines zertifizierten Testgases, welches aus einer Mischung aus fünf Gasen mit einer Volumenkonzentration von je einem Prozent bestand.

Diese neue Gasmesstechnik wurde in verschiedenen Experimenten getestet. Zuerst wurde der respiratorische mikrobielle Gasumsatz von *Pseudomonas* sp. und *Arthrobacter* sp. quantifiziert [RK1]. Durch die Gasmessungen konnten die herkömmlichen Messungen der optischen Dichte zur Bakterienzahlbestimmung mit den Atmungsraten verglichen werden. Die Atmungsraten beinhalten sowohl Sauerstoff als auch Kohlendioxid und zeigten die gleiche bakterielle Lag-Phase an, waren aber im weiteren Verlauf des Experiments unbeeinflusst von Trübungen durch die Fällung von Calciumcarbonat. Die Atmungsraten korrelierten mit dem Lebenszyklus der Bakterien. Das einstufige Bakterium hatte ein Maximum in der Aktivität, das zweistufige zeigte zwei Maxima. Die Atmungsmessungen profitieren hierbei von der simultanen Quantifizierung von Sauerstoff und Kohlendioxid.

Neben der Atmung besitzt die Isotopenmarkierung eine große Bedeutung für die Aufklärung von Stoffwechselvorgängen in Organismen. Pflanzen werden oft mit $^{13}CO_2$ markiert, welches photosynthetisch assimiliert wird. In einem übergeordneten Experiment sollte mittels $^{13}CO_2$-Markierung geklärt werden, ob die Verteidigungsmechanismen einer Pappelart aus gespeicherten oder aus frisch synthetisierten Abwehrstoffen basiert. In [RK2] war es dazu wichtig, zwischen $^{12}CO_2$ und $^{13}CO_2$ diskriminieren zu können. Die $^{13}CO_2$ Markierung wurde verfolgt und wichtige Daten konnten online erhalten werden. Dazu gehören die maximale CO_2-Konzentration, welche einen bestimmten Wert nicht übersteigen sollte und die Dauer der $^{13}CO_2$-Aufnahme für das Timing des Experiments. Im Anschluss konnte die gleiche Methode für die Quantifizierung der Dunkelatmung verwendet werden. Es stellte sich heraus, dass junge Blätter eine fast doppelt so hohe Atmungsaktivität im Vergleich zu ausgewachsenen Blättern haben und dass der respiratorische Quotient, ein wichtiger

Indikator für die Art des verbrannten Substrats, bei eins lag, was für die Verbrennung von Kohlenhydraten, z.B. Stärke, schließen lässt.

Die Messung von mehreren Gasen inklusive derer Massenisotope kann zur Kenntnis von mehreren Parametern eines Systems führen. Das kann zur umfassenden Charakterisierung von komplexen Systemen genutzt werden. Stellvertretend für ein komplexes Ökosystem war eine Torfmoorprobe in einem Mesokosmos [RK3]. Diese Probe bestand aus einer grünen Pflanze (Torfmoos), einer hochatmungsaktiven wassergesättigten Torfschicht, welche methanogene Mikroorganismen in anoxischen Mikrozonen enthielt. Durch das Gas-Monitoring bei drei verschiedenen Lichtverhältnissen konnten viele spezifische Parameter in kürzester Zeit erhalten werden, wie die maximale Photosyntheseaktivität des Torfmooses, die Dunkelatmungsrate des Torfmooses, die Bodenatmungsrate und die Methanogeneserate.

Zuletzt wurde die Cavity-verstärkte Raman-Spektrometrie mit der faserverstärkten Ramanspektrometrie verglichen [RK4]. Dabei stellte sich heraus, dass der Cavity-basierte Ansatz energieeffizienter und miniaturisierbarer ist, wohingegen die Verstärkung mit einer photonischen Hohlkernfaser zu deutlich verringerten Nachweisgrenzen und niedrigeren Probenvolumina führt.

Zusammenfassend zeigt diese Arbeit, dass die Cavity-verstärkte Raman-Gasspektrometrie ein wertvolles Instrument für die Quantifizierung von biogenen Gasen in den verschiedensten Anwendungsszenarios ist. Diese Methode hat das Potenzial neben der Gaschromatografie eine universelle Standardgasanalysemethode in der analytischen Chemie zu werden.

3 Publications

The publications are structured by the intricacy of the investigated biological system. The first three publications [RK1...3] describe the application of Raman gas sensing to respiring bacteria [RK1], photosynthesis and isotope monitoring [RK2] and monitoring of a complex ecosystem [RK3]. The benefits of utilizing an optical fiber to enhanced Raman gas spectrometry was evaluated in [RK4]. In the collaboration publication [RK5], we contributed Raman and infrared measurements of solid biogenic samples. This collaboration was extended to Raman gas measurements in the headspace of bacteria, which eventually led to the publication of [RK1].

3.1 Raman Spectroscopy - An Innovative and Versatile Tool To Follow the Respirational Activity and Carbonate Biomineralization of Important Cave Bacteria [RK1]

Robert Keiner, Torsten Frosch, Stefan Hanf, Denise M. Akob, Kirsten Küsel, Jürgen Popp

Raman Spectroscopy—An Innovative and Versatile Tool To Follow the Respirational Activity and Carbonate Biomineralization of Important Cave Bacteria

Robert Keiner,[†,‡,∇] Torsten Frosch,*[,†,‡,∇] Stefan Hanf,[†,‡] Anna Rusznyak,[§] Denise M. Akob,[§,⊥] Kirsten Küsel,[§] and Jürgen Popp[†,‡,‖]

[†]Institute of Photonic Technology, [‡]Institute for Physical Chemistry, [§]Institute of Ecology, and [‖]Abbe School of Photonics, Friedrich Schiller University, Jena, Germany

Ⓢ *Supporting Information*

ABSTRACT: Raman gas spectrometry is introduced as a unique tool for the investigation of the respiratory activity that is indicative for growth of bacteria involved in biomineralization. Growth of these bacteria cannot be monitored using conventional turbidity-based optical density measurements due to concomitant mineral formation in the medium. The respiratory activity of carbonate-precipitating *Arthrobacter sulfonivorans*, isolated from the recently discovered Herrenberg Cave, was investigated during its lifecycle by means of innovative cavity-enhanced Raman gas analysis. This method allowed rapid and nonconsumptive online quantification of CO_2 and O_2 in situ in the headspace of the bacterial culture. Carbon dioxide production rates of *A. sulfonivorans* showed two maxima due to its pleomorphic growth lifecycle. In contrast, only one maximum was observed in control organism *Pseudomonas fluorescens* with a one-stage lifecycle. Further insight into the biomineralization process over time was provided by a combination of Raman macro- and microspectroscopy. With the help of this spatially resolved chemical imaging of the different types of calcium carbonate minerals, it was elucidated that the surface of the *A. sulfonivorans* bacterial cells served as nuclei for biomineralization of initially spherical vaterite precipitates. These vaterite biominerals continued growing as chemically stable rock-forming calcite crystals with rough edges. Thus, the utilization of innovative Raman multigas spectroscopy, combined with Raman mineral analysis, provided novel insights into microbial-mediated biomineralization and, therefore, provides a powerful methodology in the field of environmental sciences.
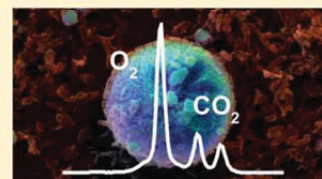
The recent discovery of the Herrenberg Cave in the Thuringian Forest (Germany) opened a unique opportunity to study an undisturbed and unexplored microbial population, which developed in the total absence of light. Karstic areas, such as the Herrenberg Cave, are carbonate-dominated and represent one of the most important subterranean carbon reservoirs.[1] This window into the subsurface provides the possibility of elucidating the role of microbes in the earth's Critical Zone[2] processes, such as the lifecycle and biomineralization of carbonate-precipitating cave bacteria.[3] The biomineralization[4] of calcium carbonates occurs at the cave walls and can be mediated either by chemical changes, caused by the metabolic activity of the microorganisms, or by providing nucleation sites for mineralization at the microbial cell surface or metabolic products.[5]

Arthrobacter species were detected not only in soils and the deep subsurface but also in extreme environments, such as the arctic ice or chemically contaminated sites.[6] The ubiquitous presence of these bacteria in various environments is caused by their ability to survive stress during long periods of time (e.g., starvation, temperature shifts, and desiccation), as well as by their metabolic diversity.[7] Members of the genus *Arthrobacter* are strictly aerobic bacteria with a pleomorphic lifecycle. They show Gram-negative rod morphology in younger cultures, and the cells of older cultures appear as Gram-positive cocci (Figure

SM1, Supporting Information). The *A. sulfonivorans* strain, SCM3, that was isolated from solid clay material (SCM)[3g] grows as aggregates, and it produces extracellular polymeric substances (EPS), which might serve as nucleation sites for biominerals. Calcium carbonate precipitation was detected not only in the laboratory by a variety of bacteria[8] but also in numerous environments, such as soils, caves, lakes, and seawater.[9] Three forms of calcium carbonate minerals are known: calcite, vaterite, and aragonite. Calcite is the major rock-forming mineral, while vaterite is a rare and metastable mineral below 400 °C.[10] Aragonite precipitates under elevated temperatures and is found as a component of the hard parts of many marine microorganisms, including shells and skeletons.[11] Bacterial calcium carbonate formation is applied in contaminated soil and groundwater remediation,[12] the protection and repair of concrete and cement structures,[13] and the conservation of building stone and statuary.[14] Thus, detailed investigations of growth characteristics of carbonate-precipitating microorganisms and their products will be of high interest.

However, the characterization of the metabolic activity of these mineral precipitating microorganisms is challenging because growth monitoring by conventional turbidity-based optical density measurements can be masked due to the concomitant mineral formation in the medium. Furthermore, direct cell counting by fluorescence spectroscopy is often disturbed by autofluorescence of the minerals formed. An elegant way for characterizing the metabolic activity of microbial cultures, including mineral precipitates, is the quantification of the gas exchange during their growth[16,17] (e.g., the consumption of oxygen and release of carbon dioxide over time). Common methods for the quantification of gaseous oxygen rely on chemical (Winkler's method), as well as electrochemical, analysis (Clark probe),[15] and carbon dioxide is often measured electrochemically[16] or by nondispersive infrared (NDIR) absorption.[17] Devices based on IR absorption spectroscopy evolved as sensitive gas sensors in recent years,[18,19] but they lack the capability for analysis of homonuclear diatomic gases, such as O_2, N_2, and H_2. Other lab-based instruments, such as GCMS, combine separation steps with the help of special columns in gas chromatography (GC)[20] and successive identification by means of mass spectrometry (MS). These devices are extremely sensitive but also bulky and expensive, and they rely on gas sampling and are limited in terms of fast and nonconsumptive identification of various gases simultaneously.

Our novel approach is Raman spectroscopy, which emerged as an extremely powerful method in various natural science disciplines.[21] This technique is based on characteristic molecular vibrations[22] and is widely established for the analysis of liquid and solid samples.[23] Innovative Raman gas spectrometry[24] will, therefore, be introduced as a novel technique for fast and nonconsumptive quantification of microbial gas exchange[3f] in order to characterize the respirational activity of *A. sulfonivorans* SCM3 during its lifecycle.

■ MATERIALS AND METHODS

Cultivation of Bacteria. The mineral-precipitating bacteria were grown in hermetically sealed bottles in order to observe the gas exchanges in a batch experiment. In doing so, the input is initial and single-term. No elimination by out-washing occurs, and the spatial organization of the population is homogeneous.

Strain SCM3, identified as *A. sulfonivorans*, was isolated from the solid clay material (SCM) of the sediment in the Herrenberg Cave.[3g] The isolate SCM3 (National Centre for Biotechnology Information (NCBI) sequence accession number FR669674) was cultivated in B4 medium containing 2.5 g of calcium acetate, 10 g of glucose, and 4 g of yeast extract per liter (pH 7.5) at room temperature in the dark.[3h] For Raman analysis, 1 L serum bottles containing 200 mL of B4 medium were inoculated with 5 mL of 24 h cultures of the *A. sulfonivorans* strain grown in B4 medium. After inoculation, the bottles were sealed and incubated at room temperature in the dark with stirring at 150 rpm. Noninoculated sterile medium and dead-cell-inoculated medium were used as negative controls.

P. fluorescens strain AH1 was isolated from an acidic fen located in northern Bavaria, Germany, on *Pseudomonas* (PS) medium, containing 20 g of peptone from meat, 2.99 g of $MgCl_2 \times 6 H_2O$, and 20 mL of glycerol per liter (pH 7). For Raman analysis, *P. fluorescens* was cultivated in 1 L serum bottles containing 200 mL of PS medium and inoculated with 2 mL of 48 h culture grown in PS medium. Duplicate inoculation

and uninoculated control bottles were sealed and incubated at room temperature in the dark with stirring at 150 rpm.

In order to keep the intact headspace within the bottles during the Raman gas experiment, parallel cultures were grown for sampling for optical density (OD) measurements. From the liquid medium, 1 mL was sampled daily for OD measurements and for the preparation of mineral samples. The OD was measured at wavelength $\lambda = 560$ nm with a two-beam UV−vis absorption spectrometer (Specord M400, Carl Zeiss, Jena, Germany).

Raman Gas Spectrometry. Online gas measurements were carried out in the headspace of a 1 L serum bottle. At the beginning, the system was checked for pressure tightness, and the total gas volume was measured simultaneously by injecting a defined volume of gas (e.g., air) into the system and recording the pressure over time. The pressure leap then relates to the total volume, and the decrease of pressure over time corresponds to the leak rate. The whole experiment was carried out in a temperature-controlled environment to avoid the influence of temperature variations on the respirational activity. Therefore, the temperature was held constant at 25 ± 0.5 °C in a regulated oven (Heraeus HT 4004). The composition of the gas phase was measured very rapidly (1 s) in order to observe even sudden gas changes.

The originally small inelastic scattering signals of the gas molecules (with low concentration) were increased by 5 orders of magnitude by means of innovative cavity-enhanced Raman spectrometry (CERS). Briefly, a laser diode ($\lambda = 650$ nm, 50 mW) was passively frequency-locked and feedback-coupled to a high finesse power-build-up cavity to achieve strong signal enhancement. The Stokes Raman intensity depends on the laser intensity (I_0) the angular frequencies of the laser (ω_L) and the scattered light (ω_S), as well as the polarizability (α) of the molecule and the molecule concentration (C).

$$I_{Stokes} \sim C * I_0 * (\omega_L - \omega_S)^4 * |\alpha|^2 \qquad (1)$$

The laser intensity and also the parameter temperature and absolute pressure were measured with additional sensors because the concentration (C) of an ideal gas is influenced by temperature (T) and (partial) pressure (p). Raman scattering offers excellent linearity with analyte concentration (eq 1) and allows for robust instrument calibration and gas quantification. Therefore, a one-point calibration of the device was proven to be reliable by measuring pure gaseous oxygen and carbon dioxide as reference gases. The concentrations of the individual gases in the experimentally acquired multicomponent gas mixture were derived by solving the according linear equation system and least-squares fitting with the calibration spectra. The magnitude of concentration fluctuations that can be monitored is in the range of 100 ppm. Raman spectra were taken with 1 s integration time.

Raman Spectroscopy and Chemical Imaging of Mineral Precipitates. Raman spectra of the samples containing mineral precipitates were acquired with a NIR-Raman macro setup ($\lambda_{exc} = 1064$ nm), as well as a micro-Raman setup with visible excitation ($\lambda_{exc} = 532$ nm). In addition, Raman spectra of pure reference samples of calcite and aragonite were measured for comparison, which were kindly provided by the Mineralogische Sammlung Jena.

The macro setup was used to characterize an area of 0.5 mm^2 in one single measurement, such that the obtained Raman spectra represent the averaged sample composition. An excitation wavelength in the NIR ($\lambda_{exc} = 1064$ nm) was used

in order to avoid excitation of fluorescence in the complex sample. The spectra were acquired with a FT-Raman spectrometer (Bruker, Ram II) equipped with a macrolens (IR352) and a liquid-nitrogen-cooled Ge detector.

Micro-Raman spectroscopy with visible excitation (λ_{exc} = 532 nm) was applied in order to target individual calcium carbonate crystals and allow for the generation of spatially resolved chemical Raman maps. The Raman spectra were acquired with a confocal micro-Raman setup (LabRam HR800, Horiba) equipped with an Olympus BX41 microscope and a liquid-nitrogen-cooled CCD detector. A 100x/0.9 Olympus micro-scope objective was used to focus the laser light onto individual crystals and to collect the backscattered Raman signals. In doing so, spectra with high signal-to-noise-ratio were acquired. In order to build up chemical images of the spatial distribution of the minerals, the sample was scanned relative to the laser focus with the help of a motorized x/y-stage, and Raman spectra were recorded at every spot.

■ RESULTS AND DISCUSSION

Raman Gas Spectroscopic Investigation of the Life-cycle of Carbonate Precipitating *A. sulfonivorans*. As explained in the introduction, it is of high interest to investigate the details of the lifecycle and biomineralization process of bacterial isolates like *A. sulfonivorans* SMC3 obtained from the Herrenberg Cave. However, the growth of this microbe cannot be analyzed by absorption measurements due to concomitant mineral formation, which affects the measured optical density (OD) values. Therefore, a novel approach is introduced—namely, cavity-enhanced Raman gas analysis—in order to provide very detailed information about the respirational activity of *A. sulfonivorans* by characterizing the multigas composition in the headspace of the bacterial culture, without sampling or gas consumption.

In doing so, the absolute amounts of O_2 and CO_2 were quantified continuously over the course of the lifecycle of *A. sulfonivorans* SCM3. An experimentally derived Raman spectrum is shown in Figure 1. The rotational−vibrational Raman spectrum of O_2 centered at 1555 cm^{-1} consists of a strong Q-band (no change in rotation), as well as P and O branches (altered rotational levels), which are not spectrally resolved. A Fermi resonance[25] occurs in the spectrum of CO_2, where the overtone of the deformation vibration at 2 × 667

Figure 1. Experimentally derived Raman spectrum of the gases O_2 and CO_2, which was quantified continuously during the lifecycle of *A. sulfonivorans* SCM3. Simultaneous multigas quantification was possible due to the spectral separation of the Raman bands of the individual gases.

cm^{-1} = 1334 cm^{-1} is located near the symmetric valence vibration at 1337 cm^{-1}. This increases the energetic distance between the two modes and transfers intensity from the stronger to the weaker mode, and it finally leads to the doublet peak at 1285 and 1388 cm^{-1}. The gas peaks of O_2 and CO_2 are spectrally well-separated and can be identified and quantified simultaneously. The N_2 content was also quantified continuously (not shown in Figure 1) and was exploited as a constant internal standard.

The gas concentrations of O_2 and CO_2 were equal to ambient conditions at the beginning of the incubation (Figure 2A). The amount of O_2 decreased at the end of the lag time at 32 h when the concentration of CO_2 was increasing. In order to monitor the activity of *A. sulfonivorans* during the incubation, the CO_2 production rate was calculated by differentiation of the CO_2 concentration with respect to time (Figure 2B). Interestingly, CO_2 production rates close to zero were detected at the beginning of the incubation, but two maxima appeared after 51.3 and 79.6 h. These two CO_2 maxima can be explained by two stages of respirational activity in the pleomorphic lifecycle of *A. sulfonivorans*. Thus, the novel application of Raman gas analysis was very useful for analyzing the respirational processes quickly and continuously, such that intermediate changes in the activity of *A. sulfonivorans* were revealed (Figure 2A,B). As the microbial system turned hypoxic, the CO_2 production rate dropped, indicating a diminishing microbial respirational activity (Figure 2B).

In order to compare the microbial activity of *A. sulfonivorans* with a bacterium that has no pleomorphic lifecycle, the respiration of *P. fluorescens*, which has only a single-stage lifecycle, was analyzed in a similar experiment. The concentrations of O_2 and CO_2 were again monitored in the sample headspace over time (Figure 2C), and the CO_2 production rate was calculated (Figure 2D). After a lag phase of 5 h, the CO_2 production rate of *P. fluorescens* showed only one maximum (Figure 2D) during the incubation experiment, in contrast to the results of *A. sulfonivorans* (Figure 2B), suggesting differences between the lifecycles of the two species.

Taking advantage of the simultaneous acquisition of the O_2 and CO_2 concentrations, the respiratory quotient (RQ) was quantified, which is defined as the ratio of mol of CO_2 evolution consumed per mol of O_2 uptake. The RQ value is an important parameter for characterizing microbial metabo-lism because it reflects the oxygen content of substrates such as low-O-containing amino acids or high-O-containing root exudates.[26] Oxygen and carbon dioxide concentrations acquired for the two different bacteria, *A. sulfonivorans* and *P. fluorescens* (Figure 2A,C), and RQ values always less than one were in good agreement with those of the amino acid oxidation.

Investigation of Calcium Carbonate Biomineralization by Means of Raman Mineral Analysis. In order to investigate more thoroughly the biomineralization of calcium carbonates, which may be important for rock formation in karstic caves, the gas analysis of the respirational activity of *A. sulfonivorans* was supported by Raman mineral analysis. The initial microcrystals, which were detected in the *A. sulfonivorans* culture, were spherically shaped with a diameter of about 3 μm (Figure 3B). However, light microscopic inspection (Figure 3B) did not allow us to distinguish between different forms of calcium carbonate precipitates (calcite, vaterite, or aragonite). Vaterite also could not be localized easily by electron microscopy or other techniques that rely on vacuum conditions because vaterite transforms to calcite under vacuum within a
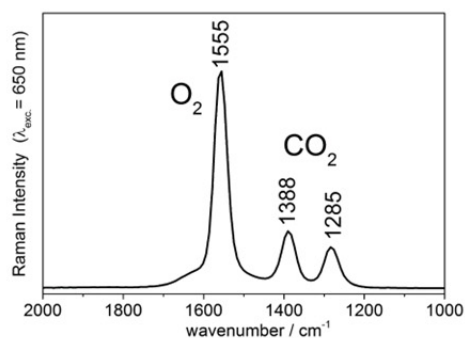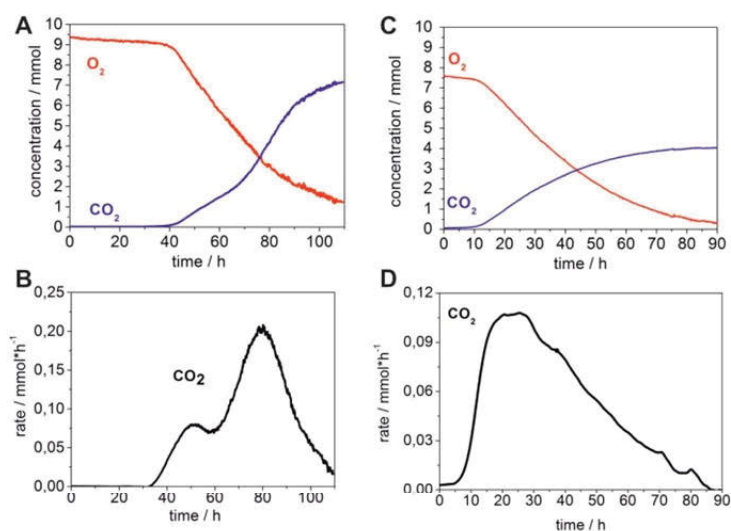
Figure 2. Raman spectroscopic monitoring of the headspace gas composition during the lifecycles of *Arthrobacter sulfonivorans* and *Pseudomonas fluorescens*. (A,C) Gas compositions of O_2 and CO_2 in the sample headspace, characterizing the respirational activity of *A. sulfonivorans* (A) and *P. fluorescens* (C) during the lifecycles. (B,D) Carbon dioxide production rates show two maxima for *A. sulfonivorans* (B), which has a pleomorphic lifecycle, whereas only one maximum is seen for *P. fluorescens* (D), which has a single-stage lifecycle.
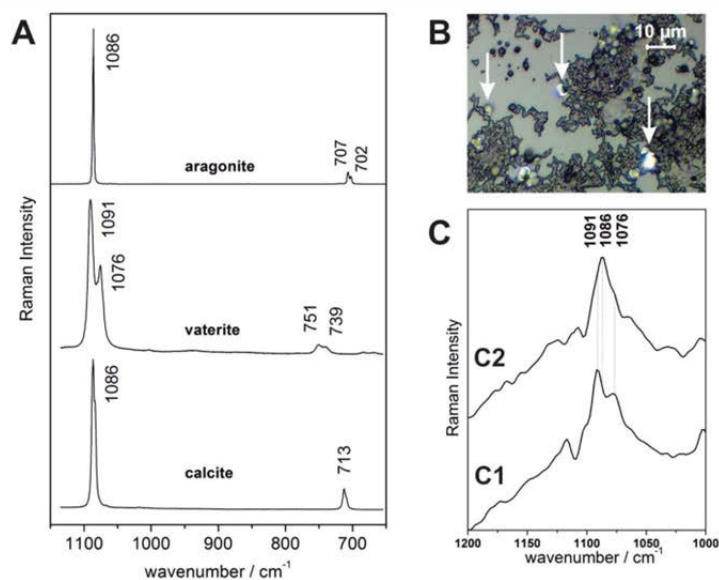

Figure 3. Raman spectroscopic investigation of calcite biominerals. (A) Raman spectra of pure reference minerals (aragonite, vaterite, and calcite), which are distinguished on the basis of their specific Raman bands. (B) White light image of *A. sulfonivorans* and precipitated vaterite microcrystals. Arrows indicate spherulitic microcrystal aggregates. (C) Raman spectra in the spectral window of the symmetric stretching vibrations of carbonate precipitates after 16 (C1) and 22 days (C2). These Raman spectra illustrate the transformation of initial vaterite bioprecipitates (Raman bands at 1091 and 1076 cm^{-1}) into chemically stable calcite microcrystals (Raman band at 1086 cm^{-1}).

few seconds. Therefore, a combination of macro- and micro-Raman spectroscopy was applied to detect intermediate vaterite appearance and to quantify the amount and the type of calcium carbonate precipitates, as well as their spatial distribution, by means of Raman chemical imaging. Raman spectra of pure reference samples of calcite and aragonite, as well as vaterite biocrystals, were acquired and are shown in Figure 3A and summarized in Table 1. All three calcium carbonates were

distinguished with the help of their specific carbonate stretching and bending vibrations.

Raman macrospectroscopy was exploited to average across many crystals simultaneously, such that the successive appearance of vaterite and calcite was quantified in the whole sample at once (Figure 3C). The excitation wavelength $\lambda_{exc} = 1064$ nm was chosen for macro-Raman spectroscopy in order to avoid the occurrence of fluorescence in the complex heterogeneous sample containing bacteria, medium, and

Table 1. Raman Peak Positions (Values Are Given in Wavenumbers/cm^{-1}) and Band Assignments for Calcium Carbonate Minerals Calcite, Vaterite, and Aragonite[27] (See Figure 3A)

	calcite	vaterite	aragonite
$\bar{v}_{asymmetric}$ CO_3^{2-}	1432		1462
$\bar{v}_{asymmetric}$ CO_3^{2-}	1086	1091, 1076	1086
$\bar{v}_{in\text{-}plane\ bending}$ CO_3^{2-}	714	751, 739	707, 702
$\bar{v}_{lattice}$	283, 156	333–106	284–144

mineral precipitates. During the first days of inspection, only low concentrations of minerals were present—leading to weak Raman signals. However, as the number and size of crystals grew with time, stronger signals of the precipitate minerals were observed in the macro-Raman spectra. After a few days, a Raman doublet at 1091 and 1076 cm^{-1} appeared, indicating the precipitation of vaterite by *A. sulfonivorans* (Figure 3C1, Table 1). The intensity of this doublet increased within the next days. During the following days, a Raman band at 1086 cm^{-1} also increased successively (Figure 3C2, Table 1). These results revealed that *A. sulfonivorans* SCM3 initially precipitated pure vaterite biominerals, which transformed into stable calcite crystals later.

In order to investigate the chemical transformation of calcium carbonate minerals from initial vaterite biocrystals into stable rock-forming calcite more thoroughly, the spatial distribution of the minerals and their geometric shapes were investigated with Raman microspectroscopy. An excitation wavelength in the visible range at λ_{exc} = 532 nm was applied to achieve a higher spatial resolution, which is required for

targeting individual calcium carbonate microcrystals. A suitable cluster of minerals was chosen for light microscopy (Figure 4A). Raman spectra were acquired across an area of about 20 × 15 μm. The analysis of the array of Raman spectra, recorded across this sample area, allowed for the generation of Raman maps, which displayed the individual minerals. The chemical Raman image, created by plotting the integrated intensity over a wavenumber range from 700 to 800 cm^{-1} (Figure 4B), represented the spatial distribution of all three types of calcium carbonate minerals (see Figure 3A). The depth of focus of the applied microscope is in the micrometer range, such that crystals that are not located in the focal plane produce only low Raman signals and are not visible in the Raman images. A closer look at Figure 3A showed that Raman microspectroscopy also allowed us to distinguish between different types of calcium carbonate in the low wavenumber range. Consequently, the chemical images of calcite (integrated intensity of the wavenumber range of 705–720 cm^{-1}) and vaterite (integrated intensity of the wavenumber range of 730–755 cm^{-1}) are shown in Figure 4C,D, respectively. These images revealed that biogenic vaterite crystals formed spherically shaped micro-aggregates (Figure 4D). The Raman maps also indicated that biogenic vaterite crystals serve as seed crystals for abiotic calcite growth with rough edges (Figure 4C). This process is likely to happen in karstic caves and could explain the preferential growth of a variety of small crystallites, in contrast to Ostwald's rule (Figure 4).

■ CONCLUSIONS AND OUTLOOK

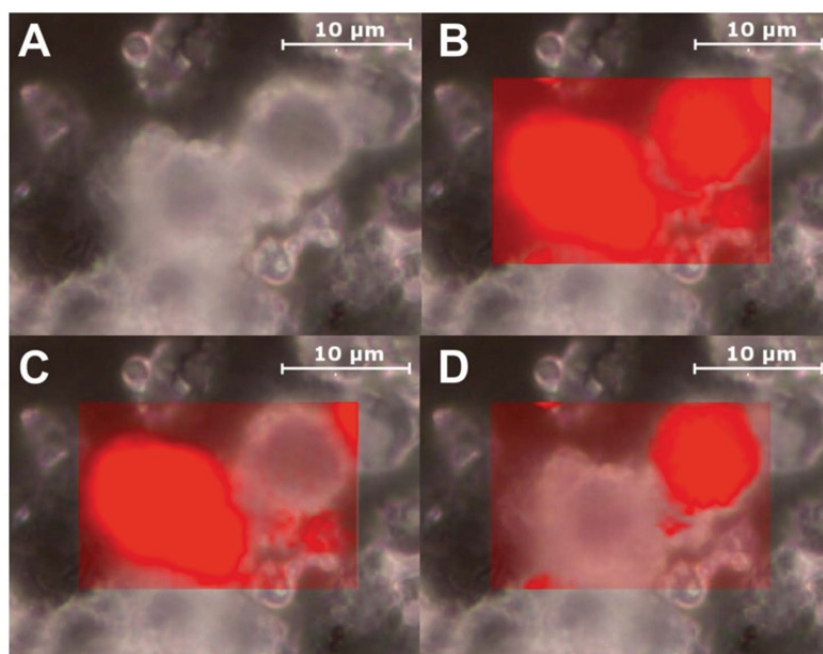The combination of innovative Raman multigas sensing, as well as Raman macro- and microspectroscopy, was exploited to

Figure 4. (A) White light microscopic image of vaterite and calcite microcrystals in a sample area of 30 × 30 μm^2. (B) White light image overlaid with chemical Raman image of carbonate precipitates (wavenumber range: 700–800 cm^{-1}). (C,D) Chemical images of calcite distribution (C) (wavenumber range: 705–720 cm^{-1}, with calcite band at 715 cm^{-1}) and of vaterite distribution (D) (wavenumber range: 730–755 cm^{-1}, with vaterite bands around 750 cm^{-1}). Vaterite and calcite crystals are not distinguishable in the white light image (A), but they can be imaged with chemical selectivity (C,D) with the help of their distinctive Raman bands.

elucidate details of the growth characteristics and the concomitant carbonate precipitation activities of the cave bacterium *Arthrobacter sulfonivorans* SCM3.

Cavity-enhanced Raman gas spectrometry was utilized as an extremely versatile technique for fast and continuous online quantification of CO_2, together with O_2, in the headspaces of *A. sulfonivorans* and *P. fluorescens* cultures, without sampling, gas consumption, or the drawbacks of turbidity-based optical density measurements. Two developmental stages with different respirational activities were discovered within the pleomorphic lifecycle of *A. sulfonivorans*, in contrast to the respiration of *P. fluorescens*, which possesses a single-stage lifecycle. The respiratory quotient (RQ) was quantified for both bacterial genera by taking advantage of the simultaneous quantification of O_2 and CO_2 concentrations, and the RQ value was in good agreement with the theory of amino acid oxidation. These important details may have been missed by conventional OD measurements due to concomitant precipitation of biominerals during the developmental cycle of the cave bacteria *A. sulfonivorans*. In comparison to chromatographic methods, which rely on the extraction of gas samples, Raman gas measurements offer a higher degree of reliability because no gas is consumed in the closed-cycle experiment.

The precipitation of calcium carbonate biominerals by *A. sulfonivorans* was further investigated with the help of combined Raman macro- and microspectroscopy. NIR Raman macrospectroscopy was hereby exploited for quantification of the individual calcium carbonates across a representative sample area. These average results demonstrated quantitatively that *A. sulfonivorans* SCM3 precipitates initially pure vaterite biominerals, which transform into chemically stable rock-forming calcite crystals later. Raman microspectroscopy provided further detailed insight into the geometrical shape and spatial distribution of the precipitates. These chemical images elucidated that biogenic vaterite crystals appear as spherically shaped microaggregates and serve as nuclei for further crystallization of calcite crystals with rough edges. These results nicely demonstrate the potential of chemical-selective Raman analysis for nondestructive onsite investigations of biomineralization processes in natural habitats, such as karstic areas or caves.

In summary, it was demonstrated that innovative Raman multigas spectrometry is a capable technique for non-consumptive, time-resolved investigation of microbial respirational activities and can help to elucidate intermediate details, which might be overlooked by conventional sampling techniques. In the future, Raman gas sensing could assist in activity measurements for other microorganisms involved in biomineralization (e.g., iron-oxidizing bacteria), where conventional growth measurements and fluorescence microscopic approaches are hindered due to autofluorescence of iron oxides within the media. In addition, a whole suite of further Raman gas experiments can be imagined, where simultaneous multigas quantification (e.g., N_2, N_2O, CO_2, O_2, CH_4, H_2) might provide novel insights into processes such as respiration, photosynthesis, or methanogenesis.

ASSOCIATED CONTENT

Supporting Information

Additional information as noted in the text. This material is available free of charge via the Internet at http://pubs.acs.org.

AUTHOR INFORMATION

Corresponding Author
*E-mail: torsten.frosch@uni-jena.de.

Present Address
[1]Denise M. Akob: U.S. Geological Survey, National Research Program, Reston, VA, United States.

Author Contributions
[∇]Both authors contributed equally to this work.

Notes
The authors declare no competing financial interest.

ACKNOWLEDGMENTS

REFERENCES

(1) Ehrlich, H. *Earth-Sci. Rev.* **1998**, *45*, 45−60.
(2) (a) Richter, D. D., Jr.; Mobley, M. L. *Science* **2009**, *326*, 1067−1068. (b) Akob, D. M.; Kuesel, K. *Biogeosciences* **2011**, *8*, 3531−3543.
(3) (a) Trumbore, S. E.; Czimczik, C. I. *Science* **2008**, *321*, 1455−1456. (b) Schmidt, M. W.; Torn, M. S.; Abiven, S.; Dittmar, T.; Guggenberger, G.; Janssens, I. A.; Kleber, M.; Kogel-Knabner, I.; Lehmann, J.; Manning, D. A.; Nannipieri, P.; Rasse, D. P.; Weiner, S.; Trumbore, S. E. *Nature* **2011**, *478*, 49−56. (c) Davidson, E. A.; Trumbore, S. E.; Amundson, R. *Nature* **2000**, *408*, 789−790. (d) Mackenzie, F. T.; Lerman, A.; Andersson, A. J. *Biogeosciences* **2004**, *1*, 11−32. (e) Hammes, F.; Verstraete, W. *Rev. Environ. Sci. Biotechnol.* **2002**, *1*, 3−7. (f) Conrad, R. *Microbiol. Rev.* **1996**, *60*, 609−640. (g) Rusznyak, A.; Akob, D. M.; Nietzsche, S.; Eusterhues, K.; Totsche, K. U.; Neu, T. R.; Frosch, T.; Popp, J.; Keiner, R.; Geletneky, J.; Katzschmann, L.; Schulze, E.-D.; Kuesel, K. *Appl. Environ. Microbiol.* **2012**, *78*, 1157−1167. (h) Boquet, E.; Boronat, A.; Ramos-Cormenzana, A. *Nature* **1973**, *246*, 527−529. (i) Torn, M. S.; Trumbore, S. E.; Chadwick, O. A.; Vitousek, P. M.; Hendricks, D. M. *Nature* **1997**, *389*, 170−173. (j) Rautaray, D.; Ahmad, A.; Sastry, M. *J. Am. Chem. Soc.* **2003**, *125*, 14656−14657.
(4) Meldrum, F. C.; Colfen, H. *Chem. Rev.* **2008**, *108*, 4332−4432.
(5) (a) Lian, B.; Hu, Q. N.; Chen, J.; Ji, J. F.; Teng, H. H. *Geochim. Cosmochim. Acta* **2006**, *70*, 5522−5535. (b) Mitchell, A. C.; Ferris, F. G. *Geomicrobiol. J.* **2006**, *23*, 213−226.
(6) (a) Ryan, K. R.; Shapiro, L. *Annu. Rev. Biochem.* **2003**, *72*, 367. (b) Hirsch, P. *Adv. Space Res.* **1986**, *6*, 287−298.
(7) (a) Boylen, C. W. *J. Bacteriol.* **1973**, *113*, 33−37. (b) Tixier, C.; Sancelme, M.; Ait-Aissa, S.; Widehem, P.; Bonnemoy, F.; Cuer, A.; Truffaut, N.; Veschambre, H. *Chemosphere* **2002**, *46*, 519−526.
(8) (a) Cacchio, P.; Contento, R.; Ercole, C.; Cappuccio, G.; Martinez, M. P.; Lepidi, A. *Geomicrobiol. J.* **2004**, *21*, 497−509. (b) Groth, I.; Schumann, P.; Laiz, L.; Sanchez-Moral, S.; Canaveras, J. C.; Saiz-Jimenez, C. *Geomicrobiol. J.* **2001**, *18*, 241−258.
(9) Wright, D. T.; Oren, A. *Geomicrobiol. J.* **2005**, *22*, 27−53.
(10) Anthony, J. W.; Bideaux, R. A.; Bladh, K. W.; Nichols, M. C. *Handbook of Mineralogy*; Mineral Data Publishing: Tucson, AZ, 2005; Vol. 5.
(11) Domart-Coulon, I. J.; Elbert, D. C.; Scully, E. P.; Calimlim, P. S.; Ostrander, G. K. *Proc. Natl. Acad. Sci. U.S.A.* **2001**, *98*, 11885−11890.
(12) Warren, L. A.; Maurice, P. A.; Parmar, N.; Ferris, F. G. *Geomicrobiol. J.* **2001**, *18*, 93−115.
(13) Ramachandran, S. K.; Ramakrishnan, V.; Bang, S. S. *ACI Mater. J.* **2001**, *98*, 3−9.

38

(14) (a) Le Metayer-Levrel, G.; Castanier, S.; Orial, G.; Loubiere, J. F.; Perthuisot, J. P. *Sediment. Geol.* **1999**, *126*, 25−34. (b) Webster, G.; Sass, H.; Cragg, B. A.; Gorra, R.; Knab, N. J.; Green, C. J.; Mathes, F.; Fry, J. C.; Weightman, A. J.; Parkes, R. J. *FEMS Microbiol. Ecol.* **2011**, *77*, 248−263. (c) Rodriguez-Navarro, C.; Jroundi, F.; Schiro, M.; Ruiz-Agudo, E.; Gonzalez-Munoz, M. T. *Appl. Environ. Microbiol.* **2012**, *78*, 4017−4029.

(15) Stetter, J. R.; Li, J. *Chem. Rev.* **2008**, *108*, 352−366.

(16) Govind, R.; Gao, C.; Lai, L.; Tabak, H. H. *Water Environ. Res.* **1997**, *69*, 73−80.

(17) Koletzko, S.; Koletzko, B.; Haisch, M.; Hering, P.; Seeboth, I.; Hengels, K.; Braden, B.; Hering, P. *Lancet* **1995**, *345*, 961−962.

(18) (a) Zalicki, P.; Zare, R. N. *J. Chem. Phys.* **1995**, *102*, 2708. (b) Berden, G.; Peeters, R.; Meijer, G. *Int. Rev. Phys. Chem.* **2000**, *19*, 565−607.

(19) Koskinen, V.; Fonsen, J.; Kauppinen, J.; Kauppinen, I. *Vib. Spectrosc.* **2006**, *42*, 239−242.

(20) (a) Patterson, B. W.; Zhang, X. J.; Chen, Y.; Klein, S.; Wolfe, R. R. *Metabolism* **1997**, *46*, 943−948. (b) Kanu, A. B.; Dwivedi, P.; Tam, M.; Matz, L.; Hill, H. H., Jr. *J. Mass Spectrom.* **2008**, *43*, 1−22.

(21) (a) Frosch, T.; Meyer, T.; Schmitt, M.; Popp, J. *Anal. Chem.* **2007**, *79*, 6159−6166. (b) Frosch, T.; Schmitt, M.; Noll, T.; Bringmann, G.; Schenzel, K.; Popp, J. *Anal. Chem.* **2007**, *79*, 986−993. (c) Frosch, T.; Tarcea, N.; Schmitt, M.; Thiele, H.; Langenhorst, F.; Popp, J. *Anal. Chem.* **2007**, *79*, 1101−1108.

(22) (a) Frosch, T.; Popp, J. *J. Mol. Struct.* **2009**, *924−926*, 301−308. (b) Frosch, T.; Popp, J. *J. Biomed. Opt.* **2010**, *15*, 041516/1−041516/9. (c) Frosch, T.; Schmitt, M.; Bringmann, G.; Kiefer, W.; Popp, J. *J. Phys. Chem. B* **2007**, *111*, 1815−1822. (d) Frosch, T.; Schmitt, M.; Popp, J. *Anal. Bioanal. Chem.* **2007**, *387*, 1749−1757.

(23) (a) Frosch, T.; Koncarevic, S.; Becker, K.; Popp, J. *Analyst* **2009**, *134*, 1126−1132. (b) Frosch, T.; Koncarevic, S.; Zedler, L.; Schmitt, M.; Schenzel, K.; Becker, K.; Popp, J. *J. Phys. Chem. B* **2007**, *111*, 11047−11056. (c) Frosch, T.; Kuestner, B.; Schluecker, S.; Szeghalmi, A.; Schmitt, M.; Kiefer, W.; Popp, J. *J. Raman Spectrosc.* **2004**, *35*, 819−821. (d) Frosch, T.; Schmitt, M.; Popp, J. *J. Phys. Chem. B* **2007**, *111*, 4171−4177. (e) Frosch, T.; Schmitt, M.; Schenzel, K.; Faber, J. H.; Bringmann, G.; Kiefer, W.; Popp, J. *Biopolymers* **2006**, *82*, 295−300. (f) Frosch, T.; Yan, D.; Popp, J. *Anal. Chem.* **2013**, *85*, 6264−6271.

(24) (a) Frosch, T.; Keiner, R.; Michalzik, B.; Fischer, B.; Popp, J. *Anal. Chem.* **2013**, *85*, 1295−1299. (b) King, D. A.; Pittaro, R. J. *Opt. Lett.* **1998**, *23*, 774−776. (c) Salter, R.; Chu, J.; Hippler, M. *Analyst* **2012**, *137*, 4669−4676.

(25) Howardlock, H.; Stoicheff, B. *J. Mol. Spectrosc.* **1971**, *37*, 321−326.

(26) Dilly, O. *Soil Biol. Biochem.* **2001**, *33*, 117−127.

(27) (a) Kontoyannis, C. G.; Vagenas, N. V. *Analyst* **2000**, *125*, 251−255. (b) Gauldie, R. *Comp. Biochem. Physiol., Part A: Mol. Integr. Physiol.* **1997**, *118*, 753−757. (c) Wehrmeister, U.; Soldati, A. L.; Jacob, D. E.; Häger, T.; Hofmeister, W. *J. Raman Spectrosc.* **2010**, *41*, 193−201.

39

3.2 Enhanced Raman multigas sensing – a novel tool for control and analysis of $^{13}CO_2$-labeling experiments in environmental research [RK2]

Robert Keiner, Torsten Frosch, Tara Massad, Sue Trumbore, Jürgen Popp

Reprinted with kind permission of the *Royal Society Of Chemistry.*

Analyst

$^{13}CO_2$

$^{12}CO_2$

ROYAL SOCIETY
OF CHEMISTRY

PAPER
Torsten Frosch et al.
Enhanced Raman multigas sensing – a novel tool for control and analysis of $^{13}CO_2$ labeling experiments in environmental research

Enhanced Raman multigas sensing – a novel tool for control and analysis of $^{13}CO_2$ labeling experiments in environmental research

Robert Keiner,[ab] Torsten Frosch,*[ab] Tara Massad,[c] Susan Trumbore[c] and Jürgen Popp[abd]

Cavity-enhanced Raman multigas spectrometry is introduced as a versatile technique for monitoring of $^{13}CO_2$ isotope labeling experiments, while simultaneously quantifying the fluxes of O_2 and other relevant gases across a wide range of concentrations. The multigas analysis was performed in a closed cycle; no gas was consumed, and the gas composition was not altered by the measurement. Isotope labeling of plant metabolites *via* photosynthetic uptake of $^{13}CO_2$ enables the investigation of resource flows in plants and is now an important tool in ecophysiological studies. In this experiment the ^{13}C labeling of monoclonal cuttings of *Populus trichocarpa* was undertaken. The high time resolution of the online multigas analysis allowed precise control of the pulse labeling and was exploited to calculate the kinetics of photosynthetic $^{13}CO_2$ uptake and to extrapolate the exact value of the $^{13}CO_2$ peak concentration in the labeling chamber. Further, the leaf dark respiration of immature and mature leaves was analyzed. The quantification of the photosynthetic O_2 production rate as a byproduct of the $^{13}CO_2$ uptake correlated with the amount of available light and the leaf area of the plants in the labeling chamber. The ability to acquire CO_2 and O_2 respiration rates simultaneously also simplifies the determination of respiratory quotients (rate of O_2 uptake compared to CO_2 release) and thus indicates the type of combusted substrate. By combining quantification of respiration quotients with the tracing of ^{13}C in plants, cavity enhanced Raman spectroscopy adds a valuable new tool for studies of metabolism at the organismal to ecosystem scale.

Introduction

Isotope labeling with gaseous precursors is an important tool in ecophysiological studies as it allows for a detailed investigation of the flow of resources at the level of an individual organism up to an entire ecosystem. For example, by labeling with ^{13}C, the existence of different carbon allocation patterns between plant functional groups[1] and the fast transfer of recently assimilated carbon to soil microorganisms[2] have been demonstrated. ^{13}C labeling has also been used at a molecular level to understand plant investments in secondary metabolites that serve as antiherbivore defenses[3] as well as the biosynthetic pathways leading to defense-related compounds.[4] Chemical ecology studies have monitored photosynthetic uptake of $^{13}CO_2$ in real time in order to measure the incorporation of newly assimilated ^{13}C into primary *versus* secondary metabolites under simulated herbivore pressure[4,5] to address the growth-defense hypothesis.[6] Measuring gas exchange of both $^{13}CO_2$ and $^{12}CO_2$ is important for investigations of the

balance of the amount of incorporated ^{13}C *versus* the amount of respirationally released $^{13}CO_2$. ^{13}C labeling of plants *via* exposure to pulses of $^{13}CO_2$ is becoming a more commonly employed tool in studies of plant physiology and chemical ecology.[7]

Nowadays, in most plant respiration experiments, CO_2 production is measured as the sole parameter, either electrochemically or by non-dispersive infrared absorption spectroscopy.[8] However, O_2 consumption is also important for the determination of the respiratory quotient in order to draw conclusions about the type of combusted substrate and for quantification of the amount of label that got fixed by the plant. Most commonly used methods are not sufficiently sensitive in the measurement of O_2 in plant respiration over timescales of minutes. High sensitivity O_2 measurements are currently performed by taking gas samples for successive lab-based analyses using gas chromatography (GC) in combination with mass spectrometry (GCMS) in order to determine O_2/N_2 ratios. Unfortunately, these chromatographic techniques are slow, consumptive, and expensive, because the samples consist of complex mixtures of gases at various concentrations and several expensive test gases are needed for instrument calibration. To date, the miniaturization of test equipment for rapid online monitoring of multigas-samples (consisting of O_2, N_2, $^{13}CO_2$ and $^{12}CO_2$) has been limited.

[a] Institute of Photonic Technology, Jena, Germany. E-mail: torsten.frosch@uni-jena.de
[b] Friedrich-Schiller University, Institute for Physical Chemistry, Jena, Germany
[c] Max-Plack-Institute for Biogeochemistry, Jena, Germany
[d] Friedrich-Schiller University, Abbe School of Photonics, Jena, Germany

These limitations can be circumvented by Raman spectroscopy, which provides characteristic information about molecular vibrations[9] and thus chemical specificity. Raman spectroscopy emerged in recent years as an extremely powerful method[10] in various natural science disciplines[11] to investigate solid samples, liquids, and gases. Raman gas analysis is capable of quantifying almost all gases (except noble gases) simultaneously with just one measurement.[12] This work introduces the methodology of cavity enhanced Raman multigas spectroscopy for pulse labeling studies of plant physiology.

Experimental details

Monoclonal cuttings of *Populus trichocarpa* were obtained from the "Thüringer Landesanstalt für Landwirtschaft", Dornburg (Germany). *Populus trichocarpa* is a fast-growing species native to western North America. Cuttings were individually planted in 2 l pots with potting soil (Klasmann KKS Bio Topfsubstrat 27) mixed 1 : 1 with quartz sand and grown in the greenhouse with additional light (Son-T Agro 430 W HPS bulbs, primary light range 520–610 nm, Philips Lighting Company, New Jersey, USA) from 6:00–17:00. The pots were uniformly watered with an irrigation system that delivered water two to three times for 3 min between 12:00 and 13:00 each day, depending on the temperature. The plants were moved to a climate chamber and exposed to five days of gradual cooling followed by an artificial winter of 8 h 10 °C days and 4 °C nights to induce senescence and leaf fall. The plants were returned to the greenhouse and exposed to the previous light and water conditions. As leaves were flushing, plants were exposed to $^{13}CO_2$ in a 2 m^3 labeling chamber (see Fig. 2). The gas phase was homogenized with the help of fans. Twenty-three to 25 plants were labeled on two consecutive days (runs 1 and 2, see Table 1) for approximately 2 h from 12:00 to 14:00. $^{13}CO_2$ was introduced into the chamber *via* acidification of 2.67 g followed by 1.33 g 99% NaH$^{13}CO_3$ (Cambridge Isotope Laboratories, USA) with 16 ml or 8 ml diluted hydrochloric acid. The leaf area of every plant was measured at the time of labeling.

Results and discussion

Raman gas monitoring of multigas mixtures containing isotopic labeled gases

The Raman gas sensor consists of a miniaturized laser diode with $\lambda_{exc.} = 650$ nm and a cw output power of 50 mW. This diode is passively frequency locked and feedback-coupled to a high-

finesse cavity (PCB) enabling a power build-up to 100 W. Thus a strong signal enhancement is achieved with only low power consumption of the instrument. The PCB supports a Gaussian beam and consists of an input coupler mirror and an end mirror, both with extremely low scattering losses and transmission. For optimal beam enhancement and stable operation, the cavity components are aligned for spatial mode matching of the input beam and the Gaussian beam supported by the PBC while the facet of the laser diode helps in stabilizing mode matching by spatial filtering.[13] This arrangement of the PCB is extremely stable to mechanical vibrations and is connected to a high-throughput spectrometer with a room temperature operated charge coupled device (CCD) with 512 pixels and a spectral resolution of approx. 50 cm^{-1}. Additional sensors monitor the laser intensity, pressure and temperature for reliable gas quantification. With the help of this strong signal enhancement it was possible to monitor concentration fluctuations of about 50 to 100 ppm within measurement times of one second. The device was calibrated for the relevant gases, N_2, O_2, $^{12}CO_2$, and $^{13}CO_2$, by flushing the optical cavity with pure gases. Underground correction was accomplished by subtracting the spectrum of the Raman inactive noble gas argon. $^{13}CO_2$ was calibrated with a GCMS-validated 1% mixture of $^{13}CO_2$ with 99% argon (Raman inactive noble gas). The calibrated reference spectra are a prerequisite for the online quantification of sample gases during the isotope labeling experiment (Fig. 1). A straightforward calibration approach is feasible because the Raman intensity, I_{Stokes}, scales strictly linearly with the gas density in molecules per volume, nV^{-1}, laser power, I_0, and partial pressure, p over the whole dynamic range.

$$I_{Stokes} \sim \frac{n}{V} I_0 p \tag{1}$$

Next, a least square fit of the measured spectrum and the calibrated reference spectra provided the concentrations of the individual gases. Therefore an over-determined linear equation system was solved with the calibration gas, g, measured gas, a (mixture of gases), intensity, $I(\tilde{\nu})$, concentration, c, CCD pixel, n, and number, m, of extracted gases.

$$\begin{bmatrix} I(\tilde{\nu})_{g_11} & \cdots & I(\tilde{\nu})_{g_m1} \\ \vdots & \ddots & \vdots \\ I(\tilde{\nu})_{g_1n} & \cdots & I(\tilde{\nu})_{g_mn} \end{bmatrix} \begin{bmatrix} c_1 \\ \vdots \\ c_m \end{bmatrix} = \begin{bmatrix} I(\tilde{\nu})_{a1} \\ \vdots \\ I(\tilde{\nu})_{an} \end{bmatrix} \tag{2}$$

Another major advantage of Raman multigas sensing becomes obvious from eqn (2), namely that all gases which

Table 1 Comparison of the Raman gas monitoring of two labeling runs with different leaf areas and available photosynthetically active radiation (PAR) in the labeling chamber. The amount of developed oxygen, mean PAR, total leaf area and the exponential decay time t_e are given. The oxygen production rate is higher and the CO_2 uptake is faster with higher light intensity and larger leaf area in labeling run 2. t_e represents the decay time until the concentration decreased to 1/e of its initial value based on the exponential fit equation: $c = c_0 e^{-t_e^{-1}t}$

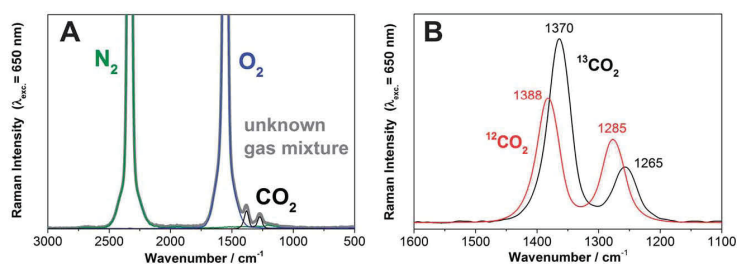| Labeling run	O_2 production [mol d^{-1}]	Light intensity PAR [W m^{-2}]	Total leaf area [m^2]	$^{13}CO_2$-uptake 1st dose t_e [min]	$^{13}CO_2$-uptake 2nd dose t_e [min]
1	0.35	121	2.29	23.52	20.6
2	0.38	275	3.11	17.16	15.7

43

Fig. 1 (A) Example of a Raman gas spectrum ($\lambda_{exc.}$ = 650 nm) during a typical leaf dark respiration measurement of *Populus trichocarpa*. The Raman spectrum of the unknown gas mixture (grey) and the Raman spectra of the individual gaseous components (green: N_2, blue O_2, black CO_2) are shown (N_2 and O_2 are ro–vibrational spectra, with unresolved O and S branches). The concentrations of the individual gases can be deconvoluted from the experimentally acquired envelope. (B) The Raman gas spectra of $^{12}CO_2$ and $^{13}CO_2$ can be distinguished and simultaneously quantified due to their spectral shift and differences in the intensity distribution of the Fermi diad.

appear in course of a labeling experiment will be detected in the Raman spectrum of the multigas-mixture. Thus, if the difference between the experimental multigas-spectrum and the deconvoluted individual spectra differs from a zero-baseline, more information about additional gases can be obtained by data post-processing with an increased number, m, of extracted gases. An example spectrum of an experimental gas mixture and the spectra of the gaseous components (N_2, O_2, and CO_2) are depicted in Fig. 1A. The Raman gas spectra of the chemically similar gaseous isotopes, $^{12}CO_2$ and $^{13}CO_2$, can be readily distinguished due to their spectral shift and differences in the intensity pattern of the Fermi diad[14] (Fig. 1B). Thus, all relevant gases (N_2, O_2, $^{12}CO_2$, and $^{13}CO_2$) can be quantified individually and simultaneously with no cross-sensitivity. The gas concentrations (N_2, O_2, $^{12}CO_2$, $^{13}CO_2$) obtained were normalized for a constant sum of all gases and a baseline subtraction was done for $^{12}CO_2$ and $^{13}CO_2$.

$^{13}CO_2$ labeling experiment of *Populus trichocarpa*

The utility of the new multigas sensing methodology is demonstrated in a labeling experiment that was designed to investigate the allocation of newly assimilated carbon to secondary metabolites. Saplings of *Populus trichocarpa* (see Experimental details) were exposed to $^{13}CO_2$ in the chamber during a two hour pulse labeling experiment (Fig. 2). The Raman gas sensor was connected to the labeling chamber on the opposite side of the $^{13}CO_2$ input to measure the labeled gas after it traveled through the chamber (Fig. 2). The Raman sensor always analyzed the homogenized gas concentration of the labeling chamber. Successive addition of the label was applied to increase the levels of ^{13}C that could be incorporated into plant metabolites. Raman gas monitoring was applied to observe the maximum $^{13}CO_2$ concentration and to ensure that the plants took up all the labeled ^{13}C. The continuous online quantification of the $^{13}CO_2$ level in the chamber allowed for accurate monitoring of the uptake during the labeling period and the precise timing of the second dose of $^{13}CO_2$ (Fig. 3).

First, the labeling chamber was flushed with CO_2-free air to decrease the amount of $^{12}CO_2$ from 586 ppm to <100 ppm within 0.5 h. At 0.7 h, $^{13}CO_2$ was chemically generated from ^{13}C-
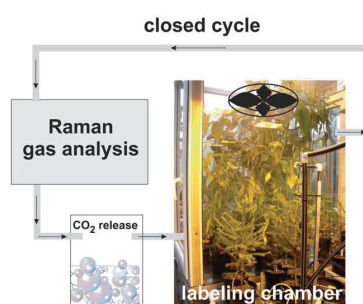

Fig. 2 Schematic setup of the Raman gas analysis of a $^{13}CO_2$ labeling experiment. The Raman gas sensor was connected to the labeling chamber such that the homogenized gas of the chamber was analyzed in a closed cycle. The Raman analysis did not change the gas composition. $^{13}CO_2$ was released chemically and introduced into the chamber by a valve. The inset-photograph of the labeling chamber shows the seedlings of *Populus trichocarpa* under growing lights in order to stimulate photosynthetic uptake of $^{13}CO_2$.
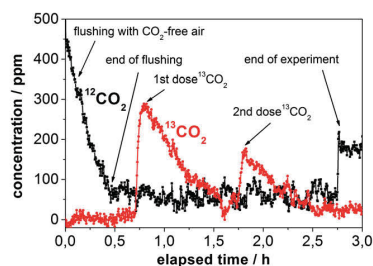

Fig. 3 Online Raman multigas analysis of the $^{13}CO_2$ pulse labeling experiment. The concentrations of $^{12}CO_2$ and $^{13}CO_2$ in the chamber are shown over the duration of the labeling procedure. The relevant steps are assigned: flushing with CO_2-free air, release of $^{13}CO_2$, photosynthetic uptake of $^{13}CO_2$ (1st dose and 2nd dose), and opening of the chamber at the end. $^{12}CO_2$, $^{13}CO_2$, and O_2 were simultaneously quantified without cross-sensitivity.

bicarbonate and diluted hydrochloric acid. A few minutes later the concentration of $^{13}CO_2$ reached its maximum at 298 ppm and then decreased to <100 ppm after 1.6 h due to

44

photosynthetic uptake by the plants (Fig. 3). After the complete uptake of the first dose, a second dose was administered. The $^{13}CO_2$ concentration reached 182 ppm at 1.8 h and dropped to <100 ppm during the next half hour. At 2.75 h the labeling chamber was opened to ambient air. The concentration of O_2 (calculated by a linear fit) rose by approximately 400 ppm during the labeling period, whereas the concentration of N_2 did not change significantly.

A major drawback of conventional gas sampling techniques is the extended time needed for data analysis and consequently the small number of data points. In contrast, the high time resolution of Raman gas sensing was exploited for the rapid acquisition of many data points tracking the $^{13}CO_2$-concentration during the course of the labeling, which allowed for kinetic investigations. First-order exponential fitting enabled the very precise determination of time constants (Table 1) and peak concentrations of $^{13}CO_2$ (Table 2).

Two separate labeling runs were performed on different days, and more leaf area and photosynthetically active radiation (PAR) were available inside the labeling chamber in the second run. The comparison of both runs revealed that the amount of O_2 produced during the $^{13}CO_2$ labeling period was higher (0.38 mol per day compared to 0.35 mol per day) in run two. Similarly, the uptake of $^{13}CO_2$ over time was faster in the second run, with a decay time of 15.7 min to reduce the amount of $^{13}CO_2$ to $1/e$ of its starting value in comparison to 20.6 min in the first labeling run. All values are summarized in Table 1.

The high time resolution of Raman gas monitoring (Fig. 3) enabled the detection of small deviations from the exponential decay due to fluctuations in natural light intensity, and, by comparison of both doses, it was even possible to confirm that $^{13}CO_2$ uptake by *P. trichocarpa* was faster at higher concentrations of $^{13}CO_2$ within the course of the first dose because the photosynthesis rate of C_3 plants is not strictly linear at low concentrations.[15]

An important task in environmental labeling experiments is the correct estimation of the peak concentration of $^{13}CO_2$ in the labeling chamber. Peak concentrations are conventionally calculated based on the mass of the ^{13}C-bicarbonate used to create the $^{13}CO_2$. However, these approximations overestimate the value in the homogenized chamber atmosphere, due to the immediate photosynthetic $^{13}CO_2$-uptake by the plants in the

labeling chamber and the time for the chemical release of $^{13}CO_2$ which broadens the sharpness of the labeling pulse. It is more precise to measure the $^{13}CO_2$-concentration in the labeling chamber online and with rapid data acquisition by means of Raman gas sensing and calculate the peak concentration from the decay equation with high precision by extrapolating back to the time of the dose (Table 2). These peak concentrations of $^{13}CO_2$ were lower with the first addition of $^{13}CO_2$ than those calculated based on the mass of reacted bicarbonate, but the extrapolated values were higher after the second addition of $^{13}CO_2$ in each labeling run (Table 2). This demonstrates that residual $^{13}CO_2$ from the first dose was still present at the addition of the second dose, meaning actual $^{13}CO_2$ values were noticeably higher than expected by standard bicarbonate-weight based calculations (Table 2).

In general, the amount of available data points from the temporally highly resolved Raman spectroscopic gas measurements enabled a very reliable fitting of time dependency curvatures and was well suited for kinetic investigations.

Leaf dark respiration

The labeled plants were further investigated with leaf dark respiration measurements in order to understand $^{13}CO_2$ exchange over time. Approximately 24 h after the ^{13}C-labeling, *P. trichocarpa* leaves of a known area were enclosed in a dark chamber, and the concentrations of O_2, $^{12}CO_2$, and $^{13}CO_2$ were continuously recorded. The fluxes of all gases were calculated based on changes of the gas concentrations over time in the enclosed headspace. The fluxes were related to a leaf area that was based on one side of the leaf only to represent the area where the stomata are located. The respired gases were circulated through the instrument and returned to the chamber without consumption or alteration by the measurement. Ambient air was measured after one hour to validate the stability of experimental setting. A linear fit of the gas concentrations over time yielded rates for the uptake of O_2 and CO_2 production (Fig. 4). The current detection limit of the device for

Table 2 Summary of the $^{13}CO_2$ peak concentrations (ppm) released. The calculated values were derived from the weighted ^{13}C-bicarbonate portion. The extrapolated values were derived from the exponential fit of the measured $^{13}CO_2$ Raman gas curve. Both calculations are in agreement, however the extrapolated Raman gas data deliver more precise information of the homogenized chamber gas atmosphere due to the fast photosynthetic $^{13}CO_2$-uptake during the time of the chemical $^{13}CO_2$-release

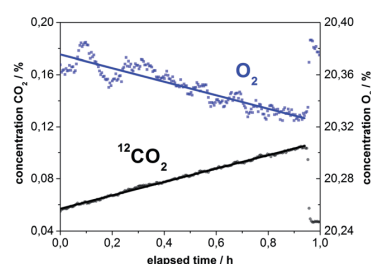| Labeling run	1st dose calculated [ppm]	1st dose extrapolated [ppm]	2nd dose calculated [ppm]	2nd dose extrapolated [ppm]
1	400	386	200	212
2	400	381	200	215

Fig. 4 Quantification of O_2 and CO_2 during the course of a leaf dark respiration measurement of *Populus trichocarpa*. The amount of O_2 decreased and the concentration of CO_2 increased linearly with respect to time. The slopes of the linear fits yield the respiration rates for both gases with just a single measurement. Ambient air was measured as a reference at the end of the experiment, and the concentrations of O_2 and CO_2 leap back to the correct starting values of air.

45

$^{12}CO_2$ was 48 ppm ($\sigma = 3$) which results in a limit of detectable exchange rate of 0.12 µmol m^{-2} h^{-1}. The additional $^{13}CO_2$ efflux rate added by the highly diluted label from the plant was below this level. The leaf dark respiration measurements resulted in an O_2 consumption rate of 1.81 µmol m^{-2} h^{-1} and a CO_2 production rate of 1.80 µmol m^{-2} h^{-1} for immature leaves. In comparison, mature leaves consumed only 0.70 µmol m^{-2} h^{-1} of O_2 and produced just 0.74 µmol m^{-2} h^{-1} of CO_2. These results indicate that the respiration rates of immature leaves are more than twice as high as the respiration rates of mature leaves. Distinctly higher dark respiration rates of immature leaves are also reported in the literature.[16] Simultaneous Raman spectroscopic quantification of O_2 and CO_2 also allowed for the calculation of the respiratory quotient (RQ) which yields information about the compounds being metabolized and respired. Deviations in the respiratory quotient arise from differing carbon–oxygen ratios of substrates or the formation of byproducts.[17] The RQ values were ~1 for all leaves, indicating the combustion of starch.[18]

Conclusions and outlook

This work demonstrates the unique capabilities of innovative cavity enhanced Raman gas monitoring for the control and analysis of $^{13}CO_2$-labeling experiments. Enhanced Raman gas sensing is superior to conventional Raman gas spectroscopy, due to the strong power build up to 100 W within the cavity (while maintaining low instrument power consumption) and outperforms other gas sensing techniques for the rapid and simultaneous analysis of multiple gases in a labeling chamber while eliminating sample collections and delayed analyses. The technique is non-consumptive, such that the measurements can be performed in a closed cycle with the labeling chamber without altering the gas composition. The high time resolution of the Raman measurement enables the acquisition of a huge number of data points, which tremendously increases the accuracy of kinetic investigations. Thus, it was possible to determine precise uptake rates and peak concentrations of $^{13}CO_2$ in the pulse labeling of *P. trichocarpa*. Additionally, the simultaneous measurements of CO_2 and O_2 allowed for calculation of photosynthetic rates for both gases at once which correlated with the leaf area as well as the photosynthetically active radiation inside the labeling chamber. The investigation of leaf dark respiration of *P. trichocarpa* revealed that the respiration rate of immature leaves was more than twice as high compared to mature leaves. Simultaneous Raman gas quantification of O_2 and CO_2 enabled the calculation of the respiratory quotient, which is an indicator of the chemistry of metabolites that are fueling respiration, or can indicate the net effects of gas transport *via* the plant transpiration stream. Monitoring of $^{13}CO_2$, $^{12}CO_2$, and O_2 also allows for quantification of the amount of label that got fixed by the plant and the $^{13}C : ^{12}C$-ratio.

Cavity enhanced Raman multigas sensing was shown to be a very versatile new technique for monitoring the amount of label incorporation in $^{13}CO_2$-labeling experiments and it is also capable of rapidly analyzing the respiration quotient, an ecophysiologically important parameter. This new technique is affordable and very robust due to the linearity of signal intensity to analyte concentration. We therefore anticipate that cavity enhanced Raman spectroscopy (CERS) will become an important tool for labeling experiments in environmental research.

Acknowledgements

References

1 M. S. Carbone and S. E. Trumbore, Contribution of new photosynthetic assimilates to respiration by perennial grasses and shrubs: residence times and allocation patterns, *New Phytol.*, 2007, **176**(1), 124–135.

2 P. Högberg, M. N. Högberg, S. G. Göttlicher, N. R. Betson, S. G. Keel, D. B. Metcalfe, C. Campbell, A. Schindlbacher, V. Hurry, T. Lundmark, S. Linder and T. Näsholm, High temporal resolution tracing of photosynthate carbon from the tree canopy to forest soil microorganisms, *New Phytol.*, 2008, **177**(1), 220–228.

3 T. Arnold and J. Schultz, Induced sink strength as a prerequisite for induced tannin biosynthesis in developing leaves of *Populus*, *Oecologia*, 2002, **130**(4), 585–593.

4 E. C. Connor, A. S. Rott, M. Zeder, F. Juttner and S. Dorn, 13C-labelling patterns of green leaf volatiles indicating different dynamics of precursors in *Brassica* leaves, *Phytochemistry*, 2008, **69**(6), 1304–1312.

5 D. Yakir and L. d. S. L. Sternberg, The use of stable isotopes to study ecosystem gas exchange, *Oecologia*, 2000, **123**(3), 297–311.

6 D. A. Herms and W. J. Mattson, The Dilemma of Plants: To Grow or Defend, *Q. Rev. Biol.*, 1992, **67**(3), 283.

7 D. Epron, M. Bahn, D. Derrien, F. A. Lattanzi, J. Pumpanen, A. Gessler, P. Hogberg, P. Maillard, M. Dannoura, D. Gerant and N. Buchmann, Pulse-labelling trees to study carbon allocation dynamics: a review of methods, current knowledge and future prospects, *Tree Physiol.*, 2012, **32**(6), 776–798.

8 (a) A. Saveyn, K. Steppe, M. A. McGuire, R. Lemeur and R. O. Teskey, Stem respiration and carbon dioxide efflux of young *Populus deltoides* trees in relation to temperature and xylem carbon dioxide concentration, *Oecologia*, 2008, **154**(4), 637–649; (b) S. Hunt, Measurements of photosynthesis and respiration in plants, *Physiol. Plant.*, 2003, **117**(3), 314–325.

9 (a) T. Frosch, S. Koncarevic, K. Becker and J. Popp, Morphology-sensitive Raman modes of the malaria pigment hemozoin, *Analyst*, 2009, **134**(6), 1126–1132; (b) T. Frosch and J. Popp, Structural analysis of the antimalarial drug halofantrine by means of Raman spectroscopy and density functional theory calculations, *J. Biomed. Opt.*, 2010, **15**(4),

46

041516; (*c*) T. Frosch, M. Schmitt, G. Bringmann, W. Kiefer and J. Popp, Structural analysis of the anti-malaria active agent chloroquine under physiological conditions, *J. Phys. Chem. B*, 2007, **111**(7), 1815–1822; (*d*) T. Frosch, M. Schmitt, K. Schenzel, J. H. Faber, G. Bringmann, W. Kiefer and J. Popp, *In vivo* localization and identification of the antiplasmodial alkaloid dioncophylline A in the tropical liana *Triphyophyllum peltatum* by a combination of fluorescence, near infrared Fourier transform Raman microscopy, and density functional theory calcula, *Biopolymers*, 2006, **82**(4), 295–300.

10 (*a*) T. Frosch, T. Meyer, M. Schmitt and J. Popp, Device for Raman difference spectroscopy, *Anal. Chem.*, 2007, **79**(16), 6159–6166; (*b*) T. Frosch, M. Schmitt, T. Noll, G. Bringmann, K. Schenzel and J. Popp, Ultrasensitive *in situ* tracing of the alkaloid dioncophylline A in the tropical liana *Triphyophyllum peltatum* by applying deep-UV resonance Raman microscopy, *Anal. Chem.*, 2007, **79**(3), 986–993; (*c*) T. Frosch, N. Tarcea, M. Schmitt, H. Thiele, F. Langenhorst and J. Popp, UV Raman Imaging - A Promising Tool for Astrobiology: Comparative Raman Studies with Different Excitation Wavelengths on SNC Martian Meteorites, *Anal. Chem.*, 2007, **79**(3), 1101–1108; (*d*) T. Frosch, D. Yan and J. Popp, Ultrasensitive Fiber Enhanced UV Resonance Raman Sensing of Drugs, *Anal. Chem.*, 2013, **85**(13), 6264–6271.

11 (*a*) T. Frosch, S. Koncarevic, L. Zedler, M. Schmitt, K. Schenzel, K. Becker and J. Popp, In situ localization and structural analysis of the malaria pigment hemozoin, *J. Phys. Chem. B*, 2007, **111**(37), 11047–11056; (*b*) T. Frosch, B. Küstner, S. Schlücker, a. Szeghalmi, M. Schmitt, W. Kiefer and J. Popp, In vitro polarization-resolved resonance Raman studies of the interaction of hematin with the antimalarial drug chloroquine, *J. Raman Spectrosc.*, 2004, **35**(10), 819–821; (*c*) T. Frosch and J. Popp, Relationship between molecular structure and Raman spectra of quinolines, *J. Mol. Struct.*, 2009, **924–926**, 301–

308; (*d*) T. Frosch, M. Schmitt and J. Popp, In situ UV resonance Raman micro-spectroscopic localization of the antimalarial quinine in cinchona bark, *J. Phys. Chem. B*, 2007, **111**(16), 4171–4177; (*e*) T. Frosch, M. Schmitt and J. Popp, Raman spectroscopic investigation of the antimalarial agent mefloquine, *Anal. Bioanal. Chem.*, 2007, **387**(5), 1749–1757.

12 (*a*) T. Frosch, R. Keiner, B. Michalzik, B. Fischer and J. Popp, Investigation of gas exchange processes in peat bog ecosystems by means of innovative Raman gas spectroscopy, *Anal. Chem.*, 2013, **85**(3), 1295–1299; (*b*) R. Keiner, T. Frosch, S. Hanf, A. Rusznyak, D. M. Akob, K. Kusel and J. Popp, Raman Spectroscopy-An Innovative and Versatile Tool To Follow the Respirational Activity and Carbonate Biomineralization of Important Cave Bacteria, *Anal. Chem.*, 2013; (*c*) R. Salter, J. Chu and M. Hippler, Cavity-enhanced Raman spectroscopy with optical feedback cw diode lasers for gas phase analysis and spectroscopy, *Analyst*, 2012, **137**(20), 4669–4676.

13 D. A. King and R. J. Pittaro, Simple diode pumping of a power-build up cavity, *Opt. Lett.*, 1998, **23**(10), 774–776.

14 H. Howardlock and B. Stoicheff, Raman intensity measurements of the Fermi diad ν_1, $2\nu_2$ in $^{12}CO_2$ and $^{13}CO_2$, *J. Mol. Spectrosc.*, 1971, **37**(2), 321–326.

15 T. D. Sharkey, Photosynthesis in intact leaves of C3 plants: Physics, physiology and rate limitations, *Bot. Rev.*, 1985, **51**(1), 53–105.

16 D. I. Dickmann, Photosynthesis and Respiration by Developing Leaves of Cottonwood (*Populus deltoides* Bartr.), *Bot. Gaz.*, 1971, **132**(4), 253–259.

17 J. Azcon-Bieto, H. Lambers and D. A. Day, Effect of Photosynthesis and Carbohydrate Status on Respiratory Rates and the Involvement of the Alternative Pathway in Leaf Respiration, *Plant Physiol.*, 1983, **72**(3), 598–603.

18 N. G. McDowell, Mechanisms linking drought, hydraulics, carbon metabolism, and vegetation mortality, *Plant Physiol.*, 2011, **155**(3), 1051–1059.

47

3.3 Investigation of Gas Exchange Processes in Peat Bog Ecosystems by Means of Innovative Raman Gas Spectroscopy [RK3]

Torsten Frosch, Robert Keiner, Beate Michalzik, Bernhard Fischer, Jürgen Popp

Investigation of Gas Exchange Processes in Peat Bog Ecosystems by Means of Innovative Raman Gas Spectroscopy

Torsten Frosch,[*,†,‡] Robert Keiner,[†,‡] Beate Michalzik,[§] Bernhard Fischer,[∥,⊗] and Jürgen Popp[†,‡,⊥]

[†]Institute of Photonic Technology, Jena, Germany

[‡]Friedrich-Schiller University, Institute for Physical Chemistry, Jena, Germany

[§]Friedrich-Schiller University, Institute of Geography, Jena, Germany

[∥]Philips Medical Systems, Boeblingen, Germany

[⊥]Friedrich-Schiller University, Abbe School of Photonics, Jena, Germany

ABSTRACT: Highly sensitive Raman gas spectroscopy is introduced for simultaneous real time analysis of O_2, CO_2, CH_4, and N_2 in order to elucidate the dynamics of greenhouse gases evolving from climate-sensitive ecosystems. The concentrations and fluxes of this suite of biogenic gases were quantified in the head space of a water-saturated, raised peat bog ecotron. The intact peat bog, exhibiting various degradation stages of peat and sphagnum moss, was exposed to various light regimes in order to determine important ecosystem parameters such as the maximum photosynthesis rate of the sphagnum as well as the extent of soil and plant respiration. Miniaturized Raman gas spectroscopy was proven to be an extremely versatile analytical technique that allows for onsite multigas analysis in high temporal resolution. Therefore it is an urgently needed tool for elucidation of complex biochemical processes especially in climate-sensitive ecosystems and consequently for the estimation of climate-relevant gas budgets.
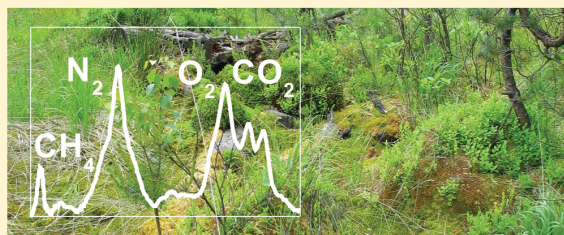
The characterization of biogenic gases in the atmosphere is extremely important for elucidation of environmental processes and the complex and interdependent interactions with the biosphere.[1] Many of these processes are not well understood but will have dramatic consequences for life on earth in the future.[2] As an example, the rapid rise of temperature in response to human activities might result in accelerated thawing of permafrost soil.[3] Therefore huge northern permafrost areas may transform into defrosted, reaerated peatlands and cause additional release of greenhouse gases. Peatlands are defined as ecosystems exhibiting a partially decomposed layer of peat forming a thickness of more than 30 cm.[3c] Though peatland areas of the northern hemisphere encompassing the boreal and subarctic climate zones only cover 3% of the global land surface,[4] they account for approximately one-third of the worlds soil carbon (455 Pg C)[3c] and therefore exhibit a high carbon density.

Peatlands sequester carbon into organic matter (OM) by the production of plant biomass, which is conserved by anoxic conditions and low temperatures resulting in low decomposition rates.[5] Since the last glaciation, the rate of plant production exceeds OM decomposition, leading to a net rate of C accumulation of 76 Tg C a^{-1}.[3c] Consequently, undisturbed peatlands maintain an imbalance between net primary production and decomposition leading to the accumulation of soil organic carbon and play an important role as carbon sinks in global biogeochemical cycles. However, in natural water-saturated bogs CH_4 is also produced,[6] and peatlands act as net sources of CH_4 with an annual release of 46 Tg CH_4–C, being equivalent to about 12% of the worlds total CH_4 emission.[3a] The global warming potential of CH_4 is 25 times higher than that of CO_2[7] making this gas ecologically relevant in lower concentrations as well. Today many bogs are drained for agricultural use, leading to an aeration of the upper peat soil and an enhanced soil respiration yielding CO_2. Thus, because of climate change, land-use change, and agricultural mismanagement, peatlands turn into net sources for greenhouse gases such as CO_2 and CH_4. In such peatland ecosystems, the complex dynamics of greenhouse gas fluxes are controlled by multiple, contrarily interacting processes: On one hand, soil respiration emits CO_2 acting as a C-source, whereas green plants assimilate CO_2 by photosynthesis during daylight (C-sink), turning into CO_2-sources after nightfall (dark respiration). Therefore, the monitoring of multigas exchange of the whole ecosystem is of central interest with respect to the budgets of climate relevant gases.[1a,b,3a,6b]

Unfortunately, there is a lack of miniaturized, field-portable, and robust sensors capable for simultaneous quantification of multicomponents in biogenic gas mixtures (e.g., CO_2 together with N_2, O_2, and CH_4) onsite and in real-time, without cross sensitivity and saturation effects.[8] The instruments currently

1295

available, include techniques like galvanic cells and non-dispersive infrared (NDIR) absorption sensors for CO_2, paramagnetic, electrochemical (Nernst-cell), semiconductive, and photoluminescence sensors for O_2 as well as utilization of the ionization potential of N_2.[9] CH_4 is usually quantified by taking samples for lab-based analysis by gas chromatography coupled with flame-ionization detection.[10] In order to increase the number of detectable gases, several electrochemical sensors can be combined,[11] but the characteristics and limitations of every single sensor have to be taken into account. All these approaches, however, suffer from low specificity, aging, drift, and saturation artifacts.[11,12] Also direct optical absorption methods (such as in Fourier transform-infrared spectroscopy (FT-IR),[13] cavity-ringdown spectroscopy (CRDS),[14] and photoacoustic spectroscopy[15]) cannot be applied for sensing homonuclear diatomic gases (such as H_2, N_2, and O_2) that do not exhibit a permanent dipole-moment. Because of the lack of versatile, portable multigas sensors, time-consuming gas sampling in the field is required followed by laboratory-based analysis. Lab-based instruments like gas chromatographs are bulky and expensive, although such instruments are highly sensitive.[16] Most involve separation steps with successive identification using flame and photoionization detectors (FID, PID)[17] or mass spectrometry (MS).

An innovative approach is Raman gas spectroscopy, a technique that is based on molecular vibrations[18] and capable for the quantification of a whole variety of biogenic gases simultaneously in a broad concentration range (from ppm to pure compounds) with practically no cross-sensitivity. Raman spectroscopy is nonconsumptive, label-free, and without drawbacks of other gas sensing techniques, such as saturation, bleeding, or strong cross-sensitivities.[12] Raman gas sensing is therefore perfectly suited for onsite quantification of CH_4 together with N_2, O_2, and CO_2 and provides sum parameters that describe soil respiration, photosynthesis, and methanogenesis with just one single measurement.

■ EXPERIMENTAL SECTION

Highly Sensitive Raman Gas Spectroscopy. Conventional Raman spectroscopy is a weak process and needs innovative enhancement techniques[19] in order to achieve high sensitivity. Raman gas sensors are nowadays based on specific multipass cavities, high pressure cells, or the application of high-power lasers.[20] While the application of high-power lasers consumes too much energy (mostly required for cooling), we exploit an innovative cavity enhancement of the electromagnetic field.[21] In doing so, a miniaturized laser diode, emitting 50 mW at 650 nm is passively frequency-locked and frequency-coupled to a high finesse optical cavity, enabling a power build up to 100 W and overall signal enhancement of 6 orders of magnitude. The beam from the laser diode enters the cavity through the input coupler mirror and is reflected back from the end mirror. Both mirrors have extremely low scattering losses and transmission. This high finesse cavity acts as a power build-up cavity (PBC)[21] supporting a Gaussian beam. In order to achieve optimal beam enhancement, it is necessary to align the cavity components for spatial mode matching of the input beam and the Gaussian beam supported by the PBC. The laser diode facet acts as a spatial filter which helps in stabilizing mode matching.[21] This configuration is very stable to mechanical vibrations. Additionally to strong enhancement of the exciting light, very efficient light collection optics is of prime importance. The whole device is very robust, highly

miniaturized (weight of approximately 500 g and size of 10 × 10 × 15 cm^3) and portable as well as with low power consumption and therefore perfectly suited for onsite application.

Raman scattering intensity offers excellent linearity with analyte concentration and allows for robust instrument calibration over a dynamic range of 4 orders of magnitude from approximately 100 ppm to pure compounds (which was tested with the presented instrument with help of various certified gas mixtures). For quantification of gas components in an unknown mixture, the laser intensity is monitored as well as the absolute pressure and temperature of the gas. Background signals of the setup are removed by subtracting a spectrum of argon (Raman inactive noble gas). The concentrations of the gas components in the acquired multigas mixture are least-squares fitted with measured calibration spectra of the individual gases, and the whole Raman spectra are taken into account. The difference spectrum is a good reference for the quality of the least-squares-fit and also elucidates remaining components in the multigas mixture. Therefore, one can also identify and account for gas components that were not expected, by adding the calibration spectra of these gases to the fitting algorithm. Obviously, this versatility, to account also for unexpected gases without prior knowledge, is a remarkable advantage, making Raman gas spectroscopy superior to other gas sensing techniques which have to be designed for a specific and known gas or gas mixture.

Peat Bog Column Experiment. The area where the peat column was collected (see Figure 1A) is located approximately
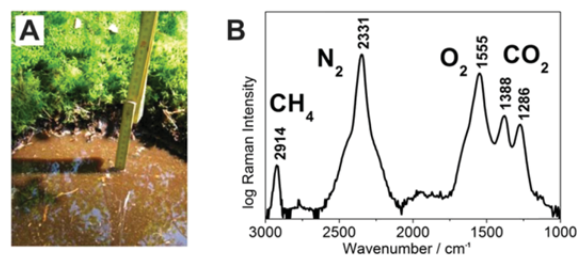

Figure 1. (A) Photograph of the location 20 km southeast of Jena (Germany) where the peat column was collected. The area is embedded in a hilly landscape at an altitude between 320 and 360 m a.s.l., exhibiting mean annual precipitations between 600 and 665 mm and mean annual temperatures of 7.0 to 7.7 °C. (B) Raman spectrum of peat bog gases showing methane, nitrogen, oxygen, and carbon dioxide. A logarithmic intensity scale was chosen for a better illustration.

20 km southeast of Jena (N 50°45'57.58" and E 11°41'51.1") and is embedded in a hilly landscape at an altitude between 320 to 360 m a.s.l., exhibiting mean annual precipitations between 600 and 665 mm and mean annual temperatures of 7.0 to 7.7 °C (TLWJF, 1997). An intact peat bog sample was cut out by a transparent acrylic plastic cylinder and transferred to an ecotron facility. The gas volume of the ecotron encompassed 1.6 L and a surface area of 230 cm^2. The peat ecotron was incubated at room temperature and controlled light conditions. The sample headspace was monitored for 4 h and the gases were cycled through the Raman gas device without consumption or altering of the gas composition. The obtained concentrations were normalized for a constant sum of gases. Gas rates were determined using the slope of a linear fit of the gas

concentrations over time. Both the soil gas rates and the leaf respiration rate were calculated using the chamber surface area. The pressure was 998 hPa, and the temperature complied with room temperature (25 °C).

■ RESULTS AND DISCUSSION

In order to study the different light-dependent biochemical processes that occur simultaneously and interdependent from each other in a complex ecosystem, the unique capabilities of the novel Raman sensor for onsite multigas quantification were exploited. The peat bog ecosystem, encompassing dead organic matter in the form of different typical peat degradation stages underneath a layer of alive sphagnum moss in a water-saturated environment (see Figure 1A), was exposed to various light regimes (phases I—V in Figure 2). The effects of different light
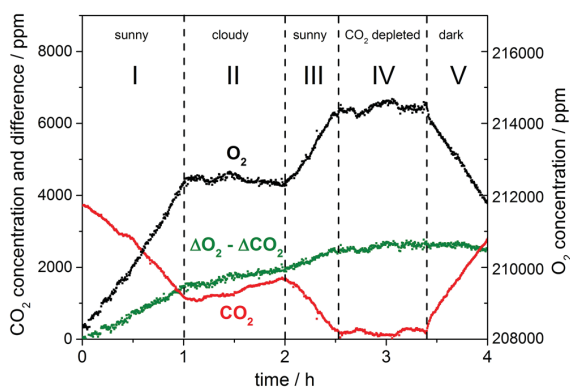

Figure 2. Raman gas monitoring of a raised bog sample (peat and sphagnum) for about 4 h. Oxygen and carbon dioxide concentrations as well as the difference of concentration changes ($\Delta O_2 - \Delta CO_2$) over time are shown. The measurement was performed in the headspace of the bog column. The peat bog was exposed to different experimental light regimes that are marked as phases I—V. The photosynthetic activity of the sphagnum and the respiratory activity can be observed dependent on the photosynthetic active radiation (PAR). The differences curve $\Delta O_2 - \Delta CO_2$ (green line) reveals the combination of processes that are not equimolar in sum, while the additional diffusion rate of CO_2 from the porous soil into the headspace lowers over time due to the peculiarities of a closed chamber experiment.[22a] The quantitative analysis of soil respiration, leaf respiration, and maximum photosynthesis rate of the sphagnum moss is presented in Table 1.

regimes on photosynthesis rates, the leaf- and soil respiration can be separated from each other and quantified with the help of Raman gas spectroscopy which enables the online monitoring of O_2, CO_2, CH_4, and N_2 (Figure 1B). The time course of the gas concentrations of O_2 and CO_2 emitted from the peat bog column are shown in Figure 2. Also the differences of the changes of O_2 and CO_2 ($\Delta O_2 - \Delta CO_2$) are highlighted as a green line in Figure 2 and reveal the combination of processes that are not equimolar in sum, which are explained by additional diffusion of CO_2 from the pore space of the peat body to the headspace gas atmosphere.

In the first hour of the experiment (phase I in Figure 2) the ecotron was placed in a sunny location and photosynthesis was promoted due to strong solar radiation, thus reducing the CO_2-concentration in the column headspace by 2600 ppm accompanied by simultaneous increase of the O_2-level by 4100 ppm. When the sun light intensity was reduced in phase II (by the presence of a cloud), the photosynthetic activity responded rapidly and respiration now contributed stronger to a decreasing headspace O_2 concentration by 150 ppm and a simultaneous increase of CO_2 by 560 ppm. A second strong photosynthesis activity started in phase III after cloud clearing until the CO_2-compensation point was reached. In this period O_2 increased by 2050 ppm and CO_2 decreased by 1480 ppm (phase III). In the next 30 min, subsequent to the CO_2 compensation point, CO_2 remained constant at ~150 ppm, but O_2 rose by 190 ppm (phase IV). In the following 35 min, the chamber was brought into a dark environment, leading to diminished O_2 and raised CO_2 concentrations (phase V). The concentrations of O_2 and CO_2 during the different phases I—V are summarized in Table 1.

In order to compare and quantify the individual biochemical processes over the course of the experiment, gas exchange rates were calculated and evaluated (see Table 1). The oxygen rates of the two photosynthesis periods (I and III) agreed well with each other: 3.22 and 3.37 μmol m^{-2} s^{-1}, respectively (Table 1). This similarity of both oxygen rates represents the photosynthesis saturation of the sphagnum (which is a C3 shade plant), which is already reached at relatively low amounts of solar radiation. However, the CO_2 slopes differed (-2.04 and -2.48 μmol m^{-2} s^{-1}). Lower amounts of CO_2 were released from the peat in phase III due to the peculiarities of a closed chamber experiment.[22] The differences in oxygen and carbon dioxide slopes are explained by slow diffusion rates of CO_2 from the porous peat body to the headspace. In the beginning, the gas atmosphere is in equilibrium with the open porosity of the upper peat layer. During the first photosynthesis period (phase

Table 1. Absolute Volume Concentrations and Gas Exchange Rates of O_2, CO_2, as well as the Difference $\Delta O_2 - \Delta CO_2$ of a Raised Bog Sample (Peat and Sphagnum) during Experimental Phases Varying in Photosynthetic Active Radiation (See Phases I—V in Figure 2)

phase		I	II	III	IV	V
O_2 ppm	begin	208 300	212 500	212 300	214 300	214 500
	end	212 500	212 300	214 300	214 500	211 800
CO_2 ppm	begin	3 730	1 120	1 670	160	180
	end	1 120	1 670	160	180	2 800
$\Delta O_2 - \Delta CO_2$ ppm	begin	0	1 480	1 930	2 450	2 620
	end	1 480	1 930	2 450	2 620	2 490
slope O_2 μmol m^{-2} s^{-1}		3.22	-0.13	3.37	0.16	-3.20
slope CO_2 μmol m^{-2} s^{-1}		-2.04	0.53	-2.48	0.04	3.03
slope $\Delta O_2 - \Delta CO_2$ μmol m^{-2} s^{-1}		1.18	0.41	0.89	0.20	-0.17

I) 3.22 μmol m^{-2} s^{-1} oxygen are produced. The CO_2 gas concentration in the headspace is reduced and further CO_2 is diffusing out of the peat, which leads to virtually lower total CO_2 consumption rates of 2.04 μmol m^{-2} s^{-1}. As explained above, these differences of oxygen and carbon dioxide changes represent processes that are not equimolar in sum (see green line in Figure 2).

In phases I–IV, CO_2 is diffusing out of the soil and is converted into O_2 by photosynthesis of the sphagnum. First, the concentration gradient of CO_2 in the peat pores and the headspace is high but diminishes with time. This results in decreasing diffusion rates over the course of the experiment, which is shown by positive but decreasing slopes of the difference curve in Table 1 (phase I in comparison with phase III and phase II with phase IV, respectively). In the last phase (V) CO_2 is produced by dark respiration. This results in an inversion of the gradient (-0.17 μmol m^{-2} s^{-1}) and CO_2 diffuses into the soil, leading to virtually lower respiration rates.[22b]

In phase IV, the CO_2 compensation point was reached due to photosynthetic activity and only a very small amount (0.04 μmol m^{-2} s^{-1}) of CO_2 enriched in the gas phase. The only remaining source of CO_2 is soil respiration, while gas phase and pore space got in equilibrium again, visible in the linearity of the difference graph (green line in Figure 2). In this phase IV, the photosynthesis was exclusively limited by the amount of available CO_2 released from the peat, which is immediately converted into oxygen (0.16 μmol m^{-2} s^{-1}). The slope of the difference graph represents the extent of soil respiration, which equals 0.20 μmol m^{-2} s^{-1}.

In phase V, the total dark respiration or net ecosystem exchange is represented by the oxygen fluxes in the absence of light. It equals 3.2 μmol m^{-2} s^{-1} and is again slightly higher than the CO_2-flux and in good agreement with the literature.[23] Phases IV and V together allow for the separation of soil respiration (phase IV) and total respiration of soil and plants (phase V). The difference of both represents plant respiration (3.04 μmol m^{-2} s^{-1}) which is referenced to the ecotron area and in good agreement with the literature,[24] considering that the sphagnum leaf area is larger.

As explained in the introduction, peatlands emit the greenhouse gas CH_4 which was simultaneously quantified by Raman gas spectroscopy in the headspace of the peat bog column (Figure 1B). An amount of 420 ppm CH_4 was developed throughout the experiment, leading to a flux of 0.11 μmol m^2 s^{-1} which is in agreement with the literature.[10]

The simultaneous quantification of O_2 and CO_2 by means of Raman gas sensing clearly illustrates the difficulties that appear when CO_2 alone is used as the sole parameter for ecosystem characterization.

CONCLUSION

Raman gas spectroscopy is an extremely versatile analytical technique capable for simultaneous quantification of a whole orchestra of biogenic gases. An innovative design of a power-build-up cavity is exploited for very strong signal enhancement and at the same time enables onsite gas analysis due to instrument miniaturization, low power consumption and robustness. This novel analytical device was applied for quantification of O_2 and CO_2 together with CH_4 and N_2, in the head space of a water-saturated, raised peat bog ecotron, simultaneously over time within just one single measurement. This intact peat bog including sphagnum moss was exposed to various light regimes in order to study the different biochemical processes that occur simultaneously and interdependent from each other in a complex ecosystem. Raman spectroscopic multigas sensing enabled the determination of important ecosystem parameters such as the maximum photosynthesis rate of the sphagnum as well as the extent of soil respiration and plant respiration. The Raman spectroscopic monitoring of dynamics of greenhouse gas fluxes is very important for elucidation of complex biochemical processes in peatlands and for balancing of climate relevant gases.

AUTHOR INFORMATION

Corresponding Author

*Address: Institute of Photonic Technology, Albert-Einstein-Strasse 9, D-07745 Jena, Germany. E-mail: torsten.frosch@uni-jena.de.

Notes

The authors declare no competing financial interest.
⊗Former affiliate.

REFERENCES

(1) (a) Conrad, R. *Microbiol. Rev.* **1996**, 60 (4), 609−640. (b) Andreae, M. O.; Schimel, D. S.; Robertson, G. P. *Exchange of Trace Gases between Terrestrial Ecosystems and the Atmosphere*; John Wiley and Sons: Chichester, U.K., 1989; p 347. (c) Harden, J. W.; O'Neill, K. P.; Trumbore, S. E.; Veldhuis, H.; Stocks, B. J. *J. Geophys. Res.* **1997**, 102 (D24), 28805−28816.

(2) (a) Trumbore, S. E.; Chadwick, O. A.; Amundson, R. *Science* **1996**, 272 (5260), 393−396. (b) Wang, Y.; Amundson, R.; Trumbore, S. *Global Biogeochem. Cycles* **1999**, 13 (1), 47.

(3) (a) Wuebbles, D.; Hayhoe, K. *Earth-Sci. Rev.* **2002**, 57 (3−4), 177−210. (b) Davidson, E. A.; Janssens, I. A. *Nature* **2006**, 440 (7081), 165−173. (c) Gorham, E. *Ecol. Appl.* **1991**, 1 (2), 182.

(4) Rydin, H.; Jeglum, J. *The Biology of Peatlands*; Oxford University Press: New York, 2006.

(5) Moore, T.; Basiliko, N. *Decomposition Boreal Peatlands* **2006**, 188, 125−143.

(6) (a) Conrad, R. *FEMS Microbiol. Ecol.* **1999**, 28 (3), 193−202. (b) Thomas, K. L.; Benstead, J.; Davies, K. L.; Lloyd, D. *Soil Biol. Biochem.* **1996**, 28 (1), 17−23.

(7) Forster, P.; Ramaswamy, V.; Artaxo, P.; Berntsen, T.; Betts, R.; Fahey, D. W.; Haywood, J.; Lean, J.; Lowe, D. C.; Myhre, G.; Nganga, J.; Prinn, R.; Raga, G.; Schulz, M.; van Dorland, R.; et al. Changes in Atmospheric Constituents and in Radiative Forcing. In *Climate Change 2007: The Physical Science Basis. Contribution of Working Group I to the Fourth Assessment Report of the Intergovernmental Panel on Climate Change*; Solomon, S., Qin, D., Manning, M., Chen, Z., Marquis, M., Averyt, K. B., Tignor, M., Miller, H. L., Eds.; Cambridge University Press: Cambridge, U.K. and New York, 2007.

(8) (a) Rakow, N. a.; Suslick, K. S. *Nature* **2000**, 406 (6797), 710−713. (b) Gardner, J. W.; Bartlett, P. N. *Sens. Actuators, B* **1994**, 18 (1−3), 210−211. (c) Kanan, S. M.; El-Kadri, O. M.; Abu-Yousef, I. A.; Kanan, M. C. *Sensors (Basel)* **2009**, 9 (10), 8158−96. (d) Yamazoe, N.; Miura, N. *Sens. Actuators, B* **1994**, 20 (2−3), 95−102. (e) Seiyama, T.; Nakahara, T.; Takeuchi, T., *Overview of Gas Sensors for Environmental Use*; Elsevier: Amsterdam, The Netherlands, 1994; Vol. 59, p 233−272. (f) Ohira, S.-I.; Toda, K. *Anal. Chim. Acta* **2008**, 619 (2), 143−156.

(9) Modi, A.; Koratkar, N.; Lass, E.; Wei, B.; Ajayan, P. M. *Nature* **2003**, 424 (6945), 171−174.

(10) Deppe, M.; Knorr, K. H.; McKnight, D. M.; Blodau, C. *Biogeochemistry* **2010**, *100* (1), 89–103.

(11) Röck, F.; Barsan, N.; Weimar, U. *Chem. Rev.* **2008**, *108* (2), 705–725.

(12) Wolfbeis, O. S. *Anal. Chem.* **2008**, *80* (12), 4269–4283.

(13) (a) Esler, M. B.; Griffith, D. W. T.; Wilson, S. R.; Steele, L. P. *Anal. Chem.* **2000**, *72* (1), 206–215. (b) Griffith, D. W. T.; Leuning, R.; Denmead, O. T.; Jamie, I. M. *Atmos. Environ.* **2002**, *36* (11), 1833–1842.

(14) Berden, G.; Peeters, R.; Meijer, G. *Int. Rev. Phys. Chem.* **2000**, *19* (4), 565–607.

(15) Koskinen, V.; Fonsen, J.; Kauppinen, J.; Kauppinen, I. *Vib. Spectrosc.* **2006**, *42* (2), 239–242.

(16) (a) Patterson, B. W.; Zhang, X. J.; Chen, Y.; Klein, S.; Wolfe, R. R. *Metab., Clin. Exp.* **1997**, *46* (8), 943–948. (b) Kanu, A. B.; Dwivedi, P.; Tam, M.; Matz, L.; Hill, H. H., Jr. *J. Mass Spectrom.* **2008**, *43* (1), 1–22.

(17) Reiche, M.; Gleixner, G.; Küsel, K. *Biogeosciences* **2010**, *7* (1), 187–198.

(18) (a) Frosch, T.; Koncarevic, S.; Becker, K.; Popp, J. *Analyst* **2009**, *134* (6), 1126–1132. (b) Frosch, T.; Popp, J. *J. Biomed. Opt.* **2011**, *15* (4), 041516–041516. (c) Frosch, T.; Schmitt, M.; Popp, J. *J. Phys. Chem. B* **2007**, *111* (16), 4171–4177. (d) Frosch, T.; Schmitt, M.; Bringmann, G.; Kiefer, W.; Popp, J. *J. Phys. Chem. B* **2007**, *111* (7), 1815–1822. (e) Frosch, T.; Kustner, B.; Schlucker, S.; Szeghalmi, A.; Schmitt, M.; Kiefer, W.; Popp, J. *J. Raman Spectrosc.* **2004**, *35* (10), 819–821. (f) Frosch, T.; Schmitt, M.; Schenzel, K.; Faber, J. H.; Bringmann, G.; Kiefer, W.; Popp, J. *Biopolymers* **2006**, *82* (4), 295–300. (g) Frosch, T.; Koncarevic, S.; Zedler, L.; Schmitt, M.; Schenzel, K.; Becker, K.; Popp, J. *J. Phys. Chem. B* **2007**, *111* (37), 11047–11056.

(19) (a) Frosch, T.; Meyer, T.; Schmitt, M.; Popp, J. *Anal. Chem.* **2007**, *79* (16), 6159–6166. (b) Frosch, T.; Schmitt, M.; Noll, T.; Bringmann, G.; Schenzel, K.; Popp, J. *Anal. Chem.* **2007**, *79* (3), 986–993. (c) Frosch, T.; Tarcea, N.; Schmitt, M.; Thiele, H.; Langenhorst, F.; Popp, J. *Anal. Chem.* **2007**, *79* (3), 1101–1108.

(20) (a) Li, X.; Xia, Y.; Zhan, L.; Huang, J. *Opt. Lett.* **2008**, *33* (18), 2143–2145. (b) Li, X. Y.; Xia, Y. X.; Huang, J. M.; Zhan, L. *Appl. Phys. B: Laser Opt.* **2008**, *93* (2–3), 665–669. (c) Kiefer, J.; Seeger, T.; Steuer, S.; Schorsch, S.; Weikl, M. C.; Leipertz, A. *Meas. Sci. Technol.* **2008**, *19* (8), 085408–085408. (d) Schiel, D.; Richter, W. *Fresenius' Z. Anal. Chem.* **1987**, *327* (3–4), 335–337.

(21) King, D. a.; Pittaro, R. J. *Opt. Lett.* **1998**, *23* (10), 774–776.

(22) (a) Livingston, G. P.; Hutchinson, G. L.; Spartalian, K. *Soil Sci. Soc. Am. J.* **2006**, *70* (5), 1459. (b) Venterea, R. T. *J. Environ. Qual.* **2010**, *39* (1), 126–135.

(23) Dinsmore, K. J.; Skiba, U. M.; Billett, M. F.; Rees, R. M. *Plant Soil* **2008**, *318* (1–2), 229–242.

(24) Niemi, R.; Martikainen, P. J.; Silvola, J.; Holopainen, T. *Science Total Environ.* **2002**, *289* (1–3), 1–12.

53

3.4 Fiber-enhanced Raman multi-gas spectroscopy – a versatile tool for environmental gas sensing and breath analysis [RK4]

Stefan Hanf, Robert Keiner, Di Yan, Jürgen Popp, Torsten Frosch

Fiber-Enhanced Raman Multigas Spectroscopy: A Versatile Tool for Environmental Gas Sensing and Breath Analysis

Stefan Hanf,[†] Robert Keiner,[†] Di Yan,[†] Jürgen Popp,[†,‡,§] and Torsten Frosch*[,†,‡]

[†]Leibniz Institute of Photonic Technology, Jena, Germany

[‡]Institute for Physical Chemistry, Friedrich-Schiller University, Jena, Germany

[§]Abbe School of Photonics, Friedrich-Schiller University, Jena, Germany

S *Supporting Information*

ABSTRACT: Versatile multigas analysis bears high potential for environmental sensing of climate relevant gases and noninvasive early stage diagnosis of disease states in human breath. In this contribution, a fiber-enhanced Raman spectroscopic (FERS) analysis of a suite of climate relevant atmospheric gases is presented, which allowed for reliable quantification of CH_4, CO_2, and N_2O alongside N_2 and O_2 with just one single measurement. A highly improved analytical sensitivity was achieved, down to a sub-parts per million limit of detection with a high dynamic range of 6 orders of magnitude and within a second measurement time. The high potential of FERS for the detection of disease markers was demonstrated with the analysis of 27 nL of exhaled human breath. The natural isotopes $^{13}CO_2$ and $^{14}N^{15}N$ were quantified at low levels, simultaneously with the major breath components N_2, O_2, and $^{12}CO_2$. The natural abundances of $^{13}CO_2$ and $^{14}N^{15}N$ were experimentally quantified in very good agreement to theoretical values. A fiber adapter assembly and gas filling setup was designed for rapid and automated analysis of multigas compositions and their fluctuations within seconds and without the need for optical readjustment of the sensor arrangement. On the basis of the abilities of such miniaturized FERS system, we expect high potential for the diagnosis of clinically administered ^{13}C-labeled CO_2 in human breath and also foresee high impact for disease detection via biologically vital nitrogen compounds.
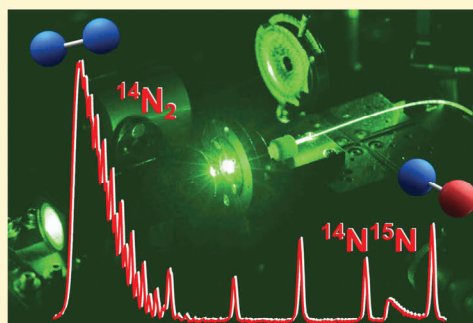
H uman breath analysis bears great potential for noninvasive early stage monitoring of disease states.[1] Breath analysis is highly accepted by patients and enables rapid diagnosis and continuous bedside observation of intensive care patients. Human breath is a mixture of different major compounds like N_2, O_2, CO_2, and H_2O and traces of volatile organic compounds (VOC). The simultaneous quantification of a whole suite of gaseous components in combination with chemometric analysis yields high diagnostic potential.[2] One of the major challenges is the accurate quantification of many gases in different concentration ranges simultaneously. Important gaseous markers for the detection of lung cancer are acetone (C_3H_6O) and methane (CH_4), along with H_2, CO, CO_2, and NH_3.[3] Other important diseases and their marker gases include (mitochondrial) oxidative stress (CO),[4] colonic fermentation (CH_4, H_2),[5] and *Helicobacter pylori* infection (NH_3, $^{12}CO_2$)[6] with diagnosis by means of isotopic-labeled $^{13}CO_2$.[7]

In the field of environmental gas sensing, it is important to trace climate relevant atmospheric gases (e.g., CH_4, CO_2, N_2O, N_2, and O_2), which are also strongly influenced by microbial activities in soil.[8] Temperate forest soils, for example, have been identified as significant sinks for CH_4 and as sources for NO, CO_2, and N_2O,[9] while wetlands are a major source of CH_4.[10] Methane is an important greenhouse gas, whose global warming potential is 25 times higher than that of CO_2.[11] The excessive production of N_2O, another potent greenhouse gas, contributes to catalytic stratospheric ozone destruction.[11] The annual increase of atmospheric N_2O is also a consequence of microbial denitrification by heterotrophic bacteria (e.g., *Pseudomonas*) as well as autotrophic denitrifiers.[12] The monitoring of multigas exchanges is thus of significant importance for an understanding of the dynamic interactions between soil, microbes, and plants in climate-sensitive ecosystems.[13]

Due to the low concentrations and diversity of the complex composition of atmospheric gases and the gas markers in breath samples, the gas analysis demands highly selective and sensitive methods. The most commonly used technique for selective quantification of simple gases is mass spectrometry, which is often coupled to gas chromatography for the separation of larger molecules.[14] Although mass spectrometry is an accurate and sensitive technique, capable of fast and simultaneous monitoring of some simple gases,[15] this technique is bulky, expensive, difficult to calibrate, and limited for miniaturization. Methods based on infrared (IR) absorption spectroscopy, such

5278

as cavity ring-down spectroscopy (CRDS)[16] and photoacoustic spectroscopy,[17] provide high sensitivity for the analysis of molecules with strong dipole moment (e.g., the atmospheric gases CO_2, CH_4, and N_2O) but cannot be applied for the detection of important homonuclear diatomic gases (e.g., H_2, O_2, and N_2).[18]

Raman spectroscopy,[19] a technique based on molecular vibrations,[20] is well-suited for selective multigas detection and considered as a potential technique for human breath analysis[21] and environmental gas sensing.[22] An advantage of using Raman spectroscopy for gas sensing is the ability for simultaneous identification of all gases (except noble gases) and volatiles, in a wide range of concentrations, within a complex mixture of gases.[22] Raman gas analysis is very fast, nonconsumptive, requires no labeling or sample preparation, and also enables the detection of homonuclear diatomic gases (N_2, O_2, and H_2). The simultaneous quantification of isotopic-labeled gases[23] (e.g., $^{13}CO_2$, $^{15}N_2$) provides a capability for tracer experiments. All gases can be quantified with help of their specific Raman bands and also a priori unexpected gases can easily be identified in the Raman spectra of complex multigas-compositions, in contrast to simple gas sensors that must be calibrated for all expected gases.[18] Thus, Raman multigas sensing is a powerful technique but is not yet established in medical breath diagnosis due to the low sensitivity of the Raman scattering process.

A promising approach for the enhancement of the intrinsically weak Raman signals is the improvement of the interaction of the laser light with the analyte molecules within hollow-core optical waveguides.[24] Gas sensors based on simple capillaries or hollow metal waveguides are already known[25] but suffer from high attenuation. Hollow-core photonic crystal fibers (HC-PCF)[26] can guide the light with low attenuation within a spectral bandgap and have recently emerged as a promising tool which could be exploited for sensitive gas analysis.[27] The light within a photonic crystal fiber is guided at a low-index defect within a quasi-2D photonic crystal lattice, forming the fiber cladding. The guided wavevectors are surrounded by propagation modes with a higher and lower propagation constant β. For higher vacuum wavevectors k than β, bandgaps appear which trap the light within the inner hollow core. This leads to broad spectral transmission windows for the laser light and the Raman-scattered photons. The HC-PCF confines both, the optical field and the gaseous analyte, within a micrometer-sized central hollow core of an elaborate microstructure. Only small sample volumes (~nanoliters per centimeter fiber length) are needed, and long optical interaction lengths are achieved for highly efficient interaction of light and gas molecules and thus provide enhanced analytical sensitivity.

METHODS AND MATERIAL

HC-PCF Based Setup for Raman Gas Sensing. The scattering cross section of the Raman effect is very low (around 10^{-23} cm^2/sr).[28] This drawback can be circumvented with an advanced experimental setup. Several parameters can be exploited to increase the amount of Raman scattered light and therefore improve the limit of detection (LOD). The Raman scattering intensity can be expressed by the simplified equation[29,30]

$$I_R(\tilde{\nu}_R, \tilde{\nu}_0) = \eta I_0 n \left(\frac{d\sigma(\tilde{\nu}_R, \tilde{\nu}_0)}{d\Omega} \right) \Omega L_e \qquad (1)$$

In this equation, I_0 represents the intensity of exciting laser, I_R the intensity of the Raman scattered light, n the molecule density of the measured gas (parts per cm^{-3}), and $(d\sigma)/(d\Omega)$ the absolute differential Raman scattering cross section (in centimeters squared per steradian). The factor η represents the detection efficiency of the experimental setup [accounting, for example, for the signal collection and optical fiber coupling efficiency, the quality of the optical components (mirrors, filters, gratings efficiencies, etc.), and the quantum efficiency of the detector]. Ω (in steradian) is the solid angle of the signal collection optic. The effective length L_e with $L_e = (1 - e^{-(\alpha_L - \alpha_R)L})/(\alpha_L + \alpha_R)$ describes the improved interaction lengths in fiber sensing with backscattering geometry, where α_L and α_R (in inverse meters) represent the attenuation of the excitation laser light and the Raman signal at a specific wavelength. A linear relationship appears between the Raman scattered signal and the laser intensity as well as the particle density of the gas (eq 1). The particle density (n) is proportional to the pressure and temperature according to the ideal gas law.

A Raman fiber-setup with detection in the visible range combines several advantages: availability of compact, high power lasers with excellent beam quality, detectors with high quantum efficiency and low noise, and high-quality gratings, mirrors, filters, and objectives.

The optical design of the HC-PCF-based Raman gas-sensing setup is schematically shown in Figure 1A. A frequency-doubled
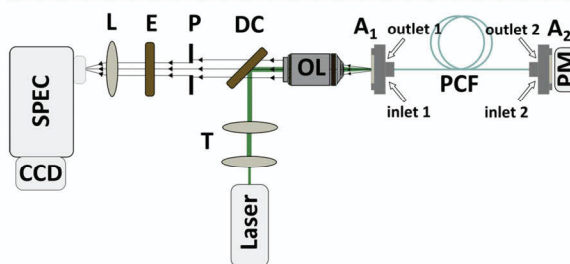

Figure 1. Design of the optical setup for fiber-enhanced Raman spectroscopy (FERS) consisting of laser, telescope (T), long-pass dichroic beam splitter (DC), objective lens (OL), fiber adapter assembly (A1 and A2), hollow-core photonic crystal fiber (PCF), powermeter (PM), pinhole (P), edge filter (E), aspheric lens (L), spectrometer (SPEC), and CCD detector.

Nd:YAG laser (with λ_L = 532.2 nm, I_L = 3.2 W, and M^2 < 1.1) from Laser Quantum is applied. The beam passes a telescope (T) to increase the beam diameter and matches the NA of the fiber. The laser light is reflected into a plan fluorite objective lens (OL) 20×/0.5 (Olympus) via a dichroic beam splitter (DC) with edge at 532 nm, providing a reflectivity of 98% for s-polarized laser light. The focused beam is coupled into a 1 m HC-PCF (HC580-02) with a central transmission wavelength of 580 nm via a three-axis nanopositioning stage (A). The core diameter of the applied HC-PCF is about 7 μm and most of the laser power is focused well within the center of the fiber core. The fiber provides an optical bandgap with a minimal attenuation at 580 nm and a spectral range from 532−633 nm, such that the excitation wavelength λ = 532 nm lies at the low wavelength edge of the bandgap and a spectral region of more than 3000 cm^{-1} can be guided with extremely low attenuation (Figure S1 of the Supporting Information), which also includes the vibrational stretching mode of CH_4 at 2917
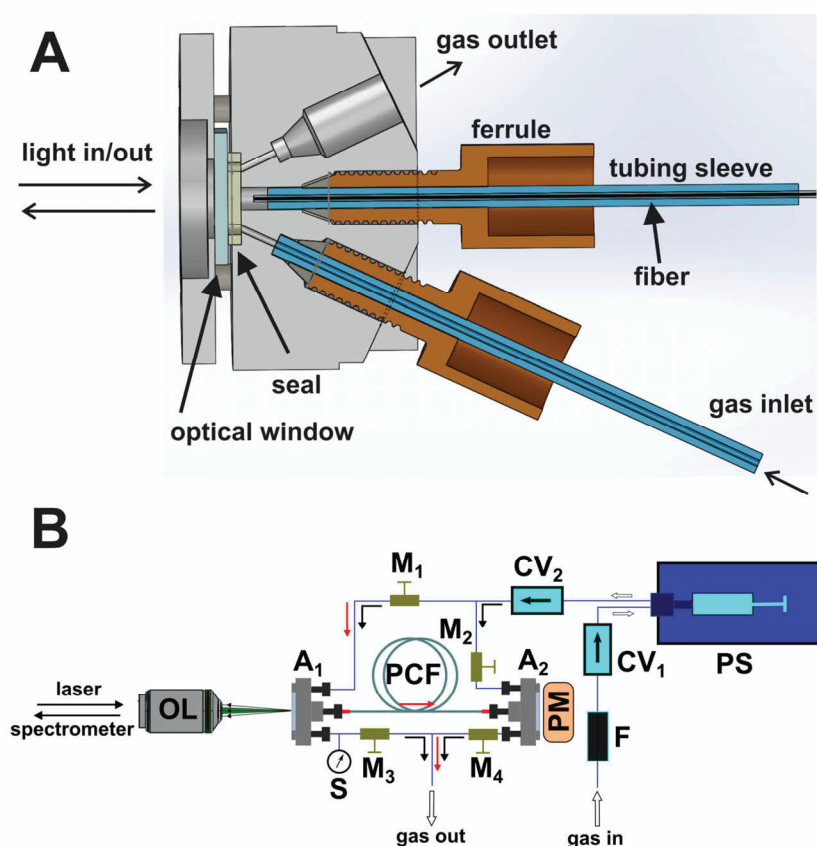
Figure 2. (A) Schematic illustration of the fiber adapter assembly for the alignment-free optical coupling and gas filling of the HC-PCF. The assembly consist of ferrules and tubing sleeves for the mounting of the HC-PCF (middle) and HPLC tubing for gas inlet and outlet (bottom and top). The laser is coupled through an optical window into the HC-PCF, and the Raman signal is collected in backscattering geometry. (B) Sketch of the setup for fast and precise filling of the HC-PCF with gas mixtures consisting of midpressure pump system (PS), fiber adapter assemblies (A_1 and A_2, see Figure 2A), check valves (CV), magnetic valves (M), powermeter (PM), hollow-core photonic crystal fiber (PCF), objective lens 20×/0.5 (OL), sensor for pressure and temperature (S), and sinter filter (F).

cm^{-1}. The transmission spectrum of the fiber is insensitive to bending, which is important for quantification, setup stability, and miniaturization.

The backscattered red-shifted Raman signal passes the dichroic mirror (DC) and edge filter (E) where the Rayleigh signal is suppressed. This backscattered light is then focused by a 75 mm achromatic lens (L) on the slit of the spectrometer (Acton 2556 with LN_2-cooled back-illuminated CCD detector). The whole collection setup magnifies the 7 μm core-diameter at the fiber exit to an approximately 60 μm diameter spot size with NA of 0.05 on the slit plane of the spectrometer in order to match the collection NA and achieve optimal etendue. The inelastically scattered photons are detected via a liquid nitrogen cooled CCD. Three gratings in the spectrometer allow overview measurements (grating with 600 lines/millimeter, which provides a resolution of 0.10 nm/pixel; equal to 3.5 cm^{-1}/pixel at 557.03 nm) and high resolved measurements [gratings with 1800 (2400) lines/mm, with resolutions of 0.03 (0.024) nm/pixel; equal to 1.0 (0.78) cm^{-1}/pixel at 557.03 nm respectively] An additional spatial filter, consisting of a pinhole (P), is inserted between the dichroic beam splitter (DC) and edge filter (E) to suppress the Raman signal from the silica of the fiber cladding such that the Raman signal of the gas samples is not attenuated and has optimal signal-to-noise ratio (SNR).

■ RESULTS AND DISCUSSION

Reproducible Optical Coupling of the Sensor-Fiber for Reliable, Quantitative FERS Gas Analysis. High stability of the optical coupling is essential for reliable gas quantification and was achieved by specially designed fiber adapter assemblies (Figures 1 and 2). The adapters (A1 and A2) at each end of the fiber solve several crucial tasks at once: laser coupling and collection of the Raman-scattered light through an optical window, collection of the transmitted light for permanent monitoring with a power meter (PM), and fast and reproducible flushing of the fiber with gas analytes. Each adapter consists of a fitting for the fiber, while entrance and exit ports enable gas flow and flushing (Figure 2A). The adapter was designed for low working distances between the microscope objective and fiber end facet down to 3 mm to increase the possible choice of high-NA microscope objectives. The sealing and optical window enables a pressure tight volume for fiber pressures up to 20 bar. The minimized dead volume within each adapter assembly is less than 100 nL. The two-way gas flow for each adapter enables fast flushing of the dead
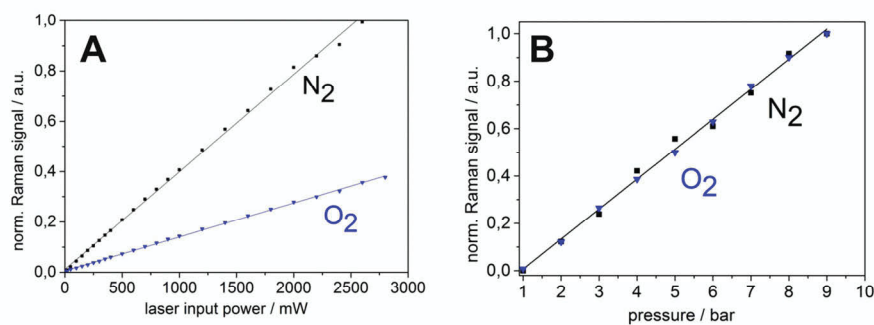
57

Figure 3. (A) Demonstration of the excellent linearity and scalability of the fiber-enhanced Raman signals of gaseous nitrogen and oxygen with rising laser powers (peak areas at 2331 and 1555 cm^{-1} were fitted and integrated, respectively). (B) Linearly increasing peak areas of the nitrogen and oxygen Raman signals are shown for linearly rising (absolute) gas pressure.

volume and fiber fillings within seconds for moderate gas pressures. The fast gas filling of the fiber-sensor is essential for fast FERS monitoring of changing gas concentrations and was achieved with a syringe pump system (PS), which is capable of increasing the pressure up to 20 bar in the fiber (Figure 2B). The gas mixture passes first a sinter filter (F) with a pore size of 0.5 μm, is then filled in the syringe, and afterward the dead volume of the setup gets flushed with gas (while all magnetic valves M_1–M_4 are opened and the gas flow follows the direction of the black arrows in Figure 2B). Second, the magnetic valves M_2 and M_3 are closed, and the analyte gas passes exclusively through the hollow fiber (red arrows in Figure 2B). All magnetic valves (M_1–M_4) are closed prior to quantitative FERS measurements to ensure constant pressure within the fiber. The whole measurement procedure is fully automated by a LabView (National Instruments) routine, which reads and controls magnetic valves, pump system, power meter, and spectrometer. In doing so, it is possible to perform a rapid measurement, including fast gas filling, Raman analysis, new gas filling, etc. and thus to follow the concentration changes of a complex multigas mixture within seconds and without the need for optical readjustment of the backscattering arrangement.

For online quantification of the concentrations of the individual gases in a gas mixture, the Raman spectra of gases were taken for known concentration, pressure, temperature, exposure time, laser power, transmitted power, and fiber length and were saved as calibration files in the Labview routine. This calibration is very robust due to the linearity between gas concentration and laser intensity and Raman intensity (eq 1). Thus, higher sensitivities can be achieved for the analysis of minor gas compounds by controlled adjustment of the laser power and gas pressure. An excellent linearity between laser intensity and pressure as well as Raman intensity of N_2 and O_2 was shown with laser powers up to 2.8 W (Figure 3A) and pressures up to 9 bar (Figure 3B), which provides a substantial increase in sensitivity by 2 orders of magnitude compared to conventional parameters.

Fiber-Enhanced Raman Analysis of Environmentally Relevant Multigas Compositions. The simultaneous quantification of the climate relevant gases CH_4, CO_2, N_2O, N_2, and O_2 as well as their fluctuations is of high interest for ecosystem characterization as explained in the introduction. Thus, a mixture of these five important biogenic gases was analyzed in order to demonstrate the analytical abilities of the new FERS-setup. The high specificity and reliability of the

method is demonstrated in the Raman spectrum of a defined mixture of CH_4, CO_2, N_2O, N_2, and O_2 (Figure 4) with
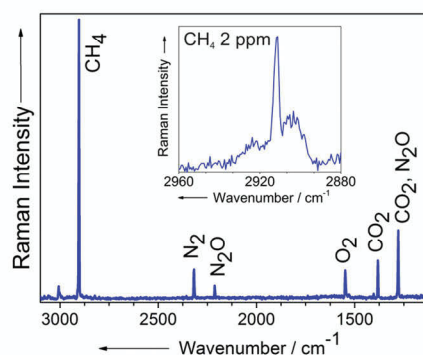

Figure 4. Fiber-enhanced Raman spectrum of a biogenic multigas composition, consisting of climate relevant gases CO_2, CH_4, and N_2O together with N_2, O_2 (each ~1 vol %, in Raman inactive argon carrier gas), which was acquired with one single measurement within a 40 ms acquisition time. All gases are spectrally well-separated from each other and can easily be quantified simultaneously. The inset shows a separate measurement, the fiber-enhanced Raman spectrum of naturally concentrated CH_4 at 2 ppm in air with SNR = 28 and thus sub-ppm LOD.

precisely defined concentrations (Table 1). All five gases show Raman peaks within the spectral bandgap of about 3100 cm^{-1}, provided by the HC-PCF (Figure S1 of the Supporting Information), and can easily be separated from each other. A calibration of the setup was performed by measurements of the individual pure gas components with known concentration, at

Table 1. Comparison of the Quantitative FERS Multi-Gas Measurement and the Certified Values of the Multi-Component Reference Gas from Linde AG (Prepared in Compliance with DIN EN ISO 6141)

gas component	certified concentrations (%)	measured Raman concentrations (%)	deviation absolute (%)
N_2	1.12	1.15	0.03
O_2	0.915	1.01	0.095
CO_2	1.02	1.10	0.08
N_2O	0.985	0.870	0.115
CH_4	1.08	1.00	−0.08

58

constant pressure, temperature, fiber length, and laser power (as explained before).

The experimentally obtained concentrations of the five biogenic gases were in very good agreement with the specified concentrations of the certified reference gas composition. The deviations of the Raman quantification of the gases N_2, O_2, CO_2, and CH_4 from the certified values were below 0.1%. The deviation of N_2O was slightly higher (0.115%) due to the small relative scattering cross section of the symmetric valence vibration between the N atoms in N_2O of around 0.51[31] (the N_2O Raman peak at 2224 cm^{-1} was preferred for the measurements because it did not superimpose with Raman peaks from other components). All data are summarized in Table 1.

The absolute sensitivity of the FERS analysis of all five biogenic gases (at pressure 20 bar and laser power 2 W) is shown in Table 2. The sensitivities for the individual gases scale

Table 2. Overview of Raman shifts, Relative Raman Scattering Cross Sections Normalized to the Cross Section of Nitrogen, and Achieved Limits of Detection for the Multiple Biogenic Gases

component	Raman shift (cm^{-1})	relative Raman scattering cross section at 532 nm[31]	LOD (ppm)
N_2	2331	1.0	9
O_2	1555	1.0	8
CO_2	1388	1.1	4
N_2O	2224	0.5	19
CH_4	2917	8.6	0.2

with their absolute scattering cross section, which is particularly high for the four times degenerated vibration of methane. In order to demonstrate the high sensitivity of the new setup, CH_4 was analyzed at atmospheric concentration of 2 ppm, with SNR of 28 and, accordingly, an LOD of 0.22 ppm (inset in Figure 4 and Table 2).

The achieved low LOD values prove that fiber-enhanced Raman gas spectrometry is an extremely capable technique for simultaneous quantification of the climate relevant gases CH_4, CO_2, and N_2O alongside with the major biogenic gases N_2 and O_2.

Fiber-Enhanced Raman Analysis of Human Breath. In order to demonstrate the potential of fiber-enhanced Raman spectroscopy for simultaneous detection of disease markers in breath gas analysis, the Raman spectrum of 27 nL exhaled human breath was analyzed within the hollow fiber (Figure 5). The typical concentrations of endogenous breath molecules are given in Table 3. The Raman peaks of the major breath components $^{14}N_2$, $^{16}O_2$, and $^{12}CO_2$ can be found at 2331, 1555, 1388, and 1285 cm^{-1}, respectively. Minor gases that appear in the lower ppm range are highly interesting for clinical diagnosis of metabolic diseases and thus it is very promising that the natural isotopes $^{14}N^{15}N$ (inset Figure 5) and $^{13}CO_2$ could also be quantified in the Raman spectrum of the breath sample.

The experimentally derived concentrations of the different gas component of the human breath sample were in very good agreement with literature values[31] (Table 3). It should be emphasized that minor components at low concentrations (e.g., 400 ppm of the natural stable isotopic $^{13}CO_2$) were quantified simultaneously with major components (e.g., 77.8% for N_2) with just one single measurement. The result highlights the high dynamic range of about 4 orders of magnitude in this
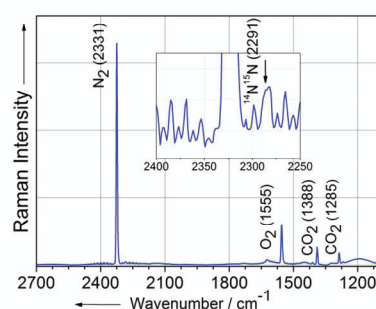

Figure 5. Fiber-enhanced Raman spectrum of 27 nL of exhaled human breath, which shows N_2, O_2, and CO_2 as the permanent gases in breath. The inset zooms the $^{14}N^{15}N$ natural isotope peak out, which superimposes with the O-branch of $^{14}N_2$.

Table 3. FERS Quantification of $^{14}N_2$, $^{16}O_2$, $^{12}CO_2$, $^{13}CO_2$, and $^{14}N^{15}N$ within Human Breath and Comparison with Literature Values.[31][a]

component	theoretical concentration in %	measured concentration in %	relative scattering cross section
$^{14}N_2$	78	77.8	1.00
$^{16}O_2$	16−17	16.0	1.02
$^{12}CO_2$	3−4	4.4	1.1 (1388)
$^{13}CO_2$	0.033−0.044	0.04	1.13 (1370)
$^{14}N^{15}N$	0.58	0.60	1.00

[a]The cross sections of the vibrational Raman transitions of different molecular components in human breath are given.

fiber-enhanced Raman gas analysis. These results are very promising because ^{13}C-labeled markers are successfully applied in breath analysis for the detection of different metabolic disorders, whereas the ^{15}N-tracer technique is not yet commonly applied in breath gas diagnosis. Besides the ability for the quantification of the low concentrated stable isotopes $^{14}N^{15}N$ and $^{13}CO_2$, the hollow fiber also provides a miniaturized sample container for the analysis of very small breath sample volumes of some tens of nanoliters.

Highly Resolved FERS of Isotopic-Labeled Gases. In order to demonstrate the unique capabilities of FERS for selective and quantitative isotope gas analysis in a high dynamic range, a high-resolution FERS analysis on natural CO_2 and N_2 was performed, including all their natural isotopes (Figure 6).

The diagnosis of clinically administered ^{13}C-labeled CO_2 in human breath requires the selective identification of the label on a huge background of naturally exhaled CO_2, including its natural isotopes. Obviously it is an essential prerequisite, for medical gas diagnosis of administered ^{13}C-label in breath, to perform a thorough analysis of the content of natural CO_2 isotopes and to develop a reliable technique for their quantification. Thus, a fiber-enhanced Raman spectrum of CO_2 was acquired (Figure 6A), which shows the typical Fermi dyad[32] of the major natural isotope $^{12}C^{16}O_2$. The sharp Q-branches of the $\tilde{\nu}_1$ and $2\tilde{\nu}_2$ bands of $^{12}C^{16}O_2$ result from the coupling of the fundamental symmetric stretching mode $\tilde{\nu}_1$ at 1286 cm^{-1} and the first overtone of the bending mode $2\tilde{\nu}_2$ at 1388 cm^{-1}. The dyad is often simply assigned with $\tilde{\nu}_-$ and $\tilde{\nu}_+$ for the lower and higher wavenumber, respectively. The measured hot bands for $^{12}C^{16}O_2$ occur at wavenumbers 1410 cm^{-1} ($\tilde{\nu}_+^{(1)}$) and 1265 cm^{-1} ($\tilde{\nu}_-^{(1)}$), shifted relative to the fundamental bands[32] (Figure 6A). The Fermi dyad of the
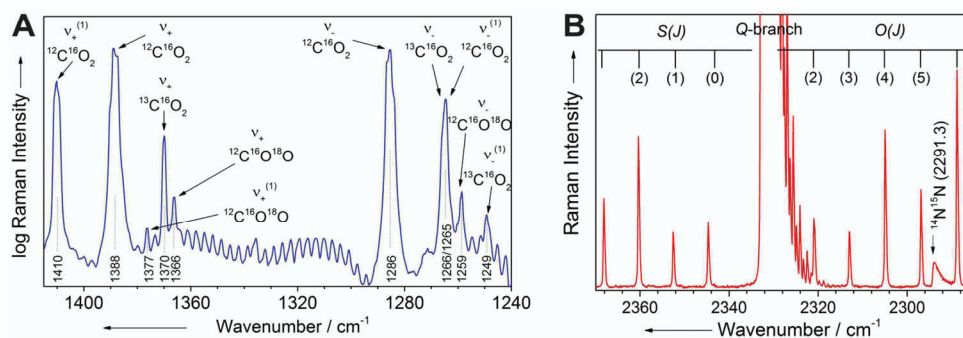
59

Figure 6. (A) Fiber-enhanced high-resolution Raman spectrum of pure CO_2. The spectrally resolved results show in detail the Fermi dyad of the different natural isotopes $^{12}C^{16}O_2$ ($\tilde{\nu}_+$ and $\tilde{\nu}_-$), $^{13}C^{16}O_2$ ($\tilde{\nu}_+$ and $\tilde{\nu}_-$), and $^{12}C^{16}O^{18}O$ ($\tilde{\nu}_+$ and $\tilde{\nu}_-$), respectively, as well as the hot bands of $^{12}C^{16}O_2$ ($\tilde{\nu}_+^{(1)}$ and $\tilde{\nu}_-^{(1)}$), $^{13}C^{16}O_2$ ($\tilde{\nu}_-^{(1)}$), and $^{12}C^{16}O^{18}O$ ($\tilde{\nu}_+^{(1)}$). (B) Fiber-enhanced high-resolution Raman spectrum of pure N_2. The ro-vibrational fine structure of the O- and S-branches next to the strong Q-branch is resolved, and the Raman peak of the $^{14}N^{15}N$ isotope is marked by an arrow.

isotope $^{13}C^{16}O_2$ occurs at lower wavenumbers, at 1370 cm^{-1} ($\tilde{\nu}_+$) and 1266 cm^{-1} ($\tilde{\nu}_-$) with the hot band at 1249 cm^{-1} ($\tilde{\nu}_-^{(1)}$). Even the bands of the isotope $^{12}C^{16}O^{18}O$ are detected at 1366 cm^{-1} ($\tilde{\nu}_+$) and 1259 cm^{-1} ($\tilde{\nu}_-$), respectively, as well as the hot band at 1377 cm^{-1} ($\tilde{\nu}_+^{(1)}$) and the ro-vibrational fine structure of CO_2 (Figure 6A). The natural abundance of ^{18}O and ^{13}C are 0.2% and 1.1% and result in a natural abundance of 1.09% for $^{13}C^{16}O_2$ and 0.39% for $^{12}C^{16}O^{18}O$ within the sum of all carbon dioxide isotopes.[33] For quantitative analysis, the peak area of $^{12}C^{16}O_2$ was integrated from 1385.6 to 1395.1 cm^{-1} and sums up to 150475 counts with a total peak height of 61968 counts and a baseline noise of about 27 counts (standard deviation of the baseline). The integration of the $^{13}C^{16}O_2$ peak from 1368.7−1375.9 cm^{-1} results in 1645 counts and a total peak height of 873 counts. From a comparison of both peaks, an absolute concentration of (1.08 ± 0.03)% was measured for the isotope $^{13}C^{16}O_2$, which is in very good agreement with the theoretical value of 1.09%.

The capability of FERS for highly sensitive quantification of N_2 alongside other biogenic gases and natural isotopes is unique. Natural nitrogen is contained to 78.01% absolute in ambient air (sum of all isotopes). The relative natural concentrations of the individual isotopes are 99.261% for $^{14}N_2$, 0.737% for $^{14}N^{15}N$, and 0.0001% for $^{15}N_2$.[33] The high-resolution FERS measurement of N_2 in ambient air at room temperature is dominated by the Q-branch of $^{14}N_2$ at 2329 cm^{-1} (Figure 6B). The spectrally resolved Q-branch shows the typical asymmetric shape due to different ro-vibrational energy levels with spacing, according to the model of the anharmonic oscillator.[34] The Q-branch is accompanied by O- and S-branches of the rotational transitions, which roughly extend from 2000 to 2600 cm^{-1}. The intensity alternations arise from the statistical weight of the nuclear spin states for even and odd J, with the relation 6:3 (with J = 1 for N_2).[29b] The Q-branch of the isotope $^{14}N^{15}N$ at position 2291 cm^{-1} was used to quantify the isotope abundance of $^{14}N^{15}N$ compared to $^{14}N_2$. The experimentally derived relative abundance of (0.0080 ± 0.0005) is in good agreement with the theoretically expected value of 0.0074.

The results highlight the high potential of fiber-enhanced Raman spectroscopy with hollow-core photonic crystal fibers as minimal volume cuvettes for quantitative analysis of isotopic tracers.

■ SUMMARY AND CONCLUSION

An advanced fiber-enhanced Raman spectroscopic (FERS) setup was presented with specially designed fiber adapter assemblies for stable and quantitative analysis and fully automated gas filling system for alignment-free and fast monitoring of multigas fluctuations down to sub-ppm levels, with a high dynamic range of 6 orders of magnitude, time resolution of seconds, and miniscule sample volumes of nanoliters. A simultaneous FERS quantification of the climate relevant gases CH_4, CO_2, and N_2O together with N_2 and O_2 was demonstrated, and limits of detection as low as 0.2 ppm for methane were achieved. The straightforward quantification of low concentrated homonuclear diatomic gases (e.g., N_2, O_2, and H_2) and chemically almost identical isotopes (e.g., $^{13}CO_2$, $^{12}CO_2$ as well as $^{14}N_2$, and $^{14}N^{15}N$) should be highlighted, since these gases cannot easily be quantified simultaneously with conventional techniques and the tracing of isotopic labels is of outmost importance for the monitoring of metabolic pathways.

The potential of FERS for early stage disease diagnostics was demonstrated with the analysis of 27 nL of exhaled human breath, and it was shown that the major breath components $^{14}N_2$, $^{16}O_2$, and $^{12}CO_2$ as well as the minor components $^{14}N^{15}N$ and $^{13}CO_2$ can be quantified simultaneously over a high dynamic range of 4 orders of magnitude with just one single measurement. While the ^{13}C breath test is already established in breath analysis, we expect that more ^{13}C-tests will be developed in the future based on reliable sensing with the new FERS technique and also foresee a high potential for disease detection via biologically vital nitrogen compounds. The determination of nitrogen ratios with FERS is much faster and simpler compared to complicated measurements with bulky and expensive analytical techniques such as isotope ratio mass spectrometry (IRMS).

Furthermore, there is great potential in the miniaturization of FERS setups with the advantage of high sensitivity and selectivity in combination with portability and affordable prices for such devices. A portable and robust FERS sensor, which is capable for real-time multicomponent quantification of biogenic gases, will be a powerful tool for the characterization of greenhouse gas fluxes and bedside clinical diagnosis of metabolic diseases.

60

■ ASSOCIATED CONTENT

⑤ Supporting Information

Additional information as noted in text. This material is available free of charge via the Internet at http://pubs.acs.org.

■ AUTHOR INFORMATION

Corresponding Author

*E-mail: torsten.frosch@uni-jena.de.

Notes

The authors declare no competing financial interest.

■ ACKNOWLEDGMENTS

■ REFERENCES

(1) (a) Manolis, A. *Clin. Chem.* **1983**, *29* (1), 5−15. (b) Pleil, J. D.; Lindstrom, A. B. *Clin. Chem.* **1997**, *43* (5), 723−730. (c) Buszewski, B.; Kęsy, M.; Ligor, T.; Amann, A. *Biomed. Chromatogr.* **2007**, *21* (6), 553−566.

(2) (a) Hakim, M.; Broza, Y. Y.; Barash, O.; Peled, N.; Phillips, M.; Amann, A.; Haick, H. *Chem. Rev. (Washington, DC, U.S.)* **2012**, *112* (11), 5949−5966. (b) Peng, G.; Tisch, U.; Adams, O.; Hakim, M.; Shehada, N.; Broza, Y. Y.; Billan, S.; Abdah-Bortnyak, R.; Kuten, A.; Haick, H. *Nat. Nanotechnol.* **2009**, *4* (10), 669−673.

(3) (a) Houghton, A. M. *Nat. Rev. Cancer* **2013**, *13* (4), 233−245. (b) Bajtarevic, A.; Ager, C.; Pienz, M.; Klieber, M.; Schwarz, K.; Ligor, M.; Ligor, T.; Filipiak, W.; Denz, H.; Fiegl, M.; Hilbe, W.; Weiss, W.; Lukas, P.; Jamnig, H.; Hackl, M.; Haidenberger, A.; Buszewski, B.; Miekisch, W.; Schubert, J.; Amann, A. *BMC Cancer* **2009**, *9*, 348.

(4) Horvath, I.; Loukides, S.; Wodehouse, T.; Kharitonov, S. A.; Cole, P. J.; Barnes, P. J. *Thorax* **1998**, *53* (10), 867−870.

(5) (a) Olson, J. W.; Maier, R. J. *Science* **2002**, *298* (5599), 1788−1790. (b) Simren, M.; Stotzer, P. O. *Gut* **2006**, *55* (3), 297−303.

(6) (a) Marchetti, M.; Arico, B.; Burroni, D.; Figura, N.; Rappuoli, R.; Ghiara, P. *Science* **1995**, *267* (5204), 1655−1658. (b) Tummala, S.; Sheth, S.; Goldsmith, J.; Goldar-Najafi, A.; Murphy, C.; Osburne, M.; Mullin, S.; Buxton, D.; Wagner, D.; Kelly, C. *Dig. Dis. Sci.* **2007**, *52* (2), 396−401.

(7) (a) Leodolter, A.; Dominguez-Munoz, J. E.; von Arnim, U.; Kahl, S.; Peitz, U.; Malfertheiner, P. *Am. J. Gastroenterol.* **1999**, *94* (8), 2100−2104. (b) Savarino, V.; Mela, G. S.; Zentilin, P.; Bisso, G.; Pivari, M.; Mansi, C.; Mele, M. R.; Bilardi, C.; Vigneri, S.; Celle, G. *Am. J. Gastroenterol.* **1999**, *94* (5), 1203−1208.

(8) (a) Davidson, E. A.; Trumbore, S. E.; Amundson, R. *Nature* **2000**, *408* (6814), 789−790. (b) Schmidt, M. W.; Torn, M. S.; Abiven, S.; Dittmar, T.; Guggenberger, G.; Janssens, I. A.; Kleber, M.; Kogel-Knabner, I.; Lehmann, J.; Manning, D. A.; Nannipieri, P.; Rasse, D. P.; Weiner, S.; Trumbore, S. E. *Nature* **2011**, *478* (7367), 49−56. (c) Conrad, R. *Microbiol. Rev.* **1996**, *60* (4), 609−640.

(9) Luo, G. J.; Brüggemann, N.; Wolf, B.; Gasche, R.; Grote, R.; Butterbach-Bahl, K. *Biogeosciences* **2012**, *9* (5), 1741−1763.

(10) Jerman, V.; Metje, M.; Mandić-Mulec, I.; Frenzel, P. *Biogeosciences* **2009**, *6* (6), 1127−1138.

(11) Forster, P. R. V; Artaxo, P.; Berntsen, T.; Betts, R.; Fahey, D. W.; Haywood, J.; Lean, J.; Lowe, D. C.; Myhre, G.; Nganga, J.; Prinn, R.; Raga, G.; Schultz, M.; Van Dorland, R. Changes in atmospheric constituents and in radiative forcing. In *Climate Change 2007: The Physical Science Basis. Contribution of Working Group I to the Fourth Assessment Report of the Intergovernmental Panel on Climate Change*; Cambridge University Press: Cambridge, 2007.

(12) Ruser, R.; Flessa, H.; Russow, R.; Schmidt, G.; Buegger, F.; Munch, J. C. *Soil Biol. Biochem.* **2006**, *38* (2), 263−274.

(13) (a) Chikaraishi, Y.; Ogawa, N. O.; Doi, H.; Ohkouchi, N. *Ecol. Res.* **2011**, *26* (4), 835−844. (b) Thomas, K. L.; Benstead, J.; Davies, K. L.; Lloyd, D. *Soil Biol. Biochem.* **1996**, *28* (1), 17. (c) Wuebbles, D.; Hayhoe, K. *Earth-Sci. Rev.* **2002**, *57* (3−4), 177. (d) Andreae, M. O.; Schimel, D. S.; Robertson, G. P. *Exchange of Trace Gases between Terrestrial Ecosystems and the Atmosphere: Report of the Dahlem Workshop on Exchange of Trace Gases between Terrestrial Ecosystems and the Atmosphere*; Wiley: Hoboken, NJ, 1989; p 347.

(14) Deng, C.; Zhang, J.; Yu, X.; Zhang, W.; Zhang, X. *J. Chromatogr., B* **2004**, *810* (2), 269−275.

(15) Badjagbo, K. *Clin. Chem. Lab. Med.* **2012**, *50* (11), 1893−1902.

(16) Berden, G.; Peeters, R.; Meijer, G. *Int. Rev. Phys. Chem.* **2000**, *19* (4), 565−607.

(17) Koskinen, V.; Fonsen, J.; Kauppinen, J.; Kauppinen, I. *Vib. Spectrosc.* **2006**, *42* (2), 239−242.

(18) Wolfbeis, O. S.; Weidgans, B. M. Fiber Optic Chemical Sensors and Biosensors: A View Back. In *Optical Chemical Sensors*; Baldini, F., Chester, A. N., Homola, J., Martellucci, S., Eds. Springer: Dodrecht, 2006; pp 17−44.

(19) (a) Frosch, T.; Schmitt, M.; Noll, T.; Bringmann, G.; Schenzel, K.; Popp, J. *Anal. Chem.* **2007**, *79* (3), 986−993. (b) Frosch, T.; Tarcea, N.; Schmitt, M.; Thiele, H.; Langenhorst, F.; Popp, J. *Anal. Chem.* **2007**, *79* (3), 1101−1108. (c) Frosch, T.; Meyer, T.; Schmitt, M.; Popp, J. *Anal. Chem.* **2007**, *79* (16), 6159−6166. (d) Frosch, T.; Popp, J. *J. Mol. Struct.* **2009**, *924−926*, 301−308. (e) Frosch, T.; Popp, J. *J. Biomed. Opt.* **2010**, *15* (4), 041516/1−041516/9. (f) Frosch, T.; Koncarevic, S.; Zedler, L.; Schmitt, M.; Schenzel, K.; Becker, K.; Popp, J. *J. Phys. Chem. B* **2007**, *111* (37), 11047−11056.

(20) (a) Frosch, T.; Koncarevic, S.; Becker, K.; Popp, J. *Analyst (Cambridge, U.K.)* **2009**, *134* (6), 1126−1132. (b) Frosch, T.; Popp, J. *J. Mol. Struct.* **2009**, *924−926*, 301−308. (c) Frosch, T.; Schmitt, M.; Bringmann, G.; Kiefer, W.; Popp, J. *J. Phys. Chem. B* **2007**, *111* (7), 1815−1822. (d) Frosch, T.; Schmitt, M.; Popp, J. *J. Phys. Chem. B* **2007**, *111* (16), 4171−4177. (e) Frosch, T.; Schmitt, M.; Popp, J. *Anal. Bioanal. Chem.* **2007**, *387* (5), 1749−1757. (f) Frosch, T.; Schmitt, M.; Schenzel, K.; Faber, J. H.; Bringmann, G.; Kiefer, W.; Popp, J. *Biopolymers* **2006**, *82* (4), 295−300.

(21) Okita, Y.; Katagiri, T.; Matsuura, Y. *Proc. SPIE* **2010**, *7559*, 755908−755908.

(22) (a) Frosch, T.; Keiner, R.; Michalzik, B.; Fischer, B.; Popp, J. *Anal. Chem.* **2013**, *85* (3), 1295−1299. (b) Keiner, R.; Frosch, T.; Hanf, S.; Rusznyak, A.; Akob, D. M.; Kusel, K.; Popp, J. *Anal. Chem.* **2013**, *85*, 8708−8714. (c) Keiner, R.; Frosch, T.; Massad, T.; Trumbore, S.; Popp, J. *Analyst* **2014**, DOI: 10.1039/C3AN01971C. (d) Salter, R.; Chu, J.; Hippler, M. *Analyst* **2012**, *137* (20), 4669−4676.

(23) (a) Schlosser, M.; Seitz, H.; Rupp, S.; Herwig, P.; Alecu, C. G.; Sturm, M.; Bornschein, B. *Anal. Chem.* **2013**, *85* (5), 2739−2745. (b) Uda, T.; Okuno, K.; Naruse, Y. *J. Radioanal. Nucl. Chem.* **1992**, *159* (1), 145−154. (c) Uda, T.; Okuno, K.; Naruse, Y. *J. Nucl. Sci. Technol.* **1992**, *29* (3), 288−295.

(24) Frosch, T.; Yan, D.; Popp, J. *Anal. Chem.* **2013**, *85* (13), 6264−6271.

(25) (a) Buric, M. P.; Chen, K.; Falk, J.; Velez, R.; Woodruff, S. In *Raman Sensing of Fuel Gases Using a Reflective Coating Capillary Optical Fiber*; Udd, E., Du, H. H., Wang, A., Eds.; SPIE: Orlando, FL, 2009; pp 731608−731608. (b) Eftekhari, F. *J. Appl. Phys.* **2011**, *109* (11), 113104. (c) Pearman, W. F.; Carter, J. C.; Angel, S. M.; Chan, J. W. *Appl. Opt.* **2008**, *47* (25), 4627−4632.

(26) (a) Russell, P. *Science* **2003**, *299* (5605), 358−362. (b) Knight, J. C.; Broeng, J.; Birks, T. A.; Russell, P. S. J. *Science* **1998**, *282* (5393), 1476−1478.

(27) (a) Buric, M. P.; Chen, K. P.; Falk, J.; Woodruff, S. D. *Appl. Opt.* **2008**, *47* (23), 4255−4261. (b) Buric, M. P.; Chen, K. P.; Falk, J.; Woodruff, S. D. *Appl. Opt.* **2009**, *48* (22), 4424−4429.

(28) Schrötter, H. W.; Klöckner, H. W. Raman Scattering Cross Sections in Gases and Liquids. In *Raman Spectroscopy of Gases and Liquids*, Weber, A., Ed. Springer: Berlin, 1979; Vol. *11*, pp 123−166.

(29) (a) Larkin, P. *Infrared and Raman Spectroscopy: Principles and Spectral Interpretation*, 1st ed.; Elsevier: Amsterdam, 2011. (b) Demtröder, W. *Laser Spectroscopy: Experimental Techniques*, 4th ed.; Springer: Berlin, 2008; Vol. *2*.

(30) Long, D. A. *The Raman Effect: A Unified Treatment of the Theory of Raman Scattering by Molecules*; John Wiley & Sons: Hoboken, NJ, 2002; p 624.

(31) Fenner, W. R.; Hyatt, H. a.; Kellam, J. M.; Porto, S. P. S. *J. Opt. Soc. Am.* **1973**, *63* (1), 73−73.

(32) Howard-Lock, H. E.; Stoicheff, B. P. *J. Mol. Spectrosc.* **1971**, *37* (2), 321−326.

(33) Rosman, K. J. R.; Taylor, P. D. P. *Pure Appl. Chem.* **1998**, *70* (1), 18.

(34) Haken, H.; Wolf, H. C. *Molecular Physics and Elements of Quantum Chemistry: Introduction to Experiments and Theory*, 2nd ed.; Springer: Heidelberg, 2004.

62

3.5 Calcite Biomineralization by Bacterial Isolates from the Recently Discovered Pristine Karstic Herrenberg Cave [RK5]

Anna Rusznyák, Denise M. Akob, Sándor Nietzsche, Karin Eusterhues, Kai Uwe Totsche, Thomas R. Neu, Torsten Frosch, Jürgen Popp, Robert Keiner, Jörn Geletneky, Lutz Katzschmann, Ernst-Detlef Schulze, Kirsten Küsel

Calcite Biomineralization by Bacterial Isolates from the Recently Discovered Pristine Karstic Herrenberg Cave

Anna Rusznyák,[a] Denise M. Akob,[a] Sándor Nietzsche,[b] Karin Eusterhues,[c] Kai Uwe Totsche,[c] Thomas R. Neu,[d] Torsten Frosch,[e,f] Jürgen Popp,[e,f] Robert Keiner,[e,f] Jörn Geletneky,[g] Lutz Katzschmann,[g] Ernst-Detlef Schulze,[h] and Kirsten Küsel[a]

Aquatic Geomicrobiology Group, Institute of Ecology, Friedrich Schiller University Jena, Jena, Germany[a]; Centre of Electron Microscopy, University Hospital Jena, Friedrich Schiller University Jena, Jena, Germany[b]; Institute of Geosciences, Friedrich Schiller University Jena, Jena, Germany[c]; Helmholtz Centre for Environmental Research-UFZ, Magdeburg, Germany[d]; Institute of Physical Chemistry, Friedrich Schiller University Jena, Jena, Germany[e]; Institute of Photonic Technologies, Jena, Germany[f]; Thuringian Agency for Environment and Geology, Jena, Germany[g]; and Max Planck Institute for Biogeochemistry, Jena, Germany[h]

Karstic caves represent one of the most important subterranean carbon storages on Earth and provide windows into the subsurface. The recent discovery of the Herrenberg Cave, Germany, gave us the opportunity to investigate the diversity and potential role of bacteria in carbonate mineral formation. Calcite was the only mineral observed by Raman spectroscopy to precipitate as stalactites from seepage water. Bacterial cells were found on the surface and interior of stalactites by confocal laser scanning microscopy. Proteobacteria dominated the microbial communities inhabiting stalactites, representing more than 70% of total 16S rRNA gene clones. Proteobacteria formed 22 to 34% of the detected communities in fluvial sediments, and a large fraction of these bacteria were also metabolically active. A total of 9 isolates, belonging to the genera *Arthrobacter*, *Flavobacterium*, *Pseudomonas*, *Rhodococcus*, *Serratia*, and *Stenotrophomonas*, grew on alkaline carbonate-precipitating medium. Two cultures with the most intense precipitate formation, *Arthrobacter sulfonivorans* and *Rhodococcus globerulus*, grew as aggregates, produced extracellular polymeric substances (EPS), and formed mixtures of calcite, vaterite, and monohydrocalcite. *R. globerulus* formed idiomorphous crystals with rhombohedral morphology, whereas *A. sulfonivorans* formed xenomorphous globular crystals, evidence for taxon-specific crystal morphologies. The results of this study highlighted the importance of combining various techniques in order to understand the geomicrobiology of karstic caves, but further studies are needed to determine whether the mineralogical biosignatures found in nutrient-rich media can also be found in oligotrophic caves.

Recent interest in the role of microbial processes in biogeochemical cycles and the largely unexplored subsurface diversity has spurred research on the geomicrobiology of deep marine and terrestrial environments. Calculations indicate that the total amount of carbon in intraterrestrial organisms may equal that of all terrestrial and marine plants (55). An important part of this biomass is within subsurface microbial ecosystems deep inside the earth (6). Although, in the last 20 years, numerous studies have started to investigate microbial biodiversity in a wide range of habitats, including pristine and contaminated groundwater, marine subsurface habitats, sedimentary and magmatic terrestrial environments, and various caves (31, 37, 52, 70, 72), the physiological and biochemical features of these communities are still awaiting exploration (55).

Caves provide a window into the subsurface and are a prime habitat for investigating subsurface microbial life (1). The majority of previous cave research focused on cave systems where chemical energy fuels microbial communities, such as the ferromanganese deposits of the Lechuguilla Cave in New Mexico (21, 53), the sulfidic Frasassi cave system in Italy or the Movile Cave in Romania (18, 47), the nitrate/nitrite-dominated Nullarbor Cave in Australia (40), or a number of caves receiving allochthonous organic matter input (34). Karstic areas are of specific interest because these carbonate-dominated habitats represent one of the most important natural subterranean carbon reservoirs on Earth (22). Caves provide easy access to karstic environments. However, if caves are open to the public, it can be difficult to differentiate between the pristine indigenous microbial communities and those introduced into the cave by visiting humans or animals. To date, only a limited number of studies have examined the diversity

and activity of microorganisms colonizing karstic habitats (56, 60, 69). Other studies focused on microbial isolates obtained from caves, which are capable of carbonate mineral formation (for example, see references 13, 15, 24, 35, and 63).

Our multidisciplinary study took advantage of the recently discovered Herrenberg Cave, which was discovered in the Thuringian forest in Germany during the excavation of a new rail tunnel. This karstic cave was not affected by human activity before 2008 and appeared to have no contact with migrating higher animals, e.g., bats. Thus, it provided a unique pristine habitat for elucidating the active microbial community in a karstic system. Our goal was to achieve a first glimpse into the geomicrobiology of this pristine cave by combining a broad variety of techniques, including phylogenetic analyses, microscopic techniques, and cultivation-based methods. We had the opportunity to sample stalactite material and fluvial sediments some hours before the cave was permanently closed, and construction work proceeded. With this pristine material, we aimed to (i) elucidate the hidden bacterial diversity and activity, (ii) evaluate the potential of bacterial isolates for carbonate mineralization, and (iii) to study in de-
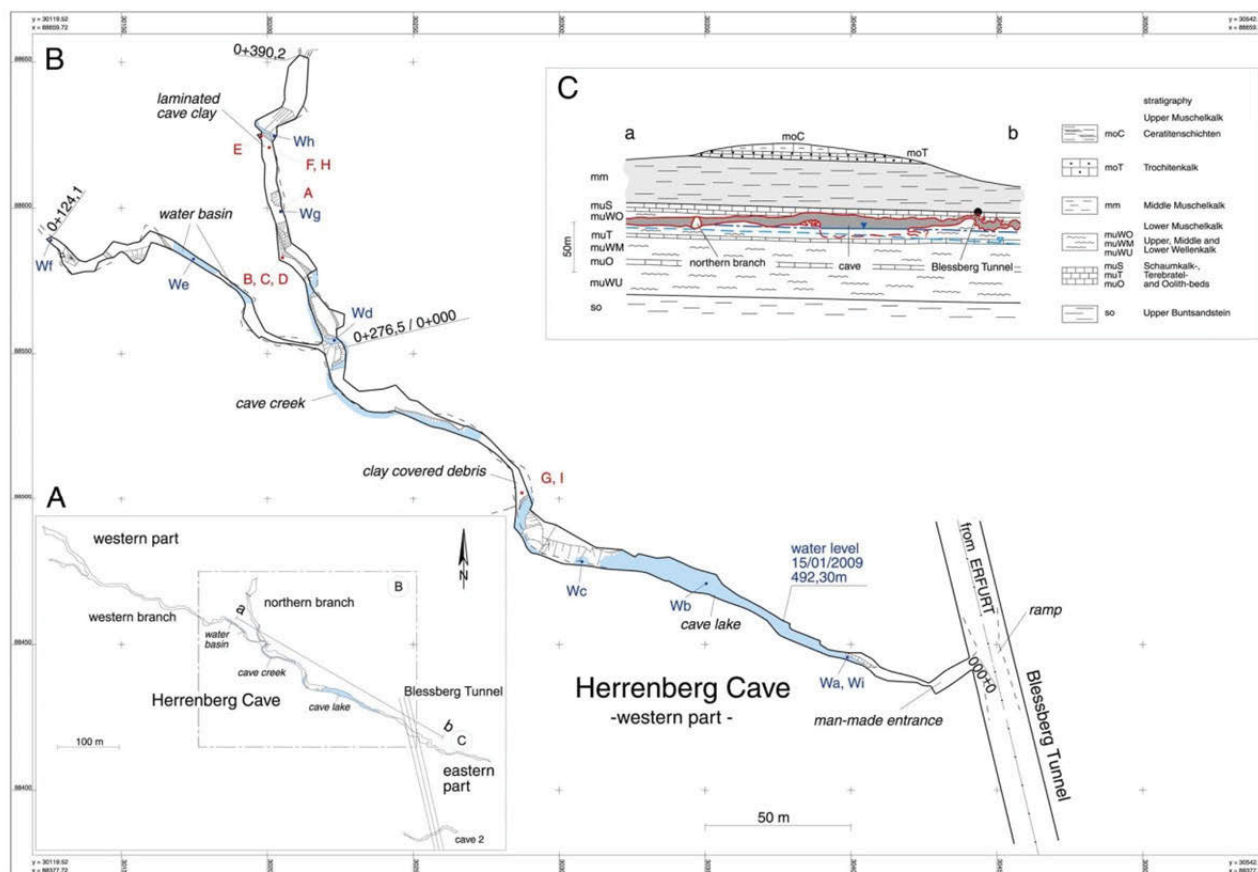
FIG 1 Herrenberg Cave. (A) Map of the Herrenberg Cave located in southwest Thuringia, Germany, with profile line a-b. (B) Sample points in the western part of the cave (samples from sites A to I are solid samples, while Wa to Wi are water samples). A, stalactite; B, brown straw stalactite; C, white straw stalactite; D, eccentric straw stalactite; E, cave wall material; F, entrance sediment material; G, H, and I, fluvial sediments. (C) Geological profile of the area. (Courtesy of the Thuringian State Institute of Environment and Geology, Thuringia, Germany.)

tail different phases of mineral formation with scanning electron microscopy and energy-dispersive X-ray spectroscopy (SEM-EDX) and confocal laser scanning microscopy (CLSM).

MATERIALS AND METHODS

Study site and sampling. Herrenberg Cave (situated between 40 and 90 m below the ground) is located in Thuringia, Germany (R-value 4430286, H-value 5588500, DHDN/Gauss-Kruger zone 4, 11°01′007,5′′E, 50°25′41,6′′N) at the southern foreland of the Thuringian Forest. It was formed during Tertiary and Quarternary times in Middle Triassic limestones and marls of the Lower Muschelkalk formation (mu), i.e., in the main aquifer (Fig. 1). The cave is between 8 to 0.5 m wide and up to 20 m high. Parts of the cave lie under the regional groundwater level characterized by 1.2 to 2.7 mg liter^{-1} dissolved organic carbon (DOC), which flows mainly north to south. Weakly mineralized water (30 to 100 mg liter^{-1} total dissolved salts [TDS] of the Ca-Mg-SO$_4$ type) from quartzite-rich shales enters the limestones of the main aquifer, resulting in intensive solution of calcite and strong mineralization of groundwater [up to 600 mg liter^{-1} TDS of the Ca-(Mg)-HCO$_3$ type]. A small creek flows from north to southwest into a cave lake near the human-made entrance. The average nitrate concentrations were 19.5 mg liter^{-1} in groundwater and 13.7 mg liter^{-1} in seepage water collected from stalactites. The ammonium concentration was 0.01 to 0.02 mg liter^{-1} or below the detection limit. Water and air temperatures in the cave varied between 7 and 9°C.

Samples from different sites of the cave were obtained from the cave in January 2009 using aseptic techniques (Fig. 1) stalactite (site A samples) and straw stalactites (site B samples, brown straw stalactite; site C samples, white straw stalactite; site D samples, excentric straw stalactite), black-colored clay wall material (site E samples), mud at the human-made entrance of the cave (site G samples), and fluvial sediments (site F, H, and I samples). All samples were stored at 4°C until return to the laboratory.

Determination of nitrate, ammonium, total metal concentrations, and C/N analysis. Water samples were filtered through glass microfiber filters (Whatman) and were analyzed for NO$_3^-$ (12) and NH$_4^+$ (10) concentrations. Sediment samples for total Al, Mg, Ca, Fe, Mn, and Na analyses were dried at 100°C, powdered, completely extracted with aqua regia (38), and then analyzed with an inductively coupled plasma mass spectrometer (ICP-MS) (PQ3S; Thermo Electron, United Kingdom). Sediment samples were ground to <100 μm with a ball mill and analyzed for total carbon and nitrogen by dry combustion with a CN analyzer (Vario Max; Elementar Analysensysteme GmbH, Germany). Inorganic carbon was determined by measuring the total amount of carbon after removal of organic carbon (OC) by ignition of samples for 4 h at 550°C (36). OC concentrations were then calculated from the difference between total and inorganic carbon concentrations.

XRD. Powder X-ray diffraction (XRD) patterns were obtained with a Seifert-FPM XRD 7, equipped with a graphite monochromator, using Cu Kα radiation at 40 kV and 30 mA. Step scanning was done from 10° to 52°

65

2Θ with increments of 0.02° 2Θ and a counting time of 10 s per step. Sediment samples 6 and 9 were mounted on glass slides, while precipitates from culture experiments were prepared on Si slides. For clay mineral analysis, the clay fractions of samples 6 and 9 were separated by sedimentation and analyzed as (i) oriented specimens on ceramic tiles, (ii) saturated with glycol, and (iii) after heating to 550°C.

Infrared and Raman spectroscopy. Raman spectra were recorded with a Fourier transform (FT)-Raman spectrometer (Bruker MultiRAM) in microscopic and macroscopic mode with a spectral resolution of 2 cm^{-1}. The instrument was equipped with a Nd:YAG laser (excitation wavelength [λ_{exc}] of 1,064 nm) as the excitation source and a liquid nitrogen-cooled germanium detector. FT-infrared (IR) spectra were measured using a Bruker IFS66 spectrometer equipped with a doped triglycerin sulfate (DTGS) detector and 4-cm^{-1} spectral resolution.

Bacterial community analysis. (i) DNA and RNA extraction, cDNA synthesis, and PCR amplification. Genomic DNA and RNA were isolated and purified from environmental samples using the RNA PowerSoil kit combined with the RNA PowerSoil DNA elution accessory kit (Mo Bio Laboratories, Carlsbad, CA) according to the manufacturer's instructions except for the stalactite sample. In this case, a piece of stalactite (~0.5-cm^2 surface area) was mixed with the bead solution from the kit's bead tube and vortexed to remove surface cells. The liquid was then returned to the kit's bead tube to proceed with the manufacturer's protocol. RNase-free DNase I (Fermentas) was used for DNase treatment of isolated RNA. cDNA was synthesized using the RevertAid first-strand cDNA synthesis kit (Fermentas) according to the manufacturer's instructions. PCR amplification of 16S rRNA gene fragments from isolated genomic DNA or cDNA was performed using the universal eubacterial forward fd1 and reverse rp2 primers (51) in a Peqlab advanced Primus 96 thermocycler. The PCR mixtures contained 1 U *Taq* DNA polymerase in the manufacturer's buffer (Jena Bioscience, Jena, Germany), 1.5 mM MgCl$_2$, 200 μM deoxynucleoside triphosphates (dNTPs), and 0.3 μM (each) primer. Samples were first denatured at 95°C for 5 min, followed by 30 cycles, with 1 cycle consisting of denaturation at 95°C for 30 s, annealing at 55°C for 45 s, and extension at 72°C for 1.5 min, followed by a final extension step at 72°C for 10 min. PCR products were purified using the NucleoSpin extract II kit (Macherey-Nagel, Germany) according to the manufacturer's instructions.

(ii) Construction and analysis of clone libraries. Purified 16S rRNA amplicons were cloned into the pCR4-TOPO vector using the TOPO TA cloning kit for Sequencing with One Shot TOP10 chemically competent *Escherichia coli* cells according to the manufacturer's instructions (Invitrogen, Carlsbad, CA). Ligation reactions originating from the stalactite DNA (site A samples) and sediment RNA (site F samples) were shipped to the Genome Center at Washington University (St. Louis, MO) for transformation and bidirectional sequencing with vector-specific primers (T3/T7). The rest of the clone libraries were constructed and screened in the laboratory. Plasmids were extracted by boiling a loopful of bacterial cells in 50 μl water for 10 min and pelleting the debris by centrifugation (2 min at 15,000 × *g*). The supernatant was transferred into fresh tubes. The inserts were amplified with vector-specific M13f/M13r primers (73). 16S rRNA gene fragments were sequenced by Macrogen (Seoul, South Korea) and AGOWA (Berlin, Germany). Clones were grouped with amplified ribosomal DNA restriction analysis (ARDRA) using the enzymes BsuRI and MspI (Fermentas) as described previously (50).

(iii) Phylogenetic analysis. Sequences were assembled, and vector sequences flanking the 16S rRNA gene inserts were removed using Geneious Pro version 4.6.4 (Biomatters, Auckland, New Zealand). Operational taxonomic units (OTUs) were determined with 0.15 distance cutoff using the Aligner and Complete Linkage Clustering Tool of the Ribosomal Database Project (RDP) (http://pyro.cme.msu.edu). All sequences were checked for possible chimeric artifacts with the Chimera Check Tool from RDP (19). Percent coverage was calculated according to standard equations (5), and rarefaction analysis was performed using Analytic Rarefaction 1.3 (39). The Shannon diversity index was calculated using the Esti-

mateS software program (http://viceroy.eeb.uconn.edu). Sequence similarity was determined using the Basic Local Alignment Search Tool (BLAST) algorithm against the GenBank database available from the National Center for Biotechnology Information (2).

(iv) Quantitative PCR for quantification of bacterial 16S rRNA genes. The copy numbers of bacterial 16S rRNA genes were determined in triplicate for each sediment sample (site F to I samples) and stalactite sample (site A samples) by quantitative PCR (qPCR) using the 331F-797R primers/bactprobe combination (46) and Maxima Probe qPCR Master-Mix (Fermentas) on an Mx3000P instrument (Stratagene). Cycling conditions were 95°C for 10 min and 40 cycles, with 1 cycle consisting of 95°C for 15 s, 60°C for 30 s, and 72°C for 30 s (46). Standard curves were prepared using serial dilutions of mixtures of plasmids containing 16S rRNA clones originating from clones FC36, FC63, FC13, FC29, OMA08, FC75, FC6, FC83, OME09, and FC11, representing the most frequently observed phyla. Standard curves were linear from 4.7×10^8 to 4.7×10^3 16S rRNA gene copies with an efficiency of 104.7%.

Cultivation and identification of isolates. Serial dilutions from sediments were spread on B4 medium containing 2.5 g Ca acetate, 10 g glucose, 4 g yeast extract, 15 g agar liter^{-1} (pH 8.0) (9) and incubated at room temperature or 30°C for 4 weeks in the dark to allow for growth of heterotrophic bacteria. Bacteria were isolated on B4 medium, and isolates were periodically examined by light microscopy to determine the presence of crystals. For microscopic analyses, isolates were transferred to liquid B4 medium and modified B4 (B4MLY) (2.5 g Ca acetate, 0.5 g glucose, and 0.5 g yeast extract liter^{-1} [pH 8.0]) medium and incubated at room temperature and at 30°C for 4 weeks. Genomic DNA from pure cultures was isolated by boiling a loopful of bacterial biomass for 10 min in 100 μl of 5% CHELEX 100 solution (Bio-Rad). After 2 min of centrifugation at 15,000 × *g* (5415C table centrifuge; Eppendorf, Germany), the supernatant was used as a template for PCR amplification. 16S rRNA genes were amplified, sequenced, and analyzed as described above.

CLSM. Upon return to the laboratory, stalactite samples were fixed in 4% formaldehyde in 1× phosphate-buffered saline (PBS) prior to confocal laser scanning microscopy (CLSM). Liquid cultures in B4 medium of the CaCO$_3$-precipitating bacterial isolates, *Arthrobacter sulfonivorans* (SCM3) and *Rhodococcus globerulus* (SCM4), were examined directly without fixation. Samples were stained directly with SYTOX Green (nucleic acid-specific dye), SYPRO Orange (protein staining dye), and Ca-green (free Ca^{2+}-ion-specific dye) (Molecular Probes Inc., Eugene, OR). Staining was carried out on fully hydrated aggregates and directly on the surface of the stalactite sample according to the manufacturer's instructions.

Cell aggregates and the stalactite sample were analyzed by CLSM using a TCS SP5X, controlled by the LAS 2.1.0 software program (Leica, Heidelberg, Germany), equipped with an upright microscope and a super continuum light source. Images were collected with a 63× water immersion lens with a numerical aperture (NA) of 1.2 and a 63× water immersible lens with an NA of 0.9. Scanning was carried out by simple viewing from the top. The samples were examined selecting the excitation lines at 485 nm (reflection and SYPRO), 504 nm (reflection and SYTOX), and 506 nm (reflection and Ca-green). Fluorescence emission signals were recorded from 500 to 650 nm (proteins) for cell aggregates, 516 to 574 nm (nucleic acids), and 516 to 560 nm (free Ca^{2+} ions) for the stalactite sample. In addition, the reflection signals were recorded at the point of excitation. Optical sections of aggregates were recorded in a single scan, and stalactites were recorded at 0.5-μm step size. Images were visualized by using the microscope software (Leica) for maximum-intensity projections and Imaris, version 7.1.0 (Bitplane, Zürich, Switzerland), for XYZ projections. Image data of microbial isolates were subjected to deconvolution using Huygens version 3.6.0 (SVI, The Netherlands) calculated with the CMLE algorithm.

Scanning electron microscopy (SEM) and energy-dispersive X-ray spectroscopy (EDX). A droplet of bacterial suspension from liquid cultures was prepared for SEM by air drying on an electrically conductive,

66

adhesive tag (Leit-Tab; Plano GmbH, Wetzlar, Germany). In order to prevent loss of inorganic material, critical point drying was not performed. The samples were then sputter coated with platinum (thickness of approximately 8 nm) using a SCD005 sputter coater (BAL-TEC, Liechtenstein) to avoid surface charging. Finally, the specimens were investigated with a field emission (FE) SEM LEO-1530 Gemini (Carl Zeiss NTS GmbH, Oberkochen, Germany) at an electron energy of 8 keV using the secondary electron detector. For material contrast, the built-in semiconductor-based back-scattered electron detector was used. For correlation with topography, a secondary electron image was measured simultaneously. The samples used for material contrast SEM were used for EDX, as well. Measurements were carried out using a LEO-1450 instrument (Carl Zeiss NTS GmbH, Oberkochen, Germany) equipped with an EDX system Quantax 200 with an XFlash 5030 detector (Bruker AXS, Berlin, Germany).

Nucleotide sequence accession numbers. The sequences of representative clones were deposited in the GenBank database under accession numbers FR734304 to FR734402. The GenBank accession numbers for strains SCM4 (*Rhodococcus globerulus*) and SCM3 (*Arthrobacter sulfonivorans*) are FR669673 and FR669674, respectively.

RESULTS

Geochemical characteristics and mineralogy of the Herrenberg Cave. In January 2009, we investigated the 800-m-long western branch of the Herrenberg Cave (Fig. 1). Some parts of the walls, roof, and cave floor were covered with magnificent speleothems, e.g., stalagmites and stalactites (site A to D samples), including rare 2-m-long soda straw stalactites. Cave wall material (site E samples) and fluvial sedimentary deposits consisted of mostly mud, clay, and gravel (site F to I samples) and had pH values of 7.2 to 8.0. They contained small amounts of organic carbon (0.5%), nitrogen (0.06%), various amounts of total Al (63.6 to 114.9 mg g^{-1}), Ca (10.8 to 40.5 mg g^{-1}), Mg (15.8 to 28.6 mg g^{-1}), and Fe (31 to 62 mg g^{-1}). Raman microspectroscopic analyses showed a homogeneous distribution of calcite across the surface of the stalactite and straw stalactite samples. All sediment samples contained muscovite, while the content of quartz and carbonates (e.g., dolomite, calcite, and/or aragonite) was considerably higher in site E, G, and I samples, as shown by IR spectroscopy. Two sediments (site F and I samples) were further investigated using XRD, which showed that they contained quartz, dolomite, micaceous minerals, and clays. Clay minerals included illite, kaolinite, and small amounts of vermiculite or chlorite (diffractograms not shown). Additional calcite was found in site F samples.

Distribution, diversity, and activity of cave bacteria. The copy numbers of bacterial 16S rRNA genes determined for fluvial sediments (site F to I samples) and one stalactite (site A samples) yielded bacterial cell counts of approximately 1.5×10^7, 2.5×10^4, 4.6×10^7, and 2.6×10^4 g^{-1} (wet weight) sediment for samples 6, 7, 8, and 9, respectively, and 8.5×10^2 cm^{-2} stalactite surface (site A samples). CLSM of a nucleic acid-stained stalactite sample provided information about the distribution and density of bacterial cells on its surface. On the outer surface, no biofilm formation was observed, with low cell densities observed on the stalactite surface (Fig. 2a). Although a delocalization of cells from the outer surface to the interior surface during sample transport prior to microscopic analysis is unlikely but cannot be completely ruled out, it is interesting to note that bacteria were also detected on the outer surface as well as on the interior surface of the stalactite (Fig. 2b). In addition, numerous bacteria were observed on the surface of a hypha-like structure originating from the stalactite sample (Fig. 2c). Hypha-like structures were also observed in other stalactite

samples, confirming the presence of fungal members of the microbial community inhabiting this cave.

Microbial community characterization was performed on only the stalactite samples (site A samples) and the three sediment samples (site F, H, and I samples), as a limited amount of DNA was obtained from the straw stalactites. A total of 371 16S rRNA gene sequences were analyzed for the 4 samples. The 112 stalactite-derived clones grouped into 37 OTUs, and the library had 37.8% coverage. OTUs related to unclassified bacteria with unclarified phylogenetic affiliations comprised 16% of total clone sequences. The majority of clones (71%) were identified as members of the *Proteobacteria* (*Alphaproteobacteria*, *Betaproteobacteria*, *Gammaproteobacteria*, and *Deltaproteobacteria* subclasses) with a dominance of the *Gammaproteobacteria* subclass (including the genera *Pseudomonas* and *Acinetobacter*). A minor number of clone sequences were related to Gram-positive bacteria (*Firmicutes* and *Actinobacteria*), such as the *Actinobacteria* genus *Arthrobacter*. In addition, members of the phyla *Bacteroidetes*, *Acidobacteria*, *Planctomycetes*, *Verrucomicrobia*, and *Fibrobacteres* were shown to be present in the bacterial communities (Fig. 3; see Table S1 in the supplemental material).

From the three fluvial sediments (site F, H, and I samples), 204 clones were analyzed, and the clones grouped into 35 (site F samples), 22 (site H samples), and 27 (site I samples) OTUs. Only 18 OTUs were detected in more than one of the three sediment samples. Coverage approximated 20.0, 63.6, and 77.8% for site F, H, and I samples, respectively. Bacterial community composition with respect to the majority of taxonomic groups represented in the sediment libraries overlapped at the phylum level (Fig. 3); however, the relative proportions of the different phyla in the three sediment libraries differed. A number of clone sequences (5 to 15%) were related to yet unclassified bacteria with unclarified phylogenetic affiliation. Other sequences grouped within the bacterial phyla *Proteobacteria* (*Alphaproteobacteria*, *Betaproteobacteria*, *Gammaproteobacteria*, and *Deltaproteobacteria* subclasses), *Firmicutes* and *Actinobacteria*, as well as *Bacteroidetes*, *Acidobacteria*, *Nitrospira*, *Chloroflexi*, *Planctomycetes*, *Gemmatimonadetes*, and *Verrucomicrobia* (Fig. 3). The majority of clones (>90%) shared high sequence similarity (95 to 99%) with as yet uncultured organisms, detected in subsurface environments (deep-sea sediments, caves, groundwater), soils, aquatic habitats (fresh- and seawater), as well as plant-associated environments or cold-adapted environments (arctic and tundra soil) (8, 17, 64, 66, 67, 68, 74) (see Table S1 in the supplemental material).

To identify the active fraction of cave bacterial communities, RNA was extracted and used for clone library construction. RNA extracts from stalactites were below the concentrations needed for cDNA amplification. A total of 55 sequences were analyzed for the RNA-derived clone library of sediment sample F (Fig. 3), and these sequences grouped into 30 OTUs with a sampling coverage of 40%. The Shannon index was 3.56. The 16S rRNA gene- and 16S rRNA sequence-based results showed great overlap on the phylum level (Fig. 3), pointing to the activity of most bacterial groups detected within the samples. DNA-based cloning showed that the *Gammaproteobacteria* and *Deltaproteobacteria* were the dominant proteobacterial groups, whereas RNA-based cloning showed that the *Deltaproteobacteria* subgroup was the most abundant within the active bacterial community. Some taxa, e.g., the phyla *Acidobacteria* and *Nitrospira*, exhibited lower abundance in the active community than in the DNA-based clone libraries.
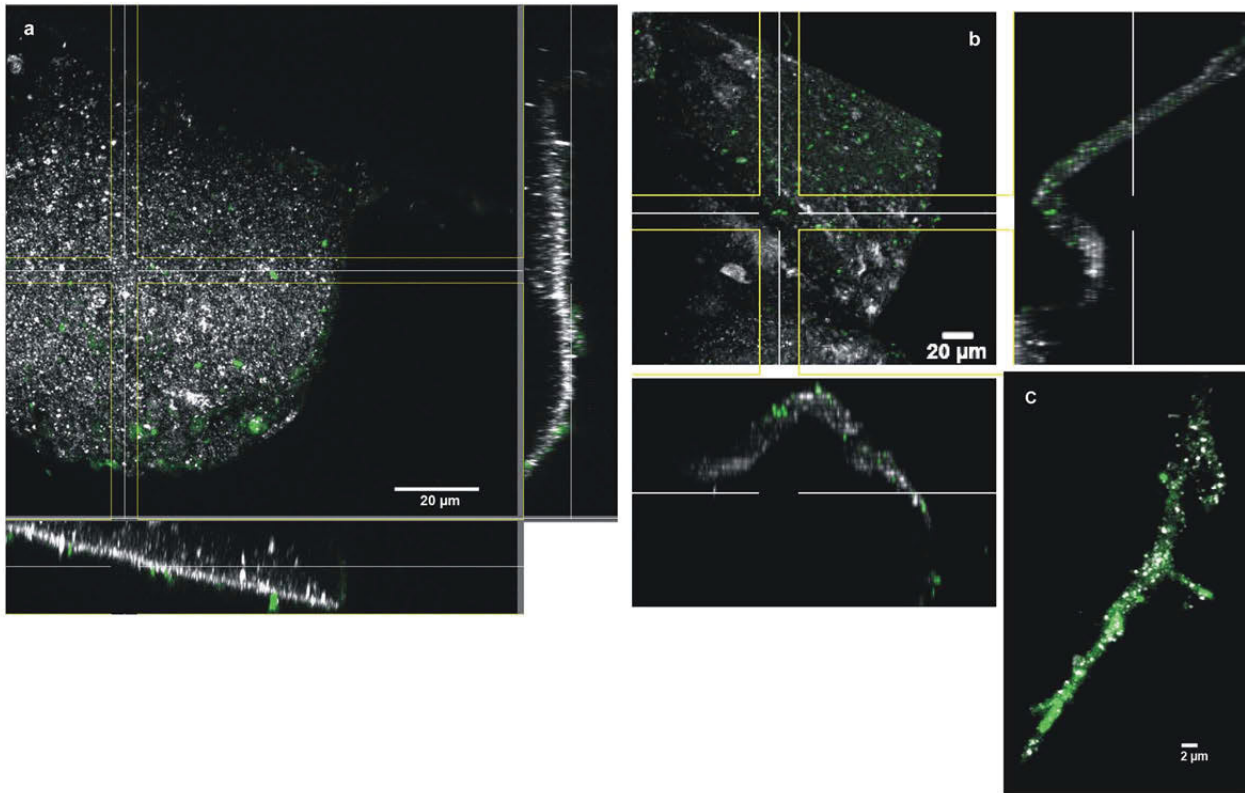
67

FIG 2 Confocal laser scanning microscopy (CLSM) of a stalactite sample taken in the Herrenberg Cave. (a and b) XYZ projection showing the distribution of bacteria on the outer surface (a) and inner surface (b) (cut surface by sampling) of a stalactite surface after staining with SYTOX Green for nucleic acids. (c) CLSM image of a hypha-like structure originating from the Herrenberg Cave, colonized by bacterial cells after staining with SYTOX Green for nucleic acids. Nucleic acids are shown in green, while the reflection signal is shown in white.

More than half of the metabolically active bacteria (53% of total RNA-derived clones) were related to members of the *Alpha-*, *Beta-*, *Gamma-*, and *Deltaproteobacteria*, which was similar to the observed predominance of these groups in the stalactite DNA-based library but contrasted with the proportions of these groups

FIG 3 Frequencies of bacterial phylogenetic lineages detected in 16S rRNA gene and 16S rRNA clone libraries from stalactite and sediment samples taken in the Herrenberg Cave. Calculations were made based on the total number of clones associated with phylotypes of sequenced representatives. Sample A, stalactite; samples F, H, and I, fluvial sediments.

in the sediment DNA-based libraries (Fig. 3). Representatives of some phyla (e.g., *Verrucomicrobia*) were not detected as active members of the fluvial sediments (Fig. 3).

Isolation of carbonate-precipitating bacteria. Plating from serial dilutions of sediment samples was followed by random isolation. A total of 32 bacterial strains were obtained on alkaline B4 carbonate-precipitating medium containing Ca acetate, glucose, and yeast extract. Because liquid cultures are more suitable for microscopic analyses, colonies were transferred to liquid B4 medium and a modified B4 medium (B4MLY), which contained reduced amounts of glucose and yeast extract. Nine isolates were able to grow in liquid medium and could be maintained under laboratory conditions. Isolates were identified as *Pseudomonas putida* (100% sequence similarity), *Serratia plymuthica* (99%), *Flavobacterium hercynium* (98%), *Flavobacterium johnsoniae* (2 isolates) (99%), *Stenotrophomonas rhizophila* (99%), *Rhodococcus fascians* (99%), *Rhodococcus globerulus* (100%), and *Arthrobacter sulfonivorans* (100%). The latter two isolates showed the most intense formation of precipitates in liquid media within 4 weeks of incubation at room temperature. Therefore, these two isolates were chosen for further studies and were cultivated in B4 and B4MLY media at 15°C, at room temperature, and at 30°C. B4MLY medium was used to investigate biomineralization under less-carbon-rich conditions. Biomineralization was also studied in the nutrient-rich B4 medium, because this was used in numerous pre-
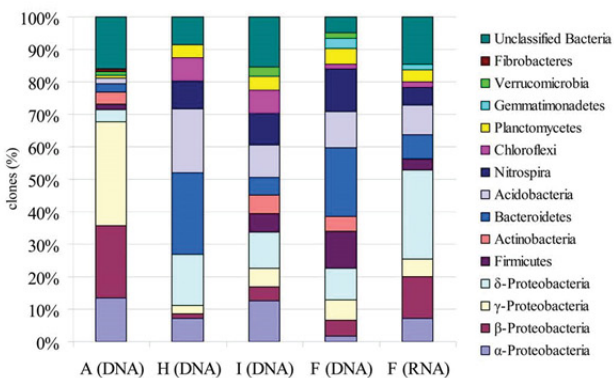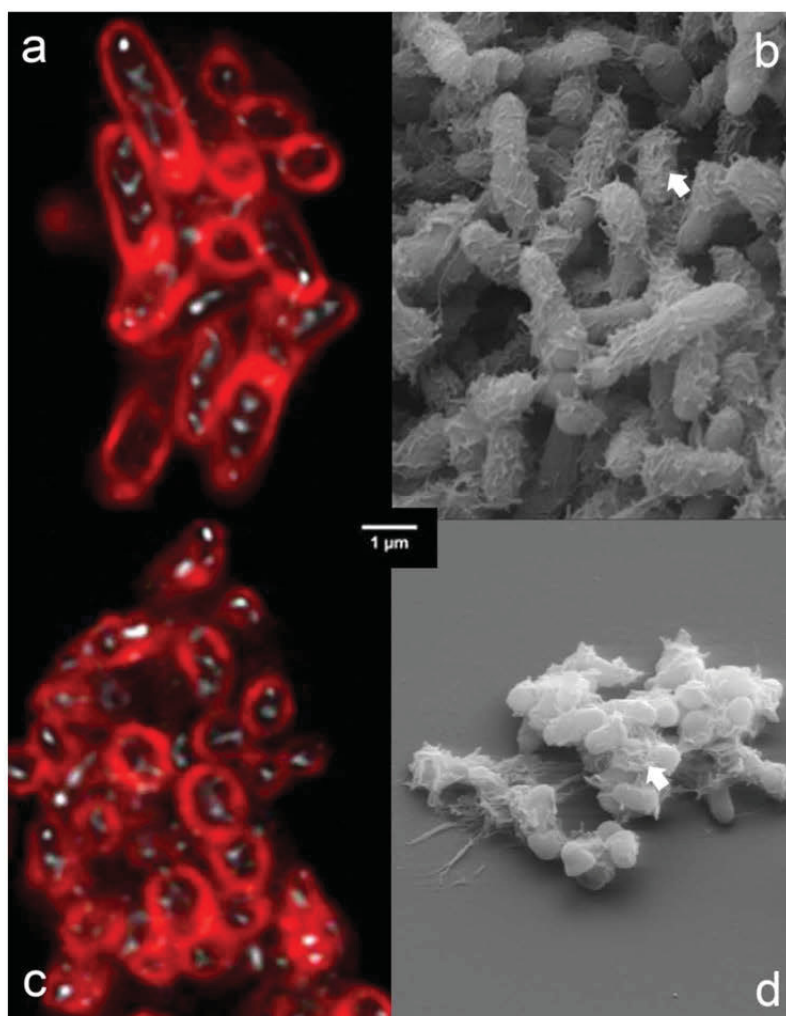
68

FIG 4 (a and c) Confocal laser scanning microscopy of *Arthrobacter sulfonivorans* (a) and *Rhodococcus globerulus* (c) cell aggregates after deconvolution. The cells scanned once after they were stained with SYPRO Orange for proteins. Protein is shown in red, while the reflection signal is shown in white. Note the intracellular reflection signals. (b and d) Scanning electron microscopy of *A. sulfonivorans* (b) and *R. globerulus* (d) cell aggregates and EPS (extracellular polymeric substance) material (white arrows). Due to fixation and dehydration, bacterial cells appear smaller than in laser microscopy images. The scale bar shown in the center of the figure applies to all four panels.

vious studies investigating carbonate-precipitating cave isolates (13, 35, 63).

Phases of biomineral formation by *Arthrobacter sulfonivorans* strain SCM3 and *Rhodococcus globerulus* strain SCM4. Crystalline material was detected by light microscopy in media inoculated with either *A. sulfonivorans* or *R. globerulus* after 20 days of incubation at room temperature or 30°C. Since only slow growth occurred at 15°C within 4 weeks of incubation, we focused on higher temperatures. No mineral formation was observed in any of the uninoculated and autoclaved controls. The pH decreased from pH 8.0 to a pH of 7.29 to 7.84 in the first 24 to 72 h of growth. At the end of the incubation, the pH increased up to 8.21.

Bacteria grew predominantly as aggregates, as seen by SEM of precipitated material (Fig. 4b and d). This observation was confirmed for both isolates using the noninvasive CLSM technique (Fig. 4a and c), which permits analysis of fully hydrated aggregates

without fixation and dehydration. Aggregates observed by CLSM showed cell surface protein staining and a cell internal reflection signal (Fig. 4a and c). Extracellular polymeric substances (EPS) were observed on SEM images of cell aggregates from both isolates (Fig. 4b to d). Ca-green staining showed the accumulation of free Ca^{2+} ions around/within the aggregates (Fig. 5). As the precipitated $CaCO_3$ could not be visualized and investigated by laser scanning microscopy, SEM-EDX, XRD, and Raman spectroscopy were used to identify the precipitated materials. EDX verified that precipitates produced by both isolates were composed of Ca, C, and O, and the atomic percent ratios indicated the presence of $CaCO_3$ (Fig. 6a to d; EDX spectra not shown). XRD and Raman analyses showed that both isolates produced calcite or a mixture of calcite and vaterite. In some samples, a single broad peak (corresponding to a d-spacing of 0.435 to 0.439 nm) pointed to the additional formation of monohydrocalcite. Differences were
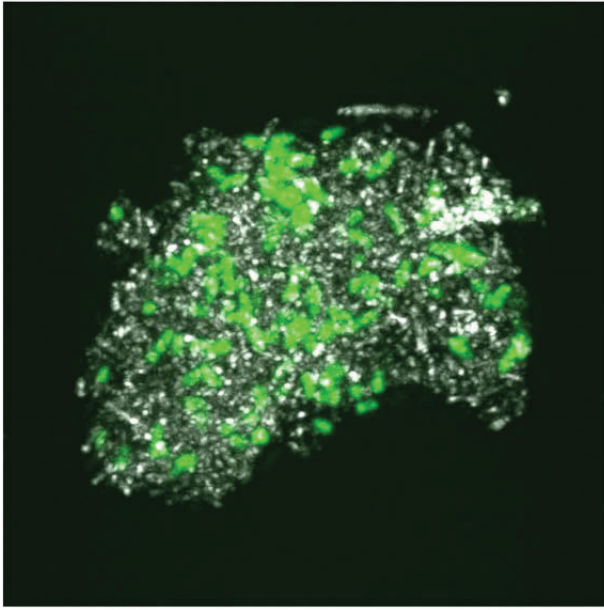
69

FIG 5 Confocal laser scanning microscopy (CLSM) of *Arthrobacter sulfonivorans* cell aggregates after staining with Ca-green for free Ca^{2+} ions. Free calcium ions are shown in green, while the reflection signal is shown in white.

shown in two cases, both at 30°C. In B4MLY medium, the *Arthrobacter* isolate produced not only calcite, as seen for the *Rhodococcus* strain, but also vaterite. In addition, in B4 medium, the *Rhodococcus* strain produced not only calcite and vaterite but monohydrocalcite as well. Interestingly, the morphology of the crystals differed depending on the bacterial species. The crystalline material produced by *A. sulfonivorans* showed xenomorphous, spherical particles, whereas the precipitates of *R. globerulus* contained idiomorphous, often rhombohedral crystals. Spherical crystals were not detected in cultures of *R. globerulus* (Fig. 7a to d).

DISCUSSION

Stalactite and sediment bacterial assemblages of the Herrenberg Cave. Our geological and geochemical data showed that the Herrenberg Cave is a typical karstic habitat (29) including light-limited conditions for microbial life. Mineralogical investigations indicated that calcite precipitates from seepage water as stalactites and accumulates along with insoluble silicates in sediment deposits at the bottom of the cave. In contrast to other diversity studies on karstic caves or karst pools (27, 41, 69), this cave was not accessible to migrating animals (higher animals) or humans in the past. However, a glimpse into this pristine, karstic cave showed that the microbial communities present were not strikingly unique compared to other cave systems, suggesting that the microbial assemblages in karstic environments may be stable and resistant to minor or occasional human activities.

Within the bacterial communities, a high percentage of clone sequences detected were related to unclassified bacteria with no clear phylogenetic affiliation. This is similar to previous studies in karstic aquifers which could identify only one third of the 16S rRNA gene sequences lower than the domain *Bacteria*, indicating autochthonous bacterial communities (27). However, the detection of sequences in our clone libraries that were related to *Bacte-*

ria derived from plant-associated environments, soils, and freshwater/seawater habitats suggested that aboveground and subsurface communities were related, likely due to connections between the two habitats via karstic water. This was seen in another study investigating shallow pools of a different karstic cave system, which found that microbial communities were related to organisms from groundwater or karst water habitats, freshwater, marine, or soil environments (69). The hypha-like structures observed in our samples indicated that fungi are members of the Herrenberg Cave microbial community, similar to what was found in the moonmilk deposits of Ballynamintra Cave in Ireland (62). These organisms can be involved in the transformation of various substrates and in biomineral formation (32, 33).

The stalactite bacterial community was dominated by the physiologically diverse *Proteobacteria* (44). Such dominance was also observed in other caves, e.g., the Lascaux Cave (4), the Tito Bustillo Cave (64), or the Altamira Cave (57, 59). Sequences related to those of *Acidobacteria* were detected in all clone libraries of the Herrenberg Cave, similar to the presence of *Acidobacteria* in the other caves, such as the Altamira Cave (Santillana del Mar, Spain) (65) and Wind Cave, North Dakota (17). The fact that there are only four cultivated species of this phylum limits our understanding of their potential metabolic function in caves. Some evidence exists that *Acidobacteria* are capable of methylotrophic growth (42), which may be an ecological advantage in an oligotrophic habitat with low inputs of organic matter. A number of cultivation-based investigations reported that diverse groups of Gram-positive bacteria inhabit cave environments (13, 26, 35, 45). However, the two Gram-positive phyla (*Firmicutes* and *Actinobacteria*) in our libraries were detected at a relatively low abundance. These contrasting results may arise from the differences in selectivity of the cultivation-based and nucleic acid-based approaches. It is known that a number of biases affect nucleic acid template amplification during PCR (43). PCR-based methods also rely on DNA extractions which can be biased due to differential lysis of cell wall structures that leads to distortions in detecting different bacterial groups in a given environmental sample (30, 49).

The pure cultures obtained from sediments were affiliated with representatives of various genera of the *Gammaproteobacteria* group, as well as the phyla *Bacteroidetes* and *Actinobacteria*. Bacteria from the genera *Pseudomonas, Stenotrophomonas, Serratia, Flavobacterium, Arthrobacter*, and *Rhodococcus* have also been isolated from other caves or karst environments, such as the Kartchner Caverns in Arizona in the United States or from karstic water samples (20, 41). Some of these genera were also detected in the stalactite clone library (see Table S1 in the supplemental material). The presence of *Arthrobacter*-related sequences in the stalactite clone library emphasizes the potential role of these bacteria in calcite mineralization, since members of the genus *Arthrobacter* are known to be capable of carbonate formation (14, 35).

Biomineral formation by *A. sulfonivorans* and *R. globerulus*. The activity of our bacterial strains resulted in carbonate crystal formation. We observed only slow bacterial growth over 4 weeks of incubation at 15°C, suggesting that the rate of metabolic activity was affected. Nevertheless, long-term metabolic transformations may carry significant potential for carbonate precipitation processes and reflect slow transformations that occur *in situ*. The changes in pH observed during incubation are likely due to the consumption of carbon sources: *Arthrobacter* and *Rhodococcus* species are known to utilize acetate, which would result in an increase in the pH of the medium. The latter is an important factor supporting carbonate pre-
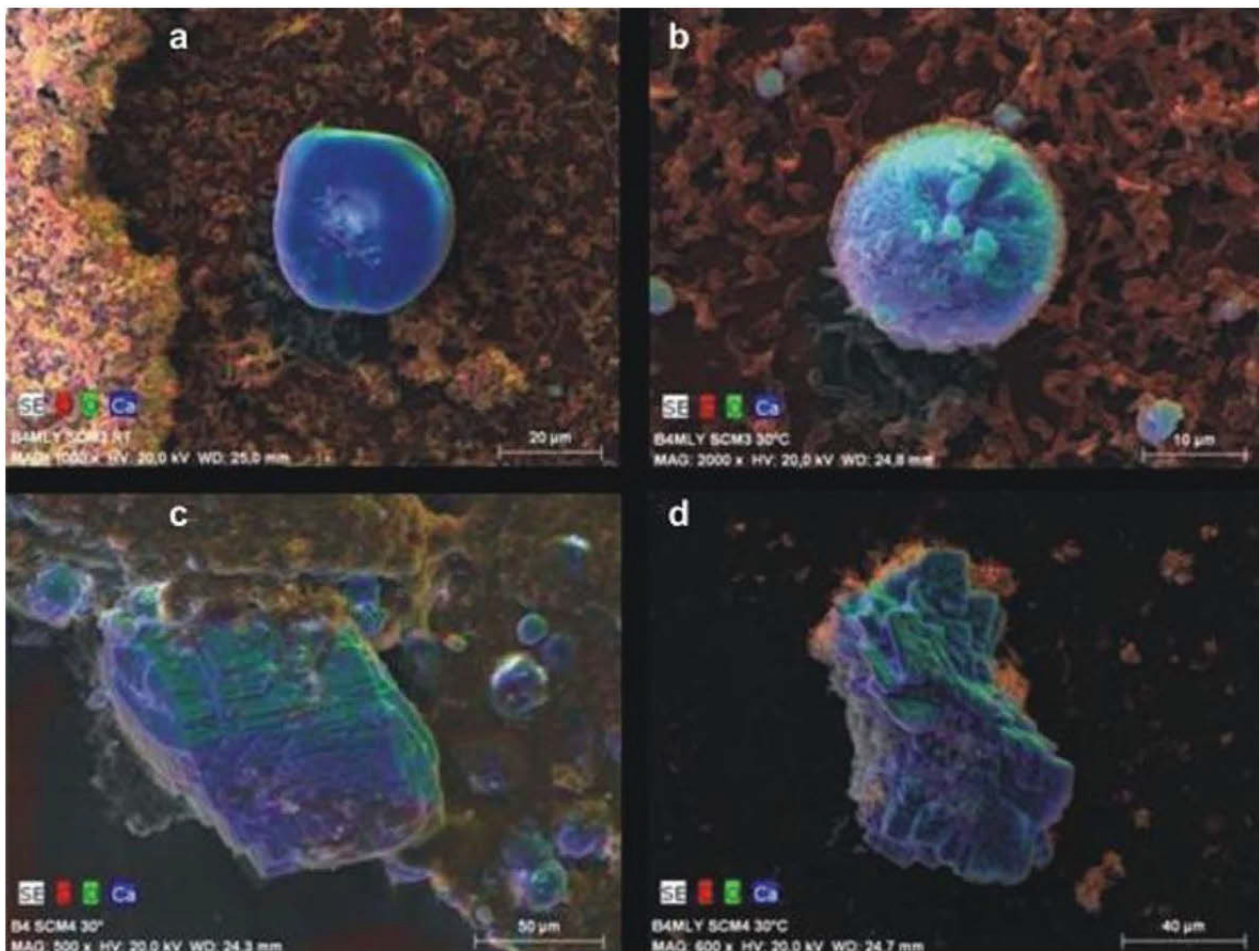
FIG 6 EDX mapping of bacterial calcite minerals of *Arthrobacter sulfonivorans* (SCM3) (a and b) and *Rhodococcus globerulus* (SCM4) (c and d). RT, room temperature; B4, B4 liquid medium (28); B4MLY, modified B4 medium. The SEM images show false colors of red, green, and blue for the local occurrence of the elements carbon, oxygen, and calcium, respectively. A gray level SEM image is underlying each. The shape of the blue-green carbonate minerals depend on the strain; it is round if precipitated in the presence of *Arthrobacter sulfonivorans* but idiomorphous when formed by *Rhodococcus globerulus*. Note the differences in magnification and scale bars.

cipitation (16). Although members of the *Arthrobacter* and *Rhodococcus* genera are known to produce calcite and vaterite (14, 35), the *A. sulfonivorans* and *R. globerulus* species have not been reported previously to precipitate calcite. Furthermore, these bacteria might also be able to form other carbonates, e.g., dolomite.

The formation of vaterite seemed to be favored at higher temperatures, while monohydrocalcite formation was restricted to cultivation in B4 medium. These minerals were not detected in samples by XRD, suggesting that the low *in situ* temperature and small amount of available nutrients in the cave did not favor formation of these minerals. Although the different crystal structures of the newly formed minerals could not be explained completely by the experimental conditions, the cultivation conditions (61), e.g., available nutrients (58), may have influenced which type of $CaCO_3$ mineral was formed. The stable forms of $CaCO_3$, calcite, and aragonite are known to be the most common microbial carbonates (23). *In vitro* bacterial precipitation of the metastable vaterite form has also been reported (14, 63), suggesting that this biogenic mineral structure is more common than previously proposed. Bacteria have been implicated in creating secondary min-

eral formations, such as speleothems, in studies of caves in which a combination of cultivation and electron microscopic analyses using B4 medium were used (3, 13). Future analyses using portable Raman spectroscopy equipment should allow *in situ* mineralogical and microbiological investigations of caves similar to analyses in studies of prehistoric cave paintings (54). In comparison with other analytical techniques, Raman spectroscopy is a nondestructive method and requires extremely small amounts of sample material. The latter was an important aspect of our study due to the limited amount of samples available. Raman spectroscopy has been shown to be a powerful tool for mineralogical investigations of moonmilk deposits in karstic habitats (48).

Imaging of *A. sulfonivorans* and *R. globerulus* cultures using strategic microscopic techniques allowed us to visualize the early phases of carbonate mineralization. CLSM in particular showed us that after aggregation, free Ca^{2+} ions were entrapped and provided a surface for nucleation sites for crystal formation. In the later phases of mineral formation, species-dependent mineral morphologies were visualized with SEM-EDX. The production of EPS, cell aggregation, and Ca^{2+} aggregation are known to be im-
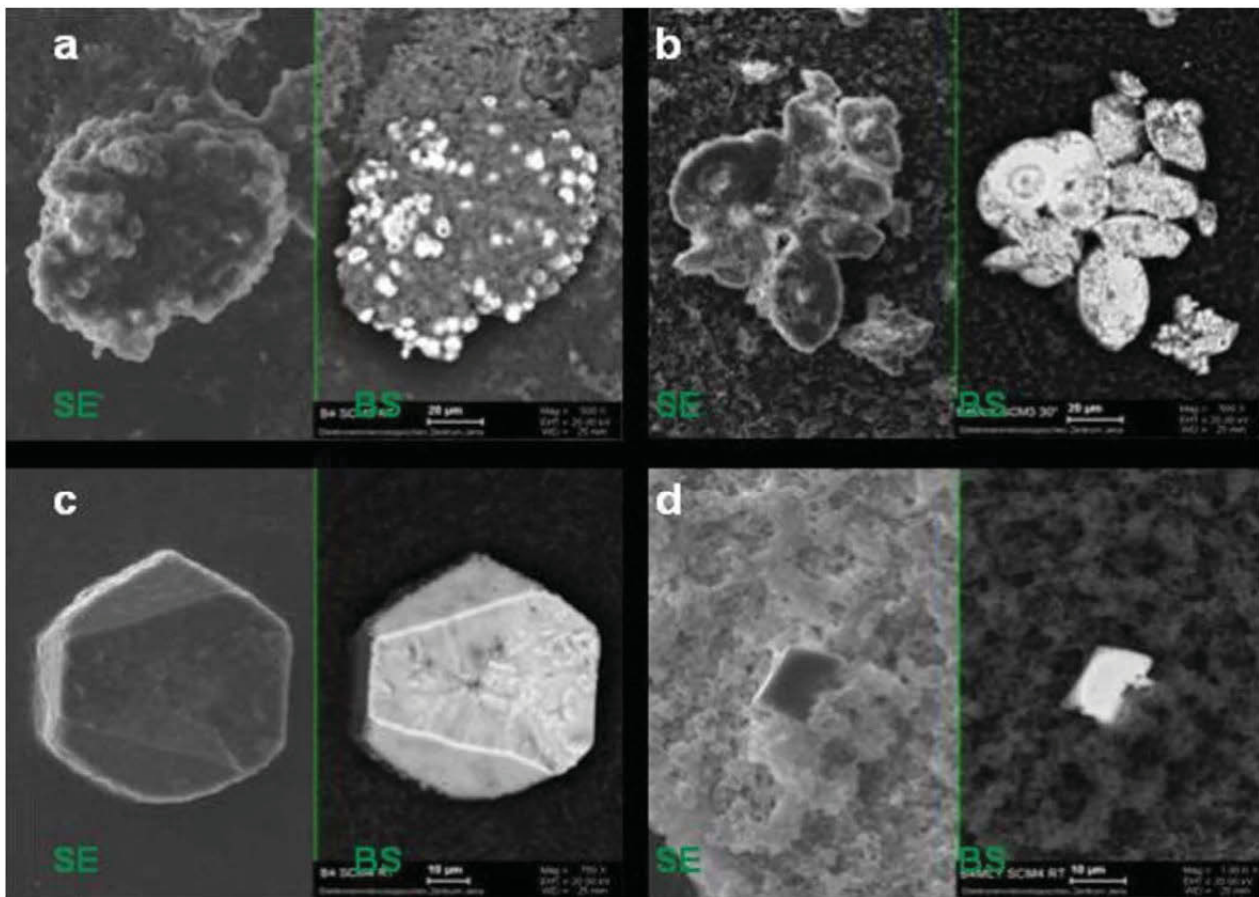
71

FIG 7 Comparison of topography-dependent secondary electron (SE) images to material-dependent back-scattered (BS) electron images of agglomerates produced by *Arthrobacter sulfonivorans* (SCM3) (a and b) and *Rhodococcus globerulus* (SCM4) (c and d). The darker gray color of the BS signal indicates lower atomic numbers, i.e., organic material. The lighter gray color indicates higher atomic numbers, i.e., inorganic material. Note the differences in magnification and scale bars. RT, room temperature; B4, B4 liquid medium; B4MLY, modified B4 medium.

portant factors in the precipitation process (59, 71). The production of specific bacterial outer structures and their chemical nature might also be crucial for the bacterial crystallization process, influencing the mineralogy and morphology of calcium carbonate crystals (11). Calcite formation by two different *Bacillus* species yielded different mineral morphologies independent of the chemical nature of capsular polysaccharides and EPS produced (25). Another work (7) provided evidence of differences in the cell wall properties of *Arthrobacter* and *Rhodococcus* species. The cell walls of *Arthrobacter* spp. lacked mycolic acids in its type B peptidoglycan, whereas *Rhodococcus globerulus* and *R. erythropolis* strains produced mycolic acids (with 34 to 56 C atoms). The presence or absence of mycolic acids influences the cell wall surface properties resulting in a more hydrophilic (*Arthrobacter*) and relatively hydrophobic (*Rhodococcus*) cell surface. In addition, the amount of peptidoglycan and the degree of amidation of free carboxyl groups or other compounds (e.g., phosphate-containing teichoic acids as cell wall accessory polymers of *Arthrobacter* species) may also influence the cell surface charge (7, 28). Such differences may have caused the observed differences in calcium carbonate mineral morphology of the two isolates (Fig. 7).

The recent discovery of the Herrenberg Cave, with its extraor-dinary long straw stalactites, and its lack of human disturbance offered an opportunity to reveal the hidden microbial diversity of a karstic environment. The detection of soil-associated microorganisms in the Herrenberg Cave ecosystem provides evidence for a connection to surface environments. This suggests that we have to be cautious about what is considered a microbial contaminant when characterizing the microbiology of highly accessed cave systems. This detected link between surface and subsurface microbial communities has important implications to critical zone research which aims to understand how such linked communities impact terrestrial biogeochemical cycling (1). Further work should attempt to detect carbonate biosignatures in stalactites by means of noninvasive high spatial mineralogical investigations. Combined with the results of pure culture studies and microscopic analyses, the results will allow a better understanding of the geomicrobiology of the Earth's hidden belowground carbon storage.

ACKNOWLEDGMENTS

72

This study is part of the research project AquaDiv@Jena funded by the ProExcellence Initiative of the federal state of Thuringia, Germany.

REFERENCES

1. Akob DM, Küsel K. 2011. Where microorganisms meet rocks in the Earth's Critical Zone. Biogeosciences 8:2523–2562.
2. Altschul SF, et al. 1997. Gapped BLAST and PSI-BLAST: a new generation of protein database search programs. Nucleic Acids Res. 25:3389–3402.
3. Banks ED, et al. 2010. Bacterial calcium carbonate precipitation in cave environments: a function of calcium homeostasis. Geomicrobiol. J. 27:444–454.
4. Bastian F, Alabouvette C, Saiz-Jimenez C. 2009. Bacteria and free-living amoeba in the Lascaux Cave. Res. Microbiol. 160:38–40.
5. Begon M, Harper JL, Townsend CR. 1990. Ecology: individuals, populations and communities. Blackwell Scientific Publications, Oxford, England.
6. Ben-Ari ET. 2002. Microbiology and geology: solid marriage made on Earth. ASM News 68:13–18.
7. Bendinger B, Rijnaarts HHMK, Altendorf Zehnder AJB. 1993. Physicochemical cell surface and adhesive properties of coryneform bacteria related to the presence and chain length of mycolic acids. Appl. Environ. Microbiol. 59:3973–3977.
8. Bottos EM, Vincent WFCW, Greer Whyte LG. 2008. Prokaryotic diversity of arctic ice shelf microbial mats. Environ. Microbiol. 10:950–966.
9. Bouquet E, Boronat A, Ramos-Cormenzana A. 1973. Production of calcite (calcium carbonate) crystals by soil bacteria is a general phenomenon. Nature 246:527–529.
10. Bower CE, Holm-Hansen T. 1980. A salicylate-hypochlorite method for determining ammonia in seawater. Can. J. Fish. Aquat. Sci. 37:794–798.
11. Braissant O, Cailleau GC, Dupraz Verrecchia AP. 2003. Bacterially induced mineralization of calcium carbonate in terrestrial environments: the role of exopolysaccharides and amino acids. J. Sediment. Res. 73:485–490.
12. Braman RS, Hendrix SA. 1989. Nanogram nitrite and nitrate determination in environmental and biological materials by vananadium(III) reduction with chemiluminescence detection. Anal. Chem. 61:2715–2718.
13. Cacchio P, Contento RC, Ercole G, Cappucio MP, Martinez Lepidi A. 2004. Involvement of microorganisms in the formation of carbonate speleothems in the Cervo Cave (Làquila-Italy). Geomicrobiol. J. 21:497–509.
14. Cacchio P, Ercole CG, Cappuccio Lepidi A. 2003. Calcium carbonate precipitation by bacterial strains isolated from limestone cave and from a loamy soil. Geomicrobiol. J. 20:85–98.
15. Canaveras JC, Sanchez-Moral SV, Soler Saiz-Jimenez C. 2001. Microorganisms and microbially induced fabrics in cave walls. Geomicrobiol. J. 18:223–240.
16. Castanier S, Le Metayer-Levrel G, Perthuisot JP. 1999. Ca-carbonates precipitation and limestone genesis — the microbiogeologist point of view. Sediment. Geol. 126:9–23.
17. Chelius MK, Moore JC. 2004. Molecular phylogenetic analysis of Archaea and Bacteria in Wind Cave, South Dakota. Geomicrobiol. J. 21:123–134.
18. Chen Y, et al. 2009. Life without light: microbial diversity and evidence of sulfur- and ammonium-based chemolithotrophy in Movile Cave. ISME J. 3:1093–1104.
19. Cole JR, et al. 2003. The Ribosomal Database Project (RDP-II): previewing a new autoaligner that allows regular updates and the new prokaryotic taxonomy. Nucleic Acids Res. 31:442–443.
20. Cousin S, Brambilla E, Yang J, Stackebrandt E. 2008. Culturable aerobic bacteria from the upstream region of a karst water rivulet. Int. Microbiol. 11:91–100.
21. Cunningham KI, Northup DE, Pollastro RM, Wright WG, LaRock EJ. 1995. Bacteria, fungi and biokarst in Lechuguilla Cave, Carlsbad Caverns National Park, New Mexico. Environ. Geol. 25:2–8.
22. Ehrlich HL. 1998. Geomicrobiology: its significance for geology. Earth-Sci. Rev. 45:45–60.
23. Ehrlich HL. 2002. Geomicrobiology, 4th ed. Marcel Dekker, New York, NY.
24. Engel AS, Stern LA, Bennett PC. 2004. Microbial contributions to cave formation: new insights into sulfuric acid speleogenesis. Geology 32:369–372.
25. Ercole C, Cacchio P, Botta AL, Centi V, Lepidi A. 2007. Bacterially induced mineralization of calcium carbonate: the role of exopolysaccharides and capsular polysaccharides. Microsc. Microanal. 13:42–50.
26. Ercole C, Cacchio PG, Cappucio Lepidi A. 2001. Deposition of calcium carbonate in karst caves: role of bacteria in Stiffe's Cave. Int. J. Speleol. 30:69–79.
27. Farnleitner AH, et al. 2005. Bacterial dynamics in spring water of alpine karst aquifers indicates the presence of stable autochthonous microbial endokarst communities. Environ. Microbiol. 7:1248–1259.
28. Fiedler F, Schäffer MJ. 1987. Teichoic acids in cell walls of strains of the "nicotianae" group of *Arthrobacter*: a chemotaxonomic marker. Syst. Appl. Microbiol. 9:16–21.
29. Ford DC, Williams PW. 2007. Karst hydrogeology and geomorphology. John Wiley and Sons, Chichester, England.
30. Frostegård Å, et al. 1999. Quantification of bias related to the extraction of DNA directly from soils. Appl. Environ. Microbiol. 65:5409–5420.
31. Fry JC, et al. 2007. Prokaryotic populations and activities in an interbedded coal deposit, including a previously deeply buried section (1.6–2.3 km) above ~150 Ma basement rock. Geomicrobiol. J. 26:163–178.
32. Gadd GM. 2004. Mycotransformation of organic and inorganic substrates. Mycologist 18:60–70.
33. Gadd GM. 2007. Geomycology: biogeochemical transformations of rocks, minerals, metals and radionuclides by fungi, bioweathering and bioremediation. Mycol. Res. 111:3–49.
34. Groth I, Saiz-Jimenez C. 1999. Actinomycetes in hypogean environments. Geomicrobiol. J. 16:1–8.
35. Groth I, Schumann P, Laiz L, Sanchez-Moral S, Canaveras JC, Saiz-Jimenez C. 2001. Geomicrobiological study of the Grotta di Cervi, Porto Badisco, Italy. Geomicrobiol. J. 18:241–258.
36. Grüneberg E, Schöning I, Kalkoa EKV, Weisser WW. 2010. Regional organic carbon stock variability: a comparison between depth increments and soil horizons. Geoderma 155:426–433.
37. Hazen TC, Jimenez L, Devictoria GL. 1991. Comparison of bacteria from deep subsurface sediment and adjacent groundwater. Microbiol. Ecol. 22:293–304.
38. Hoffman G. 1991. Methodenbuch. Die Untersuchung von Böden, vol. 1. VDLUFA-Verlag, Darmstadt, Germany.
39. Holland SM. 2003. Analytical rarefaction 1.3. User's guide and application. UGA Stratigraphy Lab, University of Georgia, Athens, GA. http://www.uga.edu/strata/software/anRareReadme.html.
40. Holmes AJ, et al. 2001. Phylogenetic structure of unusual aquatic microbial formations in Nullarbor caves, Australia. Environ. Microbiol. 3:256–264.
41. Ikner LA, Toomey RSG, Nolan JW, Neilson BM, Pryor Maier RM. 2007. Culturable microbial diversity and the impact of tourism in Kartcher Caverns, Arizona. Microbiol. Ecol. 53:30–42.
42. Kalyuzhnaya MG, Lidstrom ME, Chistoserdova L. 2008. Real-time detection of actively metabolizing microbes by redox sensing as applied to methylotroph populations in Lake Washington. ISME J. 2:696–706.
43. Kanagawa T. 2003. Bias and artifacts in multitemplate Polymerase Chain Reactions (PCR). J. Biosci. Bioeng. 96:317–323.
44. Kersters K, De Vos P, Gillis M, Swings J, Vandamme P, Stackebrandt E. 2006. Introduction to the Proteobacteria, p 3–37. *In* Dworkin M, Falkow S, Rosenberg E, Schleifer KH, Stackebrandt E. (ed), The prokaryotes. Springer Verlag, New York, NY.
45. Laiz L, Groth I, Gonzalez I, Saiz-Jimenez C. 1999. Microbiological study of the dripping waters in Altamira Cave (Santillana del Mar, Spain). J. Microbiol. Methods 36:129–138.
46. Lane DJ. 1991. 16S/23S rRNA sequencing, p 115–175. *In* Stackebrandt E, Goodfellow M (ed), Nucleic acid techniques in bacterial systematics, John Wiley and Sons Ltd, London, England.
47. Macalady JL, Jones DS, Lyon EH. 2007. Extremely acidic, pendulous cave wall biofilms from the Frasassi cave system, Italy. Environ. Microbiol. 9:1402–1414.
48. Martínez-Arkarazo I, Angulo M, Zuloaga O, Usobiaga A, Madariaga JM. 2007. Spectroscopic characterisation of moonmilk deposits in Pozalagua tourist cave (Karrantza, Basque Country, North of Spain). Spectrochim. Acta A 68:1058–1064.
49. Martin-Laurent F, et al. 2001. DNA extraction from soils: old bias for new microbial diversity analysis methods. Appl. Environ. Microbiol. 67:2354–2359.
50. Massol-Deya AA, Odelson DA, Hickey RF, Tiedje JM. 1995. Bacterial community fingerprinting of amplified 16S and 16-23S ribosomal DNA sequences and restriction endonuclease analysis (ARDRA), p 3.3.2:1–

73

3.3.2:8. *In* Akkermans ADL, van Elsas JD, deBruijn FJ (ed), Molecular microbial ecology manual. Kluwer Academic Publishers, Dordrecht, The Netherlands.

51. Nadkarni MA, Martin FE, Jacques NA, Hunter N. 2002. Determination of bacterial load by real-time PCR using a broad range (universal) probe and primer set. Microbiology 148:257–266.

52. Nealson KH, Inagaki F, Takai K. 2005. Hydrogen-driven subsurface lithoautotrophic microbial ecosystems (SLiMEs): do they exist and why should we care? Trends Microbiol. 13:405–410.

53. Northup DE, et al. 2003. Diverse microbial communities inhabiting ferromanganese deposits in Lechuguilla and Spider Caves. Environ. Microbiol. 5:1071–1086.

54. Ospitali F, Smith DC, Lorblanchet M. 2006. Preliminary investigations by Raman microscopy of prehistoric pigments in the wall-painted cave at Roucadour, Quercy, France. J. Raman Spectrosc. 37:1063–1071.

55. Pedersen K. 2000. Exploration of deep intraterrestrial microbial life: current perspectives. FEMS Microbiol. Lett. 185:9–16.

56. Personné JC, Poty F, Mahler BJ, Drogue C. 2004. Colonization by aerobic bacteria in karst: laboratory and in situ experiments. Ground Water 63:3367–3373.

57. Portillo MC, Gonzalez JM, Saiz-Jimenez C. 2008. Metabolically active microbial communities of yellow and gray colonizations on the walls of Altamira Cave, Spain. J. Appl. Microbiol. 104:681–691.

58. Portillo MC, Porca E, Cuezva S, Canaveras JC, Sanchez-Moral S, Gonzalez JM. 2009. Is the availability of different nutrients a critical factor for the impact of bacteria on subterranean carbon budgets? Naturwissenschaften 96:1035–1042.

59. Portillo MC, Saiz-Jimenez C, Gonzalez JM. 2009. Molecular characterization of total and metabolically active bacterial communities of "white colonizations" in the Altamira Cave, Spain. Res. Microbiol. 160:41–47.

60. Pronk M, Goldscheider N, Zopfi J. 2009. Microbial communities in karst groundwater and their potential use for biomonitoring. Hydrogeol. J. 17:37–48.

61. Rivadeneyra MA, Delgado G, Ramos-Cormenzana A, Delgado R. 1998. Biomineralization of carbonates by *Halomonas eurihalina* in solid and liquid media with different salinities: crystal formation sequence. Res. Microbiol. 149:277–287.

62. Rooney DC, Hutchens E, Clipson N, Baldini J, McDermott F. 2010. Microbial community diversity of moonmilk deposits at Ballynamintra Cave, Co. Waterford, Ireland. Microb. Ecol. 60:753–761.

63. Sanchez-Moral S, Canaveras JC, Laiz L, Saiz-Jimenez C, Bedoya J, Luque L. 2003. Biomediated precipitation of calcium carbonate metastable phases in hypogean environments: a short review. Geomicrobiol. J. 20:491–500.

64. Schabereiter-Gurtner C, Saiz-Jimenez C, Pinar G, Lubitz W, Rölleke S. 2002. Phylogenetic 16S rRNA analysis reveals the presence of complex and partly unknown bacterial communities in Tito Bustillo cave, Spain, and on its palaeolithic paintings. Environ. Microbiol. 4:392–400.

65. Schabereiter-Gurtner C, Saiz-Jimenez C, Pinar G, Lubitz W, Rölleke S. 2002. Altamira cave paleolithic paintings harbour partly unknown bacterial communities. FEMS Microbiol. Lett. 211:7–11.

66. Schauer R, Bienhold C, Ramette A, Harder J. 2010. Bacterial diversity and biogeography in deep-sea surface sediments of the South Atlantic Ocean. ISME J. 4:159–170.

67. Schloss PD, Handelsman J. 2006. Toward a census of bacteria in soil. PLoS Comput. Biol. 2:92.

68. Schmalenberger A, Tebbe CC. 2002. Bacterial community composition in the rhizosphere of a transgenic, herbicide-resistant maize (*Zea mays*) and comparison to its non-transgenic cultivar Bosphore. FEMS Microbiol. Ecol. 40:29–37.

69. Shabarova T, Pernthaler J. 2010. Karst pools in subsurface environments: collectors of microbial diversity or temporary residence between habitat types. Environ. Microbiol. 12:1061–1074.

70. Stevens TO, McKinley JP. 1995. Lithoautotrophic microbial ecosystems in deep basalt aquifers. Science 270:450–454.

71. Van Lith Y, Warthmann R, Vasconcelos C, Mckenzie JA. 2003. Sulphate-reducing bacteria induce low-temperature Ca-dolomite and high Mg-calcite formation. Geobiology 1:71–79.

72. van Waasbergen LG, Balkwill DL, Crocker FH, Bjornstad BN, Miller RV. 2000. Genetic diversity among *Arthrobacter* species collected across a heterogeneous series of terrestrial deep-subsurface sediments as determined on the basis of 16S rRNA and *recA* gene sequences. Appl. Environ. Microbiol. 66:3454–3463.

73. Zhou J, Davey ME, Figueras JB, Rivkina E, Gilichinsky D, Tiedje JM. 1997. Phylogenetic diversity of a bacterial community determined from Siberian tundra soil. Microbiology 143:3913–3919.

74. Zinger L, Shahnavaz B, Baptist F, Geremia RA, Choler P. 2009. Microbial diversity in alpine tundra soils correlates with snow cover dynamics. ISME J. 3:850–859.

74

Author Contribution

[RK1] Raman Spectroscopy - An Innovative and Versatile Tool To Follow the Respirational Activity and Carbonate Biomineralization of Important Cave Bacteria

Anal. Chem. **2013**, 85, 18, 8708-8714

Robert Keiner: conception, measurements, calculations, data analysis, preparation of the manuscript

Torsten Frosch: project leadership, measurements, conception, discussion of results, preparation and correction of the manuscript

Stefan Hanf: mapping experiments

Anna Rusznyák: preparation of bacterial samples, preparation and correction of the manuscript

Denise M. Akob: preparation of bacterial samples

Kirsten Küsel: discussion and correction of the manuscript

Jürgen Popp: project leadership, discussion and correction of the manuscript

[RK2] Enhanced Raman multigas sensing – a novel tool for control and analysis of $^{13}CO_2$-labeling experiments in environmental research

Analyst **2013,** 139, 16, 3813-4019

Robert Keiner: conception, measurements, calculations, data analysis, preparation of the manuscript

Torsten Frosch: project leadership, conception, discussion of results, preparation and correction of the manuscript

Tara Massad: preparation of plant samples, conception and realization of the labeling experiment, discussion and correction of the manuscript

Sue Trumbore: discussion and correction of the manuscript

Jürgen Popp: project leadership, discussion and correction of the manuscript

[RK3] Investigation of Gas Exchange Processes in Peat Bog Ecosystems by Means of Innovative Raman Gas Spectroscopy

Anal. Chem. **2013**, 85, 3, 1295-1299

Robert Keiner: conception, measurements, calculations, data analysis, preparation of the manuscript

Torsten Frosch: project leadership, conception, discussion of results, preparation and correction of the manuscript

Beate Michalzik: collection and preparation of peat bog samples, discussion and correction of the manuscript

Bernhard Fischer: preparation of the Raman gas sensor, correction of the manuscript

Jürgen Popp: project leadership, discussion and correction of the manuscript

[RK4] Fiber-enhanced Raman multi-gas spectroscopy – a versatile tool for environmental gas sensing and breath analysis
Anal. Chem. **2014**, 5278-5285

Stefan Hanf: conception, measurements, calculations, data analysis, preparation of the manuscript

Robert Keiner: measurements, data analysis, discussion of results, correction of the manuscript

Di Yan: design of the adapter

Torsten Frosch: project leadership, conception, discussion of results, preparation and correction of the manuscript

Jürgen Popp: project leadership, discussion and correction of the manuscript

[RK5] Calcite Biomineralization by Bacterial Isolates from the Recently Discovered Pristine Karstic Herrenberg Cave

Anna Rusznyák, Denise M. Akob, Sándor Nietzsche, Karin Eusterhues, Kai Uwe Totsche, Thomas R. Neu, Jörn Geletneky, Lutz Katzschmann, Ernst-Detlef Schulze, Kirsten Küsel: conception, measurements, data analysis, preparation and correction of the manuscript

Robert Keiner: Raman and IR measurements, data analysis, correction of the manuscript

Torsten Frosch: Raman and IR measurements, data analysis, correction of the manuscript

Jürgen Popp: discussion and correction of the manuscript

Acknowledgment

This part is dedicated to all, who made this interdisciplinary work possible.

First of all, I would like to thank Prof. Jürgen Popp for the opportunity to work in his group, his trust, supervision and the constructive negotiations with him.

Also I thank the referees (N.N.) for reading and evaluating this thesis.

Many thanks belong to Dr. Torsten Frosch, for his intensive supervision. He contributed with immense creativity and persistence to almost every aspect of this work. We complemented very well in terms of experimental realization on the one hand and writing/publishing on the other hand.

I thank Dr. Bernhard Fischer (former affiliate of Philips Medical Systems, Boeblingen) and Nico Correns (Carl-Zeiss Microscopy, Jena) and their co-workers for the huge amount of energy and time that was spent on developing the Raman gas device far in advance to the time we started and for lending us some devices for our work. Their help with the peat bog ecosystem publication is highly acknowledged as well.

Many thanks are dedicated to Dr. Anna Rusznyák, Dr. Martina Herrmann and Prof. Kirsten Küsel for their sustained help with the liquid cultures and their contributions to the publication about microbial respiration.

Dr. Tara Massad and Prof. Susan Trumbore gave me the opportunity to participate in their $^{13}CO_2$ pulse labeling experiment. Thanks for that and for the substantial contribution to the isotope labeling publication.

I would like to thank Dr. Marie-Cécile Gruselle and Prof. Beate Michalzik for the nice cooperation with the peat bog ecosystem.

Without the technical personal Wolfgang Fähndrich (Institute of Physical Chemistry), Thomas Büttner, Michael Wiedemann, Bernd Neundorf, Fabian Hildebrandt and Manuel Glatter (Institute of Photonic Technologies) building all the necessary mechanical devices would have been impossible. On the "electronic side" are Rainer Bark, Dirk Hieronymus and Peter Engelhardt (Electronic Workshop at Institute of Optics and Quantum Mechanics). Many thanks belong to all of you.

Declaration of Originality

Ich erkläre, dass mir die Promotionsordnung der chemisch-geowissenschaftlichen Fakultät bekannt ist. Weiterhin habe ich die vorliegende Arbeit selbständig angefertigt und alle Beiträge von anderen Personen und Quellen gekennzeichnet. Ich habe die Hilfe eines Promotionsberaters nicht in Anspruch genommen und diese Dissertation wurde noch nicht anderweitig als wissenschaftliche Prüfung eingereicht. Bei der Auswertung des Materials und der Herstellung der Manuskripte haben mich weitere Personen unterstützt (siehe Kapitel „Author contribution").